Thesis for the Degree of Doctor of Philosophy

Strain engineering of electrical and photovoltaic properties of 1D and 2D semiconductors

Jonatan Holmér

Department of Physics

Chalmers University of Technology

Gothenburg, Sweden 2024

Strain engineering of electrical and photovoltaic properties of 1D and 2D semiconductors

Jonatan Holmér

ISBN 978-91-8103-126-3
Doktorsavhandlingar vid Chalmers tekniska högskola, Ny serie nr 5584
ISSN 0346-718X

Department of Physics
Chalmers University of Technology
SE-412 96 Gothenburg
Sweden
Telephone +46 (0)31 772 3334

Cover image:
Upper left: HR TEM image of a GaAs nanowire.
Upper: Single-nanowire I-V characteristics at different strain levels.
Upper right: 2D MoS_2-flake suspended over a gap with tunable width.
Center: False color SEM image of an STM-probe contacting a single nanowire.
Lower left: Schematic illustration of in situ STM-SEM characterization of nanowires.
Lower: SEM image of in situ exfoliation of 2D MoS_2 flake.
Lower right: SEM images of a straining series of a GaAs nanowire.

Printed at Chalmers Digitaltryck
Gothenburg, Sweden 2024

Strain engineering of electrical and photovoltaic properties of 1D and 2D semiconductors

Jonatan Holmér
Department of Physics
Chalmers University of Technology

Abstract

Semiconductor nanowires and 2D-materials have unique physical properties that are suitable for various electronic and optoelectronic applications. The small physical dimensions, high surface-to-volume ratio and pristine crystallinity of the materials make them able to withstand high levels of elastic strain. Their elasticity makes these materials ideal candidates for elastic strain engineering (ESE), where strain is intentionally applied to enhance the desired physical properties of a material. Realization and investigation of ESE on nanomaterials require techniques that enable high resolution imaging and application and detection of strain on the nanoscale. In situ electron microscopy fulfills these requirements.

In this thesis work, in situ electron microscopy and Raman spectroscopy techniques were developed and applied to study ESE of charge transport and photovoltaic properties of individual GaAs nanowires and 2D MoS_2. An in situ scanning tunneling microscope (STM) – focused ion beam and scanning electron microscope (FIBSEM) setup was developed to investigate ESE of individual GaAs nanowires. Furthermore, procedures to fabricate optimized electrical contacts on individual nanowires in the FIBSEM were established. Uniaxial tensile strain of more than 3% could be applied to the nanowires, which resulted in large modification of their current-voltage (I-V) characteristics, and an increased photocurrent by more than a factor of 4 during near-infrared illumination.

The STM-FIBSEM setup was also used to transfer and study ESE of freestanding 2D MoS_2 flakes. It was found that the applied strain modifies the I-V characteristics of 2D MoS_2. Moreover, a piezo-straining device was developed to correlate electron microscopy, Raman spectroscopy and I-V characterization on the 2D-flakes. Evolution of strain distribution in 2D MoS_2 due to applied stress was investigated by in situ Raman mapping.

Keywords: Semiconductor nanowires, GaAs nanowires, Nanowire solar cells, Elastic strain engineering, In situ electron microscopy, 2D semiconductors, Transition metal dichalcogenides, MoS_2

List of appended papers

This thesis is based on the following papers:

Paper I
An STM – SEM setup for characterizing photon and electron induced effects in single photovoltaic nanowires
Jonatan Holmér, Lunjie Zeng, Thomas Kanne, Peter Krogstrup, Jesper Nygård, Ludvig de Knoop, and Eva Olsson
Nano Energy 53, 2018, 175-181

Paper II
Tuning Hole Mobility of Individual p-Doped GaAs Nanowires by Uniaxial Tensile Stress
Lunjie Zeng, Jonatan Holmér, Rohan Dhall, Christoph Gammer, Andrew M. Minor, and Eva Olsson
Nano Letters 9, 2021, 3894-3900

Paper III
Enhancing the NIR photocurrent in single GaAs nanowires with radial p-i-n junctions by uniaxial strain
Jonatan Holmér, Lunjie Zeng, Thomas Kanne, Peter Krogstrup, Jesper Nygård and Eva Olsson
Nano Letters 21, 2021, 9038-9043

Paper IV
Revealing mechanisms of ion beam milling to optimize electrical contacts on individual GaAs nanowires using analytical and in situ electron microscopy
Jonatan Holmér, Lunjie Zeng and Eva Olsson
In manuscript

My contributions to the appended papers

Paper I: I developed the experimental technique together with my co-authors. I performed all the in situ STM-SEM experiments and analyzed the data. I wrote the first draft of the manuscript and finalized it together with my co-authors

Paper II: I performed some of the sample preparation using FIBSEM. I was involved in the in situ TEM experimental work. I performed the in situ STM-FIBSEM

measurements for the supplementary information. I performed the data analysis of the I-V characteristics.

Paper III: I planned the study and performed all the in situ STM-FIBSEM experiments. I developed the theoretical model used for quantitative analysis of the measured I-V characteristics. I wrote the first draft of the manuscript and finalized it together with my co-authors.

Paper IV: I planned the study and performed all the sample preparation, electrical measurements and TEM characterization. I was involved in the STEM EDS experimental work and analyzed the data. I performed the theoretical simulations. I wrote the first draft of the manuscript.

Acknowledgements

The research presented in this thesis was carried out in Eva Olsson Group, Division of Nano- and Biophysics within the Department of Physics, Chalmers University of Technology, Gothenburg, Sweden during the period 2018 – 2024. The work was performed under the supervision of Prof. Eva Olsson and co-supervisor Dr. Lunjie Zeng.

The thesis work was funded by the Swedish Research Council and the Knut and Alice Wallenberg Foundation, and this support is gratefully acknowledged.

My PhD-studies have been a long journey with a lot of ups and downs, and there are several people that have helped me along the way that I would like thank: First of all, I would like to thank my supervisor **Prof. Eva Olsson** for giving me the opportunity to carry out my PhD-studies within her group, for giving me valuable feedback and inspiration, and for supporting me and believing in me throughout my work. I would like to thank my co-supervisor **Dr. Lunjie Zeng** for helping me and teaching me so much and for always being open for discussions that has often lead to new insights and ideas. I would like to thank the past and present members of Eva Olsson Group, for giving me feedback during group presentations, and for being great colleagues and creating a nice working atmosphere. A special thanks to my former office mate **Dr. Gustav Persson** for all help and nice discussions. I would like to thank the CMAL staff, especially **Dr. Ludvig de Knoop** for showing me how to use the Nanofactory equipment, **Dr. Stefan Gustavsson** for helping me out with the electron microscopes, and **Dr. Katarina Logg** for teaching me how to use the Raman microscope. I would also like to thank **Dr. Anamul Md Hoque** for showing me some tricks and tips about 2D exfoliation and transfer. To **Ola Löfgren** for helping me with computer-related problems. To all the members of the Materials Microstructure division, for nice lunch discussions. Lastly I would like to thank my friends and family, for being a great support. A special thanks to my mother, **Carina**, and to **Katarina**, for all the help with babysitting. To my partner **Linda**, thank you for always being there for me, for supporting me when I feel down and overwhelmed by work, and for being a great mom! And of course to my two sons, **Vincent** and **Elias**, for reminding me of what is most important in life.

List of Abbreviations

1D	one-dimensional
2D	two-dimensional
AFM	Atomic force microscope
ALD	Atomic layer deposition
BF	Bright field
BSE	Backscattered electron
CCD	Charge-coupled device
CVD	Chemical vapour deposition
DF	Dark field
EBIC	Electron beam induced current
EBID	Electron beam induced deposition
ESE	Elastic strain engineering
ET	Everhart-Thornley
FIBSEM	Focused ion-beam scanning electron microscope
GIS	Gas injection system
HRTEM	High resolution transmission electron microscopy
LED	Light emitting diode
MBE	Molecular beam epitaxy
MEMS	Microelectromechanical system
NIR	Near-infrared
NWA	Nanowire array
PCE	Power conversion efficiency
PDMS	Polydimethylsiloxane
SA	Selective-area
SC	Self-catalyzed
SE	Secondary electron
SEM	Scanning electron microscopy
STM	Scanning tunneling microscope
TCO	Transparent conductive oxide
TE	Thermionic emission
TEM	Transmission electron microscopy
TFE	Thermionic field emission
TMDC	Transition metal dichalcogenide
TP	Twin plane
WZ	Wurtzite
ZB	Zinc Blende

Contents

1. Introduction

Semiconductors play a vital role in many of the technologies that our society depends upon, because of their unique physical properties. Their ability to support an internal electrical field and the possibility to control their electrical conductivity via doping and gating make semiconductors essential for modern electronics, especially as the fundamental component in field effect transistors [1, 2]. Furthermore, semiconductors' ability to absorb, propagate and emit light makes them useful for photovoltaic and optoelectronic applications such as solar cells, photodetectors and light emitting diodes (LEDs) [3, 4]. So far, semiconductor technology has been dominated by silicon-based devices. However, in many applications, the fundamental limitations of Si hinder further progress, and this motivates research of alternative semiconductor materials and structures.

Much of the progress in semiconductor technology has been driven by the downscaling of components. This has triggered a rapid development in semiconductor nanofabrication and nanotechnology. Nanofabrication not only allows device miniaturization, but also brings new possibilities for functionality in semiconductors. By entering the nano regime, the physical properties may differ substantially from bulk semiconductors. For example, nanomaterials may exhibit quantum confinement effects, giving rise to novel electrical and optical properties [5, 6]. Furthermore, nanoscale crystalline materials can usually withstand higher levels of elastic strain than their bulk counterparts [7, 8]. Two types of nanomaterials that are promising for a wide range of applications are semiconductor nanowires and 2-dimensional (2D) semiconductors.

Semiconductor nanowires have high aspect ratios and diameters on the nanometer scale. This geometry offers advantages in many applications. For example, nanowire-based field effect transistors could provide further downscaling of electronic devices [9]. Nanowires may also be used to miniaturize optical and optoelectronic devices by acting as optical waveguides [10], nanoscale lasers [11] and LEDs [12]. One particularly interesting application of semiconductor nanowires is solar cells. The sub-wavelength diameter of the nanowires enables them to act as antennas for incoming sunlight, enhancing the light absorbtion [13]. Furthermore, their high surface-to-volume ratio enables growth of defect-free compound nanowires on lattice-mismatched substrates such as Si, which is not possible with bulk structures [14]. These and other unique properties make semiconductor nanowires potential building blocks for highly efficient, low-cost solar cells [15].

2D-semiconductors such as transition metal dichalcogenides (TMDCs) have unique physical properties due to their van der Waals layered structure with thicknesses

down to a single atomic layer [16]. Their high carrier mobilities at atomic scale thicknesses and dangling bond-free surfaces make them promising building blocks for next-generation nanoelectronics [17]. Furthermore, their high light-absorption efficiency, band gap tunability, and high degree of freedom for making artificial heterostructures make 2D semiconductors highly interesting for photonic and photovoltaic applications [18].

Common to both semiconductor nanowires and 2D semiconductors is that their small physical dimensions, high surface-to-volume ratio and high level of crystallinity make them able to withstand high levels of elastic strain [19–21]. This property makes these materials ideal candidates for elastic strain engineering (ESE), where elastic strain is intentionally applied to a material to alter its physical properties [22]. ESE is a powerful tool to gain access to material properties that could be complicated or even impossible to reach through conventional methods such as doping or chemical composition engineering. The elastic strain could be induced through material epitaxial growth or mechanical manipulation. Mechanically induced ESE is of particular interest because it could provide a reversible access to a continuous spectrum of properties within the same specimen, and ideally it would be possible to go back and forth on this spectrum at will. To realize and investigate ESE on nanomaterials, it is essential to be able to experimentally apply and measure strain on the nanoscale, while simultaneously measure the effect of strain on the properties of interest.

1.1 Scope of the thesis

The aim of this thesis is to develop techniques for elastic strain engineering of semiconductor nanowires and 2D semiconductors and to study the effect of strain on the photovoltaic and electrical properties of GaAs nanowires and 2D MoS_2.

An in situ scanning tunneling microscope (STM) – focused ion beam and scanning electron microscope (FIBSEM) technique for the characterization of individual semiconductor nanowires standing vertically on a growth substrate was developed. This technique enables high levels of elastic strain to be applied to the nanowires in a controlled manner. Simultaneously, current-voltage (I-V) measurements under both illuminated and dark conditions, as well as electron beam induced current mapping can be performed. The in situ technique was used to investigate the effect of strain on electrical conductivity, band gap energy, photocurrent generation and other properties of GaAs nanowires with built-in radial p-i-n junctions or homogeneous p-doping. Furthermore, procedures for making stable, high-quality metal-semiconductor contacts to individual nanowires in situ were developed, and the mechanisms behind the contact-optimization were investigated.

The in situ STM-FIBSEM technique was also adapted to enable elastic strain engineering of 2D semiconductors. Moreover, a technique for straining of individual 2D-flakes, based on piezo-actuators and compatible with both electron and Raman

microscopy, was developed.

2. III-V semiconductor nanowires

III-V semiconductors are composed of one element from group III in the periodic table and one from group V. Some examples are GaAs, GaN and InAs. Most III-V semiconductors have direct bandgaps [23], leading to efficient light absorption. They also have high carrier mobilities. III-V nanowires exhibit these properties and additional advantages related to the nanowire geometry, making them promising for nanoelectronics and solar cells.

2.1 Fabrication methods

A prerequisite for all the nanowire-based research and technology is the ability to fabricate high-quality nanowires. In 1964, the growth of Si nanowiskers through a vapor-liquid-solid process was first reported [24]. The first III-V compound nanowires were made in 1997 [25]. Since then, a rapid development has taken place in this field. Today, III-V compound nanowires of high quality and uniformity regarding diameter and length, crystallinity and doping profile can be routinely fabricated.

One way to categorize the different nanowire fabrication methods is to divide them into top-down and bottom-up processes. In a top-down process, the wanted nanostructure is formed by removing material from a bulk sample. This is typically done by forming a protective mask on top of a substrate using lithography, followed by an etching process where the nanowires are formed with the mask as template. It has been demonstrated that III-V nanowires with a wide range of diameter and length can be fabricated using this technique [26]. Even tapered nanowires can be produced this way [27]. However, the most common way to fabricate III-V nanowires today is through bottom-up growth, typically on a substrate. With the bottom-up approach, one can better utilize the unique advantages of nanowires. One advantage is reduced material consumption, as opposed to the top-down approach which inevitably entails a waste of material. Other advantages are the possibilities to form novel, defect-free heterostructures and radial doping profiles, while maintaining control of the nanowire length and diameter. Three main methods are used to grow III-V nanowires, metal-seeded, self-catalyzed (SC) and selective-area (SA) growth [28]. In metal-seeded growth, a metal (usually Au) seed particle is liquefied and forms a eutectic alloy with the group III element, which acts as a catalytic for the nanowire growth. The III and V compounds are injected in the gas phase and nucleate at the liquid-solid interface between the catalytic droplet and the substrate. In this way, the nanowire is grown epitaxially in one direction, one atomic layer at

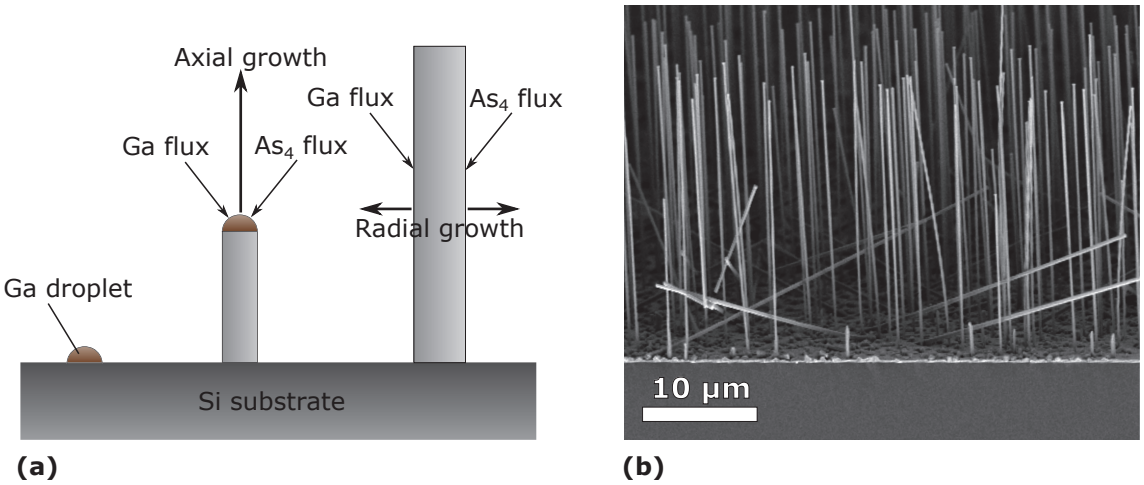

Figure 2.1: Schematic illustration **(a)** and SEM image **(b)** of GaAs nanowires grown by self-catalyzed molecular beam epitaxy.

a time [29]. One concern with this method is that part of the metal seed particle may be incorporated into the nanowire and degrade the electronic properties [30] [31]. This risk is eliminated in SC growth, where the growth process is similar but the catalyst is a pure group III-element droplet [32]. In SA growth, the substrate is covered with a mask with defined holes where the nanowire growth take place. The growth mechanism relies on the formation low-index facets of the nanowires controlled by the growth conditions, and no catalyst is needed [33].

The nanowires used in this work were fabricated through SC molecular beam epitaxy (MBE), see Figure 2.1. In MBE, a substrate is placed in a growth chamber with a pressure of a few 10^{-11} Torr. This ultra-high vacuum is needed to avoid unintentional impurities and surface contamination of the grown structure. The substrate is heated to a temperature of several hundreds of °C. Atomic or molecular beams of the growth species are injected into the chamber and adsorbed on the substrate. No interaction between the species of different beams occurs until they reach the substrate, and this enables fabrication of structures with very abrupt changes in composition or doping [34]. For growth of GaAs nanowires on a Si substrate, a flux of Ga and As_4 or As_2 is added into the chamber. Ga atoms accumulate at naturally occurring pin-holes in the native SiO_2 layer that cover the substrate and form liquid droplets, which eventually become supersaturated and epitaxial growth is initiated at the liquid-solid interface between the droplets and the substrate [35]. Since it is the structure of the native oxide that determines where growth will be initiated, the positions of the nanowires will be random and some will grow at an angle <90 degrees to the substrate due to the formation of polycrystalline seeds [36]. However, it is possible to grow a thicker SiO_2 layer (∼20 nm) and create holes in it with lithography, when control of the growth positions of the nanowires is needed. By optimizing the ratio between the diameter and thickness of the holes in the oxide, a high yield of ordered arrays of vertical nanowires can be achieved [37, 38]. When the desired length of the nanowires has been achieved, the Ga droplet can be consumed and the growth conditions such as temperature and beam fluxes may be changed to promote radial

growth, in order to increase the diameter or form radial doping structures. Doping can be incorporated both during axial and radial growth by adding a flux of the dopant element [39].

2.2 Structure and properties

III-V nanowires generally have high crystal quality, with a low density of impurities, point defects and dislocations. However, issues regarding surface defects, stacking faults due to polytypism and twin boundaries are common. The surface of the nanowire constitutes a disruption in the periodic crystal lattice which may affect the electronic properties. Especially, electronic states introduced by dangling bonds at the surface may act as recombination centers for charge carriers, an effect that can severely impair the performance of nanowire photovoltaic devices. Surface passivation may be used to mitigate these effects [40]. III-V nanowires that have been exposed to air are typically oxidized and covered with a thin native oxide layer [41]. This may obstruct the formation of low-resistive electrical contacts to the nanowires by forming an insulating barrier [42].

Regarding the crystal structure of III-V semiconductors, either the cubic zinc-blende (ZB) or the hexagonal wurtzite (WZ) structure is thermodynamically stable in bulk form, depending on the ionicity of the compound [43]. The ZB structure can be described as having a stacking sequence of ABCABC... and WZ ABABAB... along the [111] direction, where each A, B or C represents a bilayer consisting of both a layer of III-type atoms and a layer of V-type atoms, see Figure 2.2. In the nanowire

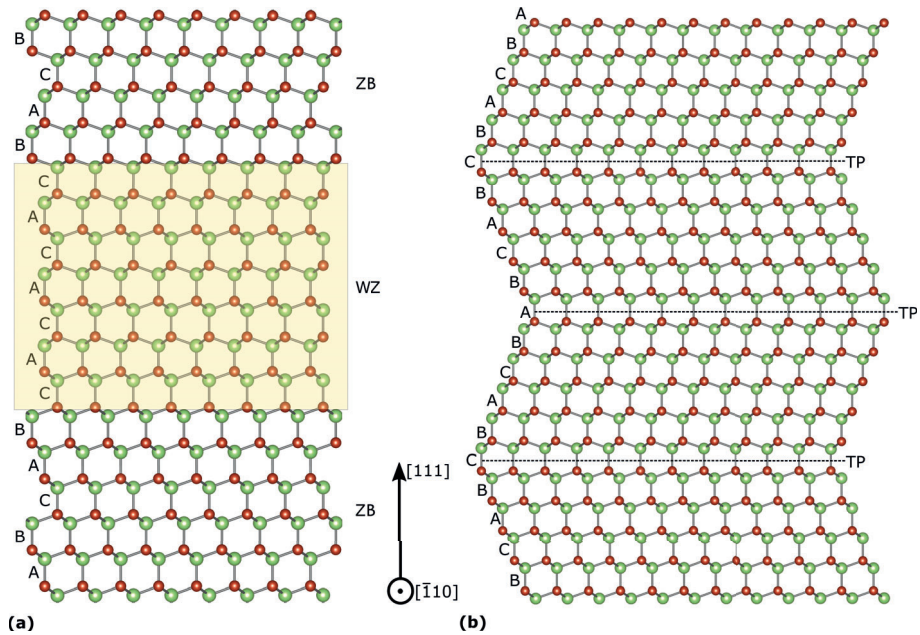

Figure 2.2: Schematic structure of **(a)** mixed ZB and WZ crystal phases and **(b)** twin planes in III-V nanowires.

geometry, even the structure that is not stable in bulk form can be found for most of the III-V materials. For example, the WZ structure is not stable in bulk GaAs, but can exist in GaAs nanowires. Even a mixture of the two phases within the same nanowire is possible, a phenomenon known as polytypism and illustrated in Figure 2.2 (a) [44]. By varying the growth conditions, the switching between WZ and ZB structure could be controlled within the nanowire [45]. Since the crystal structure affect the band structure of the material this could for example be utilized to form quantum dots [46]. However, unwanted polytypism may constitute a problem in other applications. For example, theoretical studies have shown that segments of WZ structure in otherwise ZB GaAs nanowires can reduce the conductance significantly [47].

Another phenomenon that is common in ZB III-V nanowires is the formation of twin planes (TP). A TP arises when the crystal orientation is rotated 60° along the [111] axis, see Figure 2.2 (b), and this can occur spontaneously during bottom-up growth of GaAs nanowires. A high density of TPs in the ZB structure may reduce the electron and hole mobilities [47]. However, if the average distance between TPs is >25 nm, the effect on the electron mobility is insignificant [48]

2.3 Nanowire solar cells

Nanowire solar cells is a promising technology for high-efficiency, low cost solar cells. In order to understand the potential of using nanowires in solar cells, it is necessary to have an understanding of the principles of conventional solar cells. This section therefore starts with an introduction to the theory of conventional solar cells, then continues to the design and advantages of nanowire solar cells. Lastly, different techniques for characterizing nanowire solar cells are discussed.

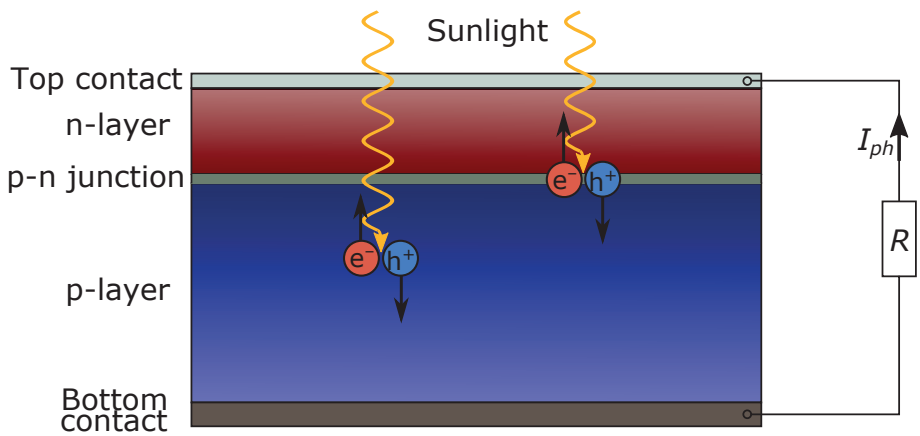

Figure 2.3: Schematic structure of a conventional solar cell. The built-in field at the p-n junction separates the charge carriers generated by absorption of sunlight, giving rise to a photocurrent.

A solar cell is a device capable of converting solar energy into electrical energy. Figure 2.3 shows the general design of a conventional solar cell. The active part is composed of a semiconductor doped to form a p-n junction. Here, the sunlight is absorbed by the semiconductor, and in this process electron-hole pairs are created. These mobile charges are subsequently separated by a built-in electric field that arises at the junction. Electrons go into the n-doped part and holes go into the p-doped part. If the p- and n-doped regions are electrically connected by an external circuit, a current will flow in order to equalize the potential of the two regions. This current is called photocurrent, I_{ph}, and can be used to power an electrical device, or charge a battery for example.

2.3.1 The p-n junction

Evidently, the p-n junction plays a key role in the function of a solar cell. Without it, there would be no separating mechanism for the generated electron-hole pairs, and no electrical current would be generated by the cell. To a large extent, it is the physical properties of the p-n junction that governs the function of a conventional solar cell, and the details of those properties will be discussed in this section.

In an intrinsic semiconductor, the Fermi energy (E_F) is in the middle of the gap between the conduction band and the valence band, but it can be shifted by doping the semiconductor. In an n-doped semiconductor there is an excess of free electrons in the conduction band, and E_F is shifted upwards, see Figure 2.4 (a). In a p-doped semiconductor there is an excess of free holes in the valence band, and E_F is shifted downwards, see Figure 2.4 (b).

If the n-doped and p-doped regions of the semiconductor are brought into physical contact, the Fermi-levels will become aligned throughout the whole material when

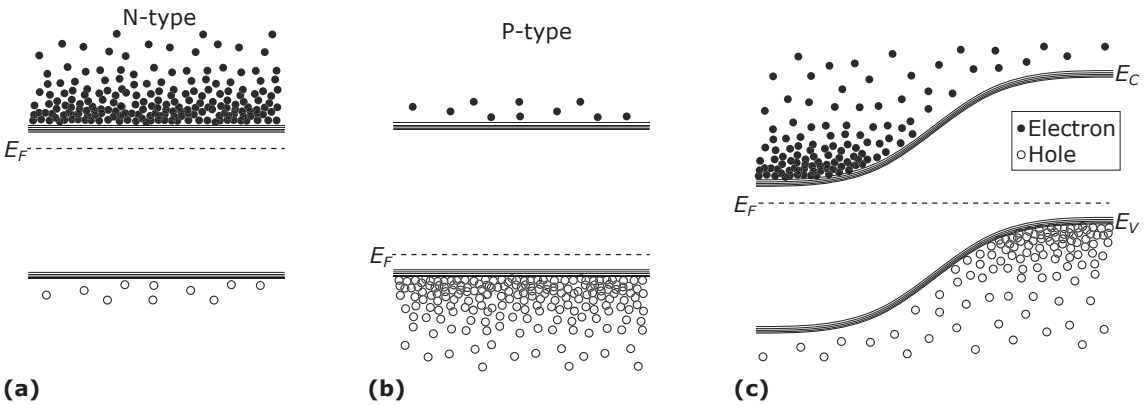

Figure 2.4: **(a)** Band diagram of a n-doped semiconductor. The Fermi energy is closer to the conduction band than the valence band. **(b)** Band diagram of a p-doped semiconductor. The Fermi energy is closer to the valence band than the conduction band. **(c)** Band diagram of a p-n junction in equilibrium. The Fermi-levels are aligned which results in a slope in the conduction and the valence band.

equilibrium is reached [49]. Still, deep into the n-doped (p-doped) region E_F will remain close to the conduction (valence) band. As a result, there will be a slope in the energy of the conduction and valence band in the region at the p-n junction, see Figure 2.4 (c), meaning that there is an electric field across this region. The physical origin of this field can be explained through the following reasoning: The n-doped region has an excess of free electrons and the p-doped region has an excess of holes. When they are brought into contact there will accordingly be a diffusion force on the electrons towards the p-doped region and a diffusion force on the holes towards the n-doped region. When the electrons diffuse to the p-side, they will recombine with the holes there and leave behind uncompensated positive charges in the form of immobile donor ions, see Figure 2.5 (a). Analogously, the holes diffusing over to the n-side will leave behind a negative charges. These growing charges will give rise to an electric field that counteract the diffusion force on the charge carriers. When equilibrium is reached the diffusion force and the electric field force will completely cancel each other out. The region where the field is present is called the depletion layer, because the free charge carriers are almost depleted here [50].

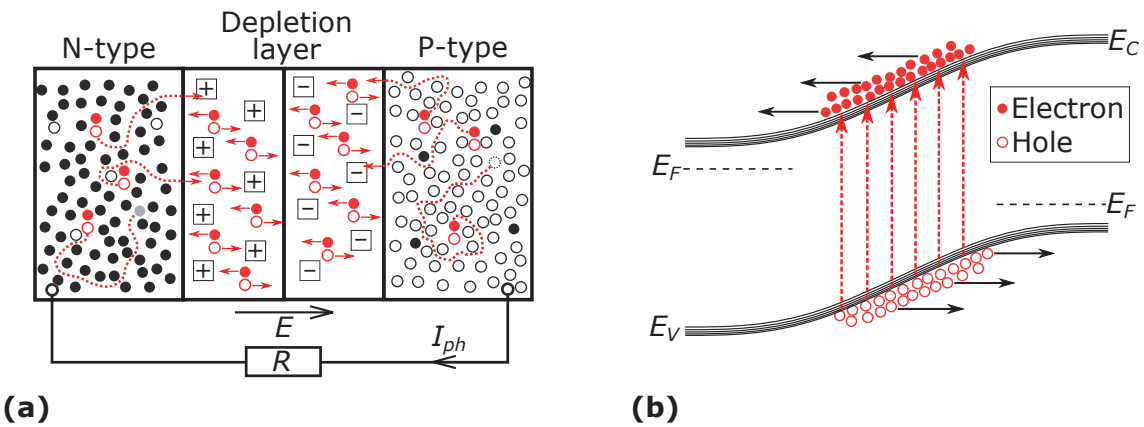

Figure 2.5: **(a)** Cross section of a p-n junction under illumination. The field across the depletion layer arises due to uncompensated ion charges. Charge carriers generated in the depletion layer are separated directly by the built-in field. Charge carriers generated in the neutral regions need to diffuse to the depletion layer to get separated, and may recombine before they get there. **(b)** Band diagram of a p-n junction under illumination. The generated electrons and holes are separated by the built-in field. This results in a difference in Fermi energies between the n-side and the p-side, and gives rise to a photocurrent.

When the p-n junction is illuminated by light, the photons could be absorbed and electron-hole pairs created. The field across the junction will act as a separator, forcing the electrons to move into the n-doped region and the holes to move into the p-doped region, illustrated in Figure 2.5 (a) and (b). The concentration of electrons in the n-doped region and the concentration of holes in the p-doped region will then be higher than the equilibrium case. This will split the Fermi-levels of the two regions, and be a driving force for the electrons to go to the p-side and holes to go to the n-side through the external circuit [50], giving rise to a net photocurrent.

Not all photons will be absorbed inside the depletion layer though. Some of them will be absorbed some distance away from the junction, either in the n-doped or the p-doped region. The generated minority carriers (electrons in the p-type region and holes in the n-type region) first need to diffuse to the junction in order for the built-in field to force them into the opposite region, see Figure 2.5 (a). While they are diffusing, there is a probability that they recombine, meaning that an electron in the conduction band fills a hole in the valence band. The charge carriers that recombine before reaching the junction will not contribute to the photocurrent. Recombination is discussed in further detail in section 2.3.3.

The built-in field of a p-n junction acts as a barrier for majority carriers (holes in the p-type region and electrons in the n-type region). If an external electrical bias is applied, this barrier can be either increased or decreased, depending on the polarity. In the so called forward bias condition, with the positive pole connected to the p-side, the barrier is lowered and the majority carriers can pass the junction into the opposite region, see Figure 2.6 (a). Since the concentration of majority carriers is high in a doped semiconductor, the current in the forward bias regime can become large. The energy distribution of the majority carriers can be approximated with a Maxwell-Boltzmann distribution. As the voltage is increased and the barrier is reduced more and more, the number of electrons and holes that can pass the depletion layer will therefore increase exponentially, and the forward bias current will have an exponential voltage dependence [49].

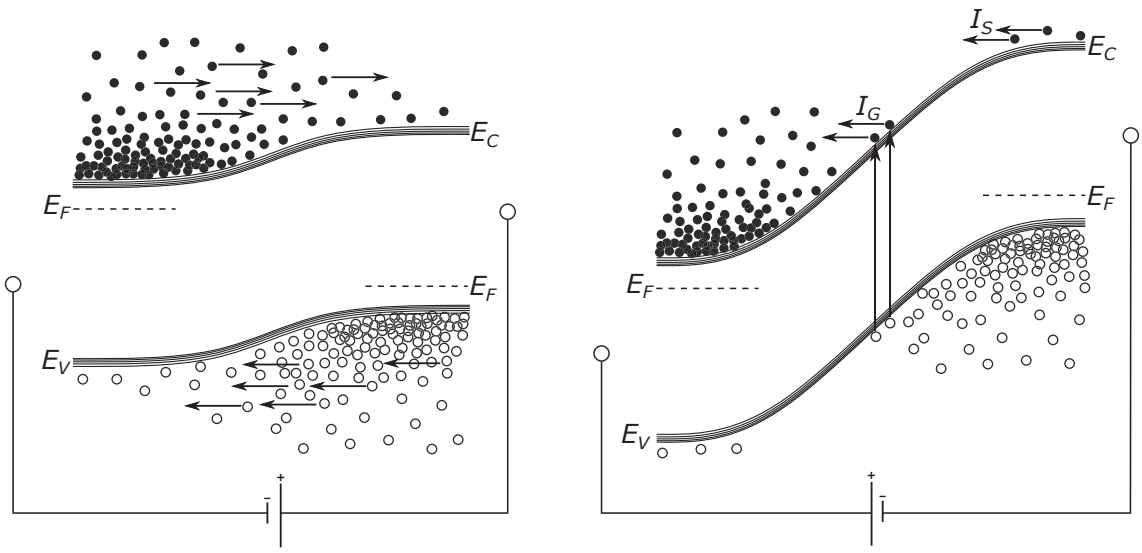

Figure 2.6: **(a)** Band energy diagram of a forward biased p-n junction. The Fermi levels of the p- respectively the n-side are split up, causing the energy barrier to decrease. **(b)** Band energy diagram of a reverse biased p-n junction. The Fermi levels of the p- respectively the n-side are again split up, but in the other direction compared to forward bias, causing the energy barrier to increase.

In the reverse bias condition though, the barrier is increased as a result of the additional voltage drop over the junction, see Figure 2.6 (b). In this situation,

there are two types of currents that can flow, the generation current I_G and the saturation current I_S. I_G is caused by the thermal generation of charge carriers in the depletion layer, which will be separated by the field at the junction. I_S is constituted of minority carriers that passes the junction, i.e. electrons that are swept by the field from the p-side to the n-side, and holes that are swept in the other direction. Since the concentration of minority carriers is usually very small compared to majority charge carriers in a doped semiconductor, I_S will take small values. As the reverse bias increases, the field strength across the junction will increase, but the concentration of minority carriers will remain the same. I_S will therefore be independent of the applied voltage, hence the name saturation current [49].

Both I_G and I_S are usually regarded as negligibly small, and in that case the p-n junction is current rectifying, meaning a current can only flow in one direction. The current through a p-n junction as a function of applied bias, $I(V)$, can be modeled by the Shockley equation:

$$I = I_S \left[\exp\left(\frac{qV}{nk_BT} \right) - 1 \right]. \tag{2.1}$$

Here q is the elementary charge, k_B is the Boltzmann constant, T is the absolute temperature, and n is the so called ideality factor of the junction. This equation clearly fulfills the requirement that the current should increase exponentially at positive bias and quickly stabilize at I_S at negative bias. I_G is not taken into account in this model. Furthermore, I_S can be related to the band gap energy (E_g) of the junction through the expression

$$I_s = Ce^{-E_g/nk_BT}, \tag{2.2}$$

where C is a constant related to the semiconductor [51].

2.3.2 Solar cell I-V characteristics

As mentioned earlier, the p-n junction is the basis of a conventional solar cell. Therefore, we can use the Shockley equation as a basis to model the I-V characteristics of a solar cell. However, some additions need to be made to make the model accurate. First of all, in a solar cell device the p-n junction needs to be connected to an external circuit in order to harvest the electrical energy. A finite resistance will always be present in this circuit and especially at the contacts between the circuit and the semiconductor. This resistance will be in series with the p-n junction, and is labeled R_{se} in the model. Furthermore, in practical devices there may exist a current path in parallel with the p-n junction. It can be the result of inhomogeneuos doping or bad insulation between the top and bottom contact. This is included in the model by a so-called shunt resistance R_{sh}, in parallel with the junction. Finally, the pho-

tocurrent, I_{ph}, that is generated when the solar cell is illuminated can be represented by a current generator in the model. The direction of this current will be the same as the reverse bias current. The equivalent electrical circuit of this model is shown in Figure 2.7 (a). Here the p-n junction is represented by a diode since it is current rectifying. With these additions, equation 2.1 becomes

$$I = \frac{V - R_{se}I}{R_{sh}} + I_S \left[\exp\left(\frac{q(V - R_{se}I)}{nk_BT} \right) - 1 \right] - I_{ph}. \tag{2.3}$$

This is known as the single diode model for solar cells [52].

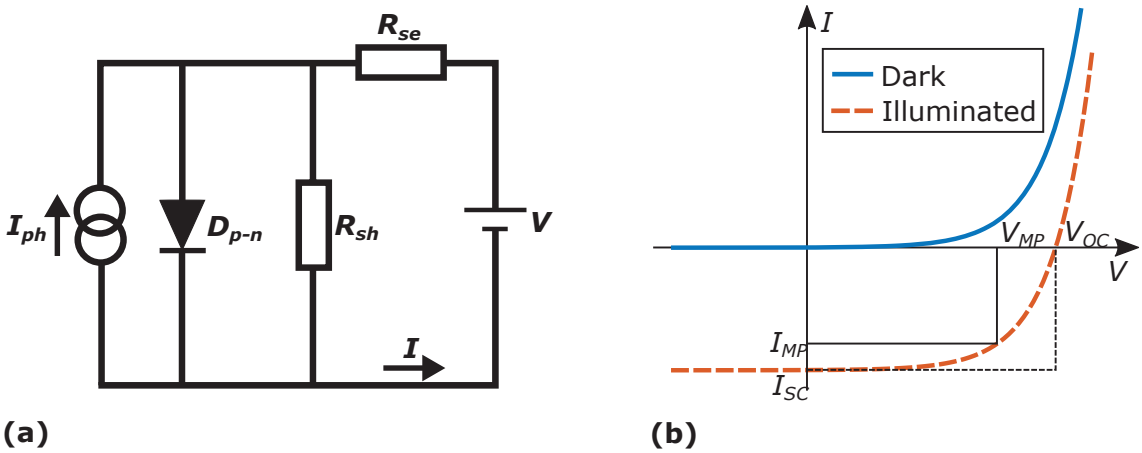

Figure 2.7: **(a)** Equivalent circuit of a non-ideal solar cell using the single-diode model. **(b)** I-V characteristics of an ideal solar cell. In the dark state the current is practically zero in the reverse bias regime and has an exponential dependence on the voltage in the forward bias regime. In the illuminated state the I-V curve is a superposition of the dark I-V curve and the photocurrent I_{ph}. The important parameters I_{SC} and V_{OC} can be extracted from the illuminated I-V curve.

Figure 2.7 (b) shows the I-V characteristics of an ideal solar cell under dark and illuminated conditions. In this case, the I-V characteristics during illumination follows the superposition principle, which means it is the exact same I-V characteristics as in the dark, only shifted downwards by the absolute value of I_{ph}. From the I-V characteristics during illumination it is possible to extract some important parameters that are commonly used to assess the performance of solar cells. The short circuit current I_{SC} and the open circuit voltage V_{OC} are two such parameters. I_{SC} can be found by reading the value of the current where the I-V curve intersects the y-axis, and V_{OC} is the value of the voltage where the I-V curve intersects the x-axis, see Figure 2.7 (b). If the effect of R_{se} and R_{sh} is negligible, then $I_{SC} = I_{ph}$ and equation 2.3 can be used to find a relation between I_{SC} and V_{OC}:

$$V_{OC} = \frac{nk_BT}{q} \ln\left(\frac{I_{SC}}{I_S} + 1 \right) \tag{2.4}$$

The resistance of the load in the external circuit will determine in which point on the I-V curve the solar cell will operate, i.e what the values of the current and voltage will be. If the solar cell is operated at short circuit conditions, the current will have the highest possible value, I_{SC}, but the voltage will be $V = 0$. The power output in this situation will therefore be $P_{Out} = IV = I_{SC} \cdot 0 = 0$. If it is operated at open circuit conditions the voltage will have the highest value, V_{OC}, but the current will be zero so again, $P_{Out} = 0$. Somewhere in between these extremes an optimum will exist, generating the highest possible P_{Out}. This is the maximum power point $[V_{MP}, I_{MP}]$, indicated in Figure 2.7 (b). The third parameter for assessment, the fill factor (FF), is then defined as

$$FF = \frac{I_{MP}V_{MP}}{I_{SC}V_{OC}} \tag{2.5}$$

Geometrically, FF is the ratio between the area of the solid line rectangle and the dashed line rectangle in Figure 2.7 (b). The fill factor can thus be said to be a measure of the "squareness" of the illuminated I-V curve, and the more square the curve is, the higher is the generated power. Further, the power conversion efficiency (PCE) of a solar cell is defined as

$$PCE = \frac{P_{Out}}{P_{In}} = \frac{FF * I_{SC} * V_{OC}}{P_{In}}. \tag{2.6}$$

P_{In} is the input power coming from the light, which is 100 mW per cm^2 for 1 Sun illumination.

2.3.3 Loss mechanisms in solar cells

Real solar cells can never be truly ideal and several mechanisms exists that may introduce losses. First of all, the parasitic resistances R_{se} and R_{sh} may have a detrimental effect on the solar cell performance, see Figure 2.8. A large R_{se} reduces the FF. A small R_{sh} reduces both FF and V_{OC}, and a combination of both large R_{se} and small R_{sh} additionally reduces I_{SC}. All these effects reduces the PCE of the solar cell.

Another loss mechanism in solar cells is recombination. Electrons and holes generated in a semiconductor have a limited lifetime, and will therefore eventually recombine. There exist different recombination processes, and they can be divided into radiative recombination and non-radiative recombination. In order for a solar cell to achieve the theoretical maximum output voltage, the recombination processes should be strictly radiative. Radiative recombination means that a photon is produced when an electron-hole pair recombines. This photon can then be recycled within the absorbing material to create another electron-hole pair, a process that helps maintaining a high concentration of charges and thus a high voltage difference

between the n- and p-doped regions during illumination. Non-radiative recombination on the other hand only results in loss of available charge carriers and reduces the V_{OC} of the solar cell [53]. Non-radiative recombination can occur when electronic states are introduced within the band gap because of defects in the crystal structure or dangling bonds at the surface of the semiconductor [54]. It is therefore important to have high crystal quality and in some cases surface passivation, in order to reach a high PCE. The recombination processes are taken into account by the ideality factor, n, in the single diode model. For the ideal case, with strictly radiative recombination occurring in the neutral regions, $n = 1$. However, for strictly non-radiative recombination occurring in the depletion region of the junction, $n = 2$. A mixture of the two processes results in $1 < n < 2$. If additional junctions are present in the circuit, for example at the contact, it is possible that $n > 2$ [55].

A more fundamental cause of energy loss in solar cells is thermalization. Whenever a photon, with energy higher than E_g of the active material in the solar cell, is absorbed, an electron will be excited to an energy level above the bottom of the conduction band, see Figure 2.9 (a). This excess energy will rapidly be transferred into the semiconductor crystal in the form of lattice vibrations, in a process termed thermalization. Therefore, the maximum energy that can be harvested from an absorbed photon is E_g, regardless of the initial photon energy. At this point, it would seem that a larger band gap always results in a higher efficiency, since then a lesser part of the photon energies is lost through thermalization. However, since no photons with energies $< E_g$ can be absorbed, a larger E_g will result in fewer absorbed photons. Therefore, the optimal choice of E_g will be a compromise between minimizing thermalization losses and maximizing absorption, and it will depend on the spectral irradiance of the incoming light. Figure 2.9 (b) shows the AM1.5 standard solar spectrum [56] and the usable intensity for $E_g = 1.7$ eV and $E_g = 1.1$ eV under the assumption that every absorbed photon contributes with an energy equal to E_g and no photons with energies less than E_g get absorbed. It is evident that a high band gap solar cell makes better use of the high energetic (short wavelength) photons

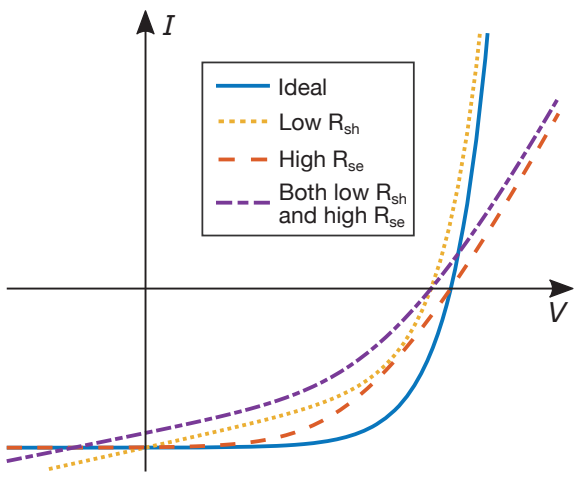

Figure 2.8: Illustration of how R_{se} and R_{sh} affects shape of the illuminated I-V curve and the performance of a solar cell.

but cannot use the low-energetic ones at all, while a low band gap solar cell absorbs a higher number of photons, but makes poor use of the high-energetic ones. The optimal band gap for the AM1.5 spectra must therefore be somewhere between 1.7 and 1.1 eV, more particularly at 1.34 eV. At this band gap, the maximum theoretical efficiency for a p-n junction solar cell that is only limited by radiative recombination is 33.16% [57]. This is the so called detailed balance limit [58], famously known as the Shockley-Queisser limit.

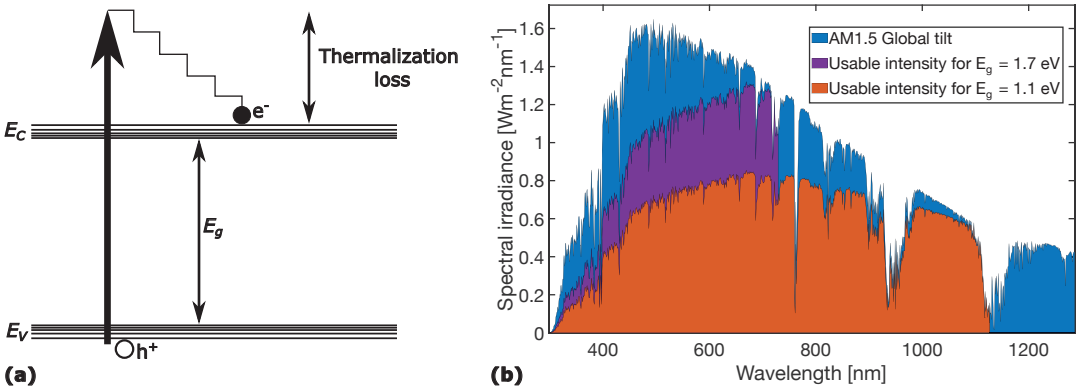

Figure 2.9: **(a)** Principle of thermalization. A photon with energy larger than E_g excites an electron to an energy level higher than E_C. The excess energy is transferred to the crystal lattice in the form of phonons. **(b)** The AM1.5 solar spectrum and the maximal usable intensity for a single band gap solar cell with $E_g = 1.7$eV and $E_g = 1.1$eV.

In order to overcome the compromise between high absorption and low thermalization losses, materials of different band gaps are stacked upon each other in multijunction solar cells. In this way, the Shockley-Quiesser limit can be beaten and the record efficiency for a multijunction solar cell is 39.5 % at 1 Sun illumination [59], and 47.4 % under concentrated sunlight [60], which is the highest reported efficency for all photovoltaic technologies [61]. The record-breaking multijunction solar cells are often composed of III-V semiconductors. However, the fabrication of such cells is complicated because only a small lattice mismatch between different materials can induce a high density of defects, detrimental for the cell. As a result, this type of solar cells are highly expensive, and therefore mainly used in specialized circumstances where a high power density is needed and cost is not critical, such as space applications [62].

At present, Si solar cells dominate the market because it is a mature technology. However, their efficiencies are still a bit from the Shockley-Quiesser limit and have not made significant progress for a long time [63]. Many new solar cell technologies have emerged in the latest decades, with the ambition of outperforming the existing Si technology and making solar cells really competing with non-renewable sources. Two main strategies are used, either lower the cost so much that the PCE is not critical, or increase the PCE. In the next section, we shall see that nanowire solar cells have the potential of doing both.

2.3.4 Design and function of nanowire solar cells

The term nanowire solar cell refers to a photovoltaic device where arrays of semiconductor nanowires are the main and active component, responsible for the absorption of photons and the generation and separation of charge carriers. A typical design of such a device is shown in Figure 2.10 (a). Here arrays of vertically aligned nanowires are standing on a substrate. Each nanowire contains a charge separating p-n [64] or p-i-n junction [65], either in the axial [66] or radial direction [67], see Figure 2.10 (b). The back contact is typically established through a metal contact to the substrate. The front contact usually consists of a layer of transparent conductive oxide (TCO) such as indium tin oxide or aluminum zinc oxide [68], deposited at the top surface of the nanowires. If any metal seed particle is still remaining at the top of the nanowires from the growth process, this is usually removed by wet etching before establishing contact, in order to avoid light reflection [69, 70]. For mechanical stability and electrical insulation, the nanowire arrays are usually embedded in a transparent polymer such as benzocyclobuten [71, 72], only exposing the tip to the TCO.

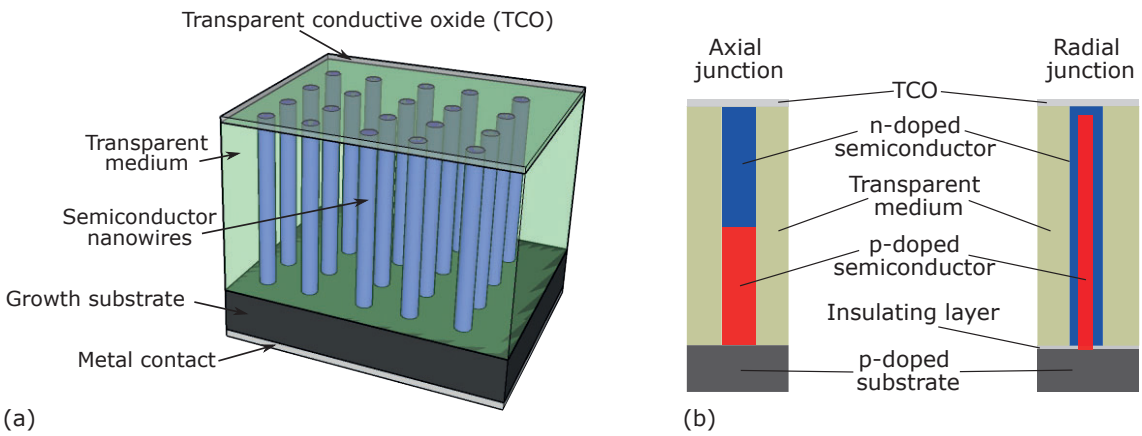

Figure 2.10: **(a)** Schematic structure of a nanowire solar cell. **(b)** Schematic illustraion of the difference between the axial junction geometry and the radial junction geometry

In conventional solar cells, the absorbtion of sunlight scales linearly with the projected area of the cell. This is intuitive and one can describe the situation with ray optics. The rays from the sun that do not hit the surface have no chance of becoming absorbed in the material. The situation becomes quite different for sub-wavelength structures. In this case, the wave nature of the light can give rise to resonance effects, dependent on the size, shape and chemical composition of the structures. Such resonance effects may confine the light within the structure and enhance the absorption. Electrodynamic modeling show that semiconductor nanowires with diameters up to several hundred nanometers exhibit this sort of resonance effects [73]. In fact, it has been experimentally shown that a single, vertical GaAs nanowire can absorb sunlight corresponding to an area approximately 8 times larger than its physical cross sectional area [13]. This decoupling of the absorption and physical

cross section means that a single nanowire solar cell can have a theoretical apparent efficiency >100% [74]. Of course, such efficiencies are not possible in large-area solar cells composed of nanowire arrays, because in that case also the area between the nanowires are included in the efficiency-calculation. Nevertheless, the waveguiding resonance effect enables a nanowire array (NWA) to be quite sparse and still absorb most of the incoming sunlight, see Figure 2.11. In fact, theoretical studies using finite-difference time-domain (FDTD) simulations have shown that a GaAs nanowire array with optimized diameter and pitch (distance between nanowires) can absorb more than 90% of the above-band gap incoming sunlight, which is significantly more than a GaAs film of the same thickness (2 μm), even though the volume filling ratio of the NWA is only 0.196 [75]. This means that the material consumption could be reduced drastically in nanowire solar cells compared to thin films.

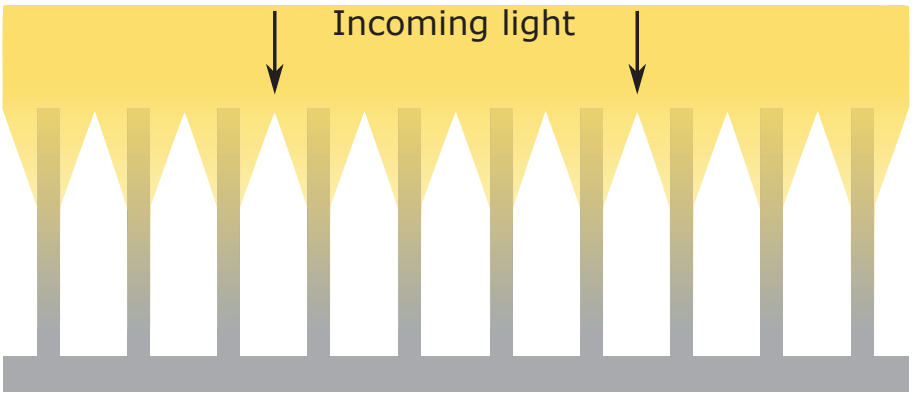

Figure 2.11: Enhanced absorption in nanowire array. Due to the wave nature of light and the sub-wavelength nanowire diameter, the nanowires act as waveguides for the incoming light and concentrates the light. This enables the nanowire array to absorb the incoming light without filling up the whole solar cell volume.

Another advantage with the nanowire design is that a NWA can have much lower reflectance than a thin film. This is because the effective refractive index of a NWA is lower than for a bulk sample of the same material [76]. The more sparse the NWA is, the closer the effective refractive index will be to 1 as that of the surrounding air. It is also possible to make conical nanowires to make a graded-index anti-reflective coating [77]. Dual-diameter or base-tapered nanowires can be used to optimize the absorption and material usage [78, 79] .

The radial junction geometry offers a potential advantage over planar junctions, since it decouples the optical and electrical thickness of the solar cells. This means that the nanowires can be made long, ensuring full absorption of the incoming light, without increasing the diffusion path lengths for the generated charge carriers. However, the radial junction geometry also implies a large junction area, which increases the I_S of the cell [15].

In a conventional solar cell with a non-active absorbing substrate, a large portion of the photons generated by radiative recombination will be emitted into the substrate

and not contribute to the output power [53]. In a nanowire solar cell though, fewer photons will be emitted into the substrate due to the waveguiding effect. This leads to an increased open circuit voltage, and as a result, the Shockley-Queisser limit for a NWA can be higher than the equivalent thin film cell [80]. Tapered nanowires can even be used to guide the emitted photons back in the opposite direction of the incoming photons, reducing the entropy losses associated with randomly emitted photons, thus further improving the optimal efficiency of nanowire solar cells [81].

A limitation with thin-film solar cells is that there has to be a high match between the lattice parameter of the growth substrate and the active layer to avoid high concentrations of detrimental dislocations [82]. As a consequence, high-efficient III-V thin films are usually grown on substrates made of expensive materials such as Ge. The lattice-matching constraint also severely limits the choices of material combinations in multijunction solar cells, where layers of different band gap need to be stacked upon each other [83]. In nanowire solar cells though, highly lattice mismatched structures are possible because the high surface-to-volume ratio of the nanowires enables efficient strain relaxation without dislocations [84]. For example, highly crystalline nanowires composed of GaAs, InP and GaAsP can be grown on inexpensive Si substrates [14, 85, 86]. This lowers the cost and opens up the possibility for tandem junction solar cells [87].

There are many advantages with the nanowire design but there are also some drawbacks. The large surface-to-volume makes the nanowire solar cell vulnerable to surface recombination. Surface cleaning and passivation have been successfully applied to mitigate this [88–90], however there is a need for further understanding and improvement of surface passivation [91]. Furthermore, the small volume of the nanowires puts high demands on the control of the doping distributions, especially in nanowires with radial junctions where the thin layers are at risk of getting fully depleted. Even if separate solutions have been found to many of the critical issues, a remaining challenge is to combine them in a single device. In order to utilize the full potential of nanowire solar cells, one needs to optimize both the photonic properties by controlling the geometrical parameters of the NWA, and the electronic properties by having a high degree of control over doping and contact formation, all while keeping the fabrication cost low [15]. One prerequisite for developing nanowire solar cells is establishing versatile and reliable techniques for characterization and assessment of individual nanowires, which the next section will address.

2.3.5 Characterization of nanowire solar cells

Assessment measurements under standardized conditions on full nanowire array cells are important to provide a fair comparison to other solar cell techniques [92], however, they give limited insight to what needs to be optimized in order to increase the efficiency further. There is a need to be able to investigate the properties of individual nanowires since they are the building blocks of the solar cells. Of course, the small size of nanowires makes it challenging to study them. One common approach

is to transfer a single nanowire from the growth substrate and place it horizontally on an insulating substrate, see Figure 2.12 (a). Electrical contacts to both ends of the nanowire can then be established by electron beam lithography and metal evaporation [93, 94]. In the case of radial junction nanowires, an additional step is required where the core is revealed by an etching process at one end of the nanowire, in order to contact both sides of the junction [95]. This setup is well suited for characterization of electrical properties inherent to the nanowires, such as I-V characteristics [96], charge generation and collection [90], and minority carrier diffusion lengths [97]. However, regarding characterization of optical properties, results obtained from horizontal nanowires will not be directly comparable to vertical nanowires since the waveguiding resonance effects differ significantly between the two geometries [98, 99].

Another way to characterize individual nanowires is to fabricate a complete solar cell containing only one single nanowire, see Figure 2.12 (b). In this way, the optical properties in the vertical geometry may be studied in detail, and the strong light trapping effect may be observed [13, 100]. However, rigorous sample preparation is needed for each nanowire to be studied.

A third way to characterize individual nanowires is to use an in situ nanoprobing instrument, see Figure 2.12 (c). In this way, individual nanowires in array samples can be selected and contacted with high precision. With this method, charge collec-

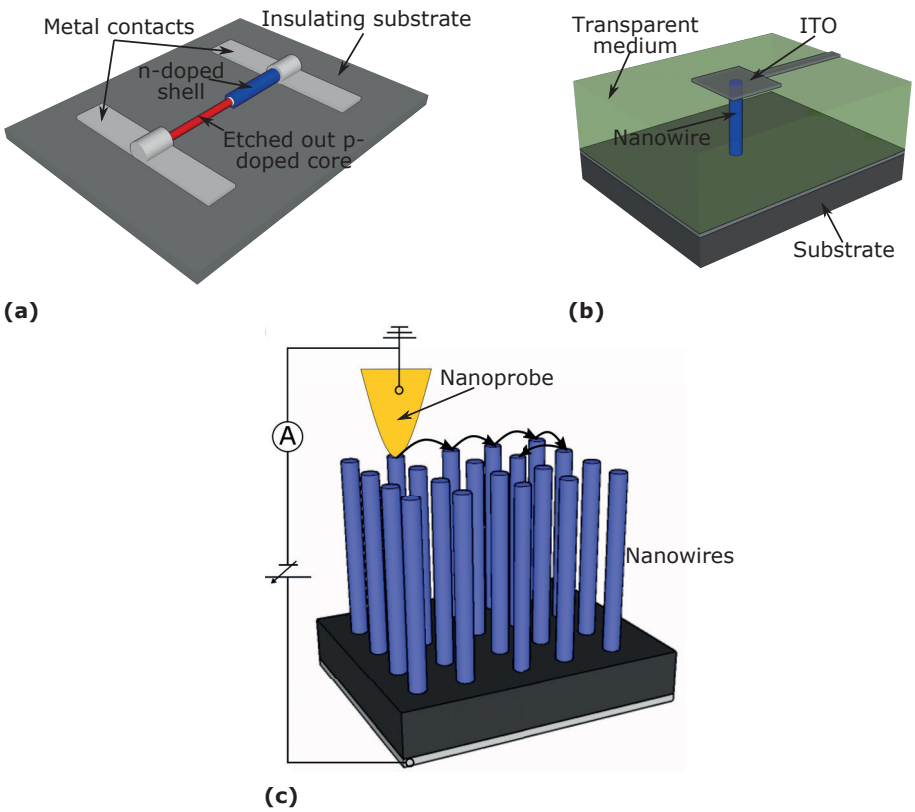

Figure 2.12: Three different techniques for characterizing single nanowire solar cells.

tion properties [101, 102] and I-V characteristics during both dark and illuminated conditions of single solar cell nanowires can be studied [103]. In Paper I, we describe this technique in detail and use it to study single GaAs nanowire solar cells. The advantage of this method is that the measurements can be carried out directly on nanowire array samples on growth substrates without the need of special sample preparation.

3. 2D transition metal dichalcogenides (TMDCs)

Transition metal dichalcogenides (TMDCs) are a group of materials with the formula MX_2, where M is a transition metal and X is a chalcogen element. Bulk TMDCs have been known for a long time and their properties range from metallic and semiconducting to insulating, depending on the specific composition and structure [16]. Many TMDC crystals (with M from group 4-7) form atomic layered structures, with strong covalent intralayer bonds and weak van der Waals forces between the layers, similar to graphite. The discovery of graphene in 2004 [104] and the subsequent research and development of 2D material fabrication, characterization and functionalization sparked a renewed interest in TMDCs, this time in their atomically thin, 2-dimensional form [105]. The 2D geometry leads to new physical properties and allows for ultrathin components important for miniaturization of devices.

3.1 Fabrication and transfer methods

The layered nature of TMDCs allows mono- and few layer samples to be produced by mechanical exfoliation. In practice, this could be done by hand using adhesive tape, the so called Scotch tape method [106], see Figure 3.1. The principle of this technique is to start with a bulk crystal, pull off the topmost layers of the crystal using adhesive tape, then fold the tape many times to get thinner flakes of the crystal. The tape is then pressed against a flat substrate, commonly Si or SiO_2, then lifted slowly. If the adhesion between the substrate and the top surface of a flake is stronger than the adhesion between two layers within the flake, exfoliation onto the substrate will occur. The flakes produced in this way will be randomly distributed both in size and position, and their thickness can vary from monolayer to hundreds of layers. Typically, the yield of this method to produce usable TMDC-flakes is low. There are ways to increase the chance of getting large monolayer flakes, for example by heating or surface treatment of the substrate [107], or using gold-mediated exfoliation [108, 109]. If control of the position of individual flakes is required, the flakes can be transferred from the tape to a viscoelastic, transparent stamp, usually made of polydimethylsiloxane (PDMS). The stamp could then be aligned over the substrate using an optical microscope and a mechanical translation stage. By pressing the stamp onto the substrate and then slowly removing it, deterministic positioning of individual flakes is enabled [110]. This method can also be used to pick up flakes from a substrate, by adding another, more sticky, layer of transparent polymer on

the PDMS-stamp. In this way, several flakes (of different TMDCs or other 2D-materials) can be picked up one after another, forming a heterolayer stack [111]. The stack can then be transferred to a substrate by increasing the temperature so that the polymer melts. Mechanical exfoliation is a readily accessible method that produces 2D-flakes of high crystalline quality, and therefore it is the method of choice for lab-scale studies of TMDCs. The main drawbacks of mechanical exfoliation is its relatively low yield and lack of scalability. Liquid phase exfoliation is another top-down method where 2D-flakes are produced from a bulk crystal in a solution. The separation of the flakes can be initiated mechanically by grinding, stirring, sonication etc. or by atomic intercalation [112]. This is a promising method for simple, low cost and scalable production, however it usually yield 2D-flakes of small size and of lower quality and purity than all-dry mechanical exfoliation [113]. There are also a number of bottom-up techniques for fabrication of 2D TMDCs, including chemical vapour deposition (CVD) and atomic layer deposition (ALD). CVD produces high quality monolayer flakes but often with low yield and limited size [114]. ALD can produce wafer-scale MoS_2 thin films [115].

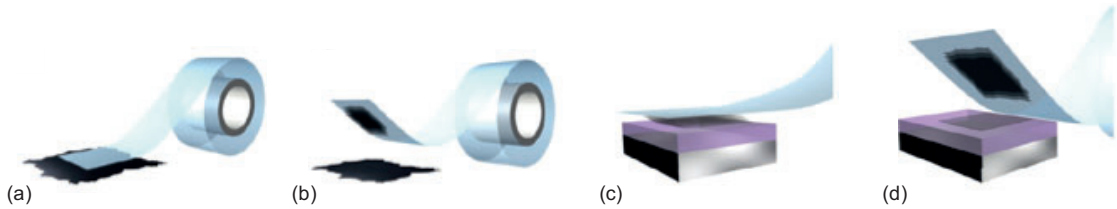

Figure 3.1: The Scotch tape method. **(a)** Adhesive tape is pressed against the top surface of a TMDC bulk crystal. **(b)** The tape is pulled off the crystal, and part of the crystal sticks to the tape. At this stage, the tape may be folded onto itself and then separated again several times. Each time, exfoliation will occur and result in thinner and thinner flakes. **(c)** The tape is pressed onto a substrate. **(d)** The tape is lifted slowly and exfoliation of thin flakes onto the substrate will occur. Adapted with permission from Phys. Scr. T146 (2012) 014006 (6pp). Copyright 2012 IOP Publishing

3.2 Microstructure and properties

One single layer of a TMDC consists of three atomic layers, with the metal atoms sandwiched between two layers of chalcogen atoms. The interlayer spacing is 6.15 Å for MoS_2, and similar for other TMDCs [116]. The three main crystal structure phases for TMDCs are 1T, 2H and 3R, see Figure 3.2 (a). The 1T structure has octahedral coordination of the metal atoms, and tetragonal symmetry. The 2H and 3R structures both has trigonal prismatic coordination of the metal atoms, but different stacking sequence of the layers. The 2H has 2 layers per repeat unit which results in hexagonal symmetry, and the 3R has 3 layers per repeat unit which results in rhombohedral symmetry. For MoS_2, only the 2H and 3R structures are thermodynamically stable and naturally occurring, with 2H being the most common

[16].

The attraction for 2D TMDCs lies in their rich physics and chemistry which allows functionality that is lacking in graphene. An example is the semiconducting property, most prominent in TMDCs with formula MoX_2 or WX_2 which have bandgaps in the range of 1-2 eV [117]. This enables high on-off ratios in field effect transistors (FET) [118], efficient light absorption/emission for photovoltaic applications [119] and existence of excitons that are stable due to the reduced Coulomb screening in 2D geometry [120]. Atomically thin TMDCs also have good electrical transport properties in relation to their thickness. While conventional 3D bulk semiconductor carrier mobilities degrade when scaled down below ∼3 nm, TMDCs have high carrier mobilities even at thicknesses below 1 nm [121], making them viable candidates as the active component in low-footprint electronics. Furthermore, TMDCs have properties that are tuneable with sample thickness. A bulk MoS_2 crystal has an indirect bandgap of 1.3 eV, but in few-layer samples the bandgap increases for every layer that is removed, see Figure 3.2 (b). In the last step, going from bilayer to monolayer, the crystal undergoes an indirect-to-direct bandgap transition [122]. The direct bandgap of 1.8 eV in monolayer MoS_2 results in strong photoluminescence [123] and may further enable optoelectronic applications. As mentioned previously, the weak interlayer forces allows stacking of different TMDCs, providing many possible heterostructures that could exhibit new properties [124]. It is also possible to rotate the layers with respect to each other to form Moiré patterns, giving rise to new electrical, optical and magnetic properties [125].

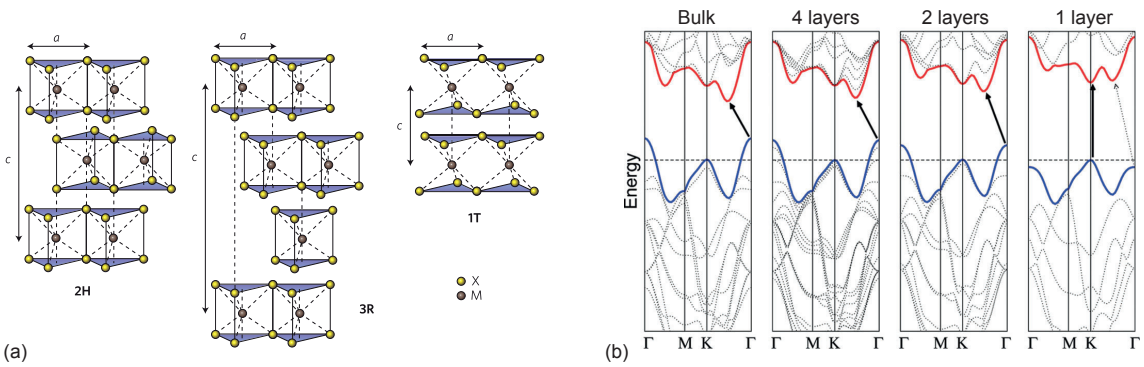

Figure 3.2: **(a)** The 2H, 3R and 1T crystal structure of TMDCs. Reprinted with permission from Nature Nanotech 7, 699–712 (2012). Copyright 2012 Springer Nature **(b)** Bandstructure of MoS_2 at different thicknesses. An indirect-to-direct bandgap transition occurs going from bilayer to monolayer. Adapted with permission from Nano Lett. 2010, 10, 4, 1271–1275. Copyright 2010 American Chemical Society

4. Elastic strain engineering (ESE)

Elastic strain engineering (ESE) refers to the tuning of a materials physical properties through elastic strain. Probably the most commercially successful example of ESE is in complementary metal organic semiconductor (CMOS) technology, where strained Si is used to enhance charge carrier mobilities, leading to faster switching of transistors [126]. In this chapter, a brief introduction to the principles of ESE is given, followed by a discussion about how ESE has been and can be applied in the specific cases of III-V semiconductor nanowires and 2D TMDCs.

4.1 Concept of ESE

In crystalline materials, elastic strain is defined as relative lattice displacement compared to the relaxed state, see Figure 4.1. In this 2 dimensional example, the lattice is elongated along the x-axis and the strain is $e_{xx} = \frac{a_2 - a_1}{a_1}$. In the general 3 dimensional case, strain can be completely described by six independent coefficients, $\mathbf{e} = (e_{xx}, e_{yy}, e_{zz}, e_{xy}, e_{yz}, e_{zx})$, where the three first coefficients represent elongation or contraction of the three basis vectors of the lattice, and the last three represent changes in the angles between the basis vectors [127]. The special case where $e_{xx} = e_{yy} = e_{zz}$ and $e_{xy} = e_{yz} = e_{zx} = 0$ describe pure hydrostatic strain which does not result in a change in the symmetry of the crystal lattice, only a change in the volume of the unit cell. All other combinations of the strain coefficients will induce some shear strain, which changes the shape of the lattice unit cell.

Strain can be induced in a solid by applying an external force. The force per unit area associated with strain is termed stress, which is also described by six

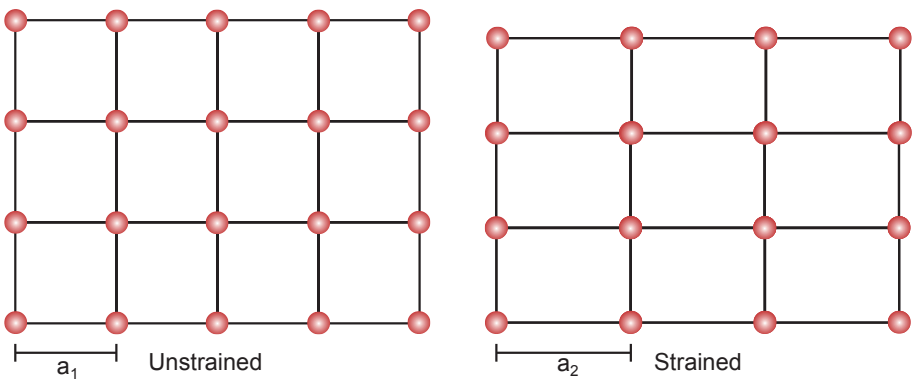

Figure 4.1: Comparison of an unstrained and strained lattice.

independent coefficients, $\tau = (\tau_{xx}, \tau_{yy}, \tau_{zz}, \tau_{xy}, \tau_{yz}, \tau_{zx})$. The strain is then related to stress according to

$$e_m = \sum_i S_{mi}\tau_i \tag{4.1}$$

where S_{mi} is the so called compliance tensor. For cubic materials, S_{mi} has only three independent components and can be represented by a 6×6 matrix [128]. In the simple case of an applied stress T along the x-axis only, $\tau = (T, 0, 0, 0, 0, 0)$, we may use the compliance tensor to find the resulting strain:

$$\begin{bmatrix} S_{11} & S_{12} & S_{11} & 0 & 0 & 0 \\ S_{12} & S_{11} & S_{12} & 0 & 0 & 0 \\ S_{12} & S_{12} & S_{11} & 0 & 0 & 0 \\ 0 & 0 & 0 & S_{44} & 0 & 0 \\ 0 & 0 & 0 & 0 & S_{44} & 0 \\ 0 & 0 & 0 & 0 & 0 & S_{44} \end{bmatrix} \begin{bmatrix} T \\ 0 \\ 0 \\ 0 \\ 0 \\ 0 \end{bmatrix} = \begin{bmatrix} S_{11}T \\ S_{12}T \\ S_{12}T \\ 0 \\ 0 \\ 0 \end{bmatrix}. \tag{4.2}$$

Evidently, the stress results in a strain not only along the x-axis, but along the y- and z-axis too. The compliance constants can be related to Young's modulus Y and Poission ration ν by

$$\mathrm{Y} = \frac{1}{S_{11}}, \nu = -\frac{S_{12}}{S_{11}} \tag{4.3}$$

for cubic systems [128]. In the example above, the strain could therefore be expressed as $\mathbf{e} = (\frac{T}{\mathrm{Y}}, -\frac{\nu T}{\mathrm{Y}}, -\frac{\nu T}{\mathrm{Y}}, 0, 0, 0)$.

The stress-strain relationship in Equation 4.1 holds as long as the sample stays within the elastic regime. If the stress becomes too high, the crystal either gets plastically deformed (ductile materials) or fractures (brittle materials). Plastic deformation is irreversible and imply propagation and/or nucleation of crystallographic defects which could lead to degradation of desirable electronic properties in semiconductors [54]. Elastic strain on the other hand is a reversible process where the atomic positions shift back and forth as stress is applied and removed. Since the lattice parameter and symmetry in a periodic crystal largely determines the physical and chemical properties of the material, these properties may be changed by elastic strain [22]. The principle of elastic strain engineering (ESE) is thus to reach desired properties by controlling the elastic strain. A parallel can be drawn to chemical alloying, where the principle is to change the composition of a material until you reach the desired properties. In a way, elastic strain engineering could be regarded as a form of mechanical alloying, where the variables are the strain components rather than the concentration of elements. By adding the six dimensions of strain to the parameter space, many new properties may become available. Alloying has been around since the Bronze Age, and the possibilities have been explored thoroughly

and the recipes for different material properties have been refined. Elastic strain engineering, despite the vast potential, has not been explored nearly as much. The reason is: for a significant change in properties, strain levels of > 1 percent are generally required. Conventional bulk materials can generally only withstand elastic strain levels <0.2% before before yielding or fracturing [8]. For thin films grown on lattice mismatched substrates, generally only up to 1% strain can be achieved without introducing defects [129]. The reason why real-life crystalline materials in general yield long before their ideal elastic limit is that they are not perfect crystals, they contain defects such as dislocations or cracks. When such a sample is exposed to external stress, dislocation glide or crack propagation occur rather than pure elastic strain. One solution to this problem is to let at least one characteristic length scale in the sample enter the nano-regime. It has been known for more than 70 years that the yield strength of bulk nanocrystalline materials are inversely proportional to the average grain size within the material, the so called Hall-Petch relationship [130] [131]. This effect is generally attributed to dislocation propagation blockage at the grain boundaries. More recently, it has been discovered that as the sample size itself is reduced to the nanometer scale, the yield strength increases and higher levels of elastic strain can be accommodated in the sample [132]. In this case, it is the reduction of defects that is the main reason for the improved strength. Because of the small size, the dislocations present in the sample cannot propagate far and are annihilated at the surfaces faster than they are multiplying. This leads to a dislocation starvation and significantly increases the yield strength [7]. Nanosized objects are also less probable to contain defects that could initiate cracks leading to brittle fracture, both for statistical reasons but also because many nanofabrication methods results in highly pristine, single crystal samples with atomically smooth surfaces [19].

Elastic strain affects the band structure of semiconductors. A qualitative understanding of the most important effects of strain and can be gained by symmetry considerations [128]. Strain can be divided into two parts, hydrostatic strain that change the volume of the unit cell and shear strain that affects the symmetry of the crystal. In general, an arbitrary stress will result in both hydrostatic and shear strain. Hydrostatic strain will shift the band gap of the semiconductor. Generally, a compressive strain will increase the band gap while a tensile strain will reduce the band gap. This could be understood intuitively by comparing the valence and conduction band with the bonding and antibonding state in a diatomic molecule. If the atoms are pushed together, the states will become further apart in energy and vice versa. Shear strains that lowers the symmetry of the crystal will lift the valence band degeneracy in cubic crystals. It may also induce splitting of conduction band valleys and band warping [128].

For a full prediction of strain impact on properties, advanced theoretical simulations are needed. Figure 4.2 shows an example of a simulation of the effect of strain on the band structure of GaAs, based on an 8-band $k \cdot p$ model [20]. The band gap shift and splitting of heavy- and light hole bands as a function of uniaxial strain along the [1 1 1]-axis is shown. Simulations like these are essential for a scientific approach in ESE.

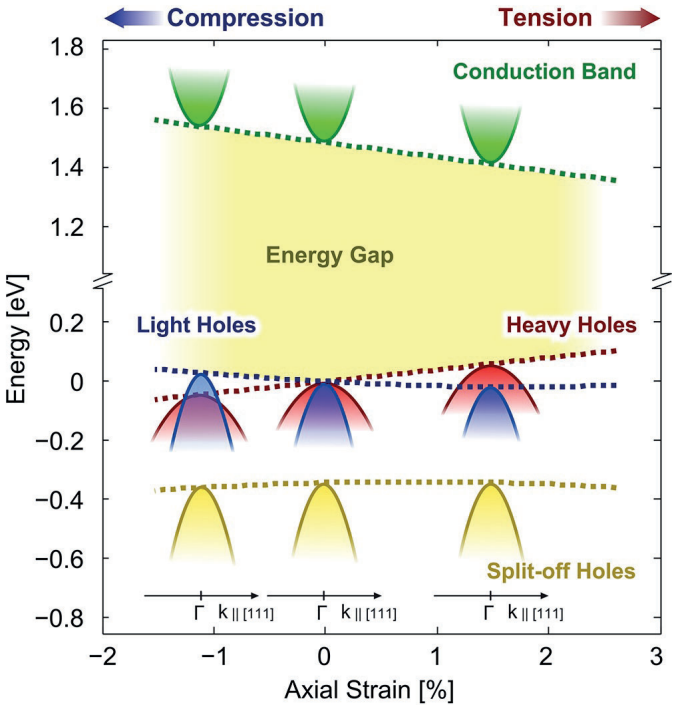

Figure 4.2: Simulation of the band structure of GaAs as a function of strain. The strain causes a splitting of the heavy- and light hole bands. Tensile strain reduces the band gap significantly. The relatively small increase in band gap with compressive strain is due to similar shifts in the conduction band and the light hole band. Reprinted with permission from Nano Lett. 2013, 13, 3, 917–924. Copyright 2013 American Chemical Society

4.2 ESE of III-V semiconductor nanowires

Semiconductor nanowires are suitable for ESE. Their high level of crystallinity and quasi-1D geometry make them able to withstand extreme levels of elastic strain. Si nanowires have been strained to 16 % experimentally, which is close to the ideal elastic limit [19]. In III-V nanowires, elastic strain of about 3-4 % have been reached, which is high enough to induce large modification of band structure and other properties. There are generally two different ways of applying strain, through internal stress or external stress. Internal stress is commonly induced by growing interfaces of materials with different lattice parameters. The lattice mismatch then give rise to strain. Nanowires can be grown in a core-shell structure, with a lattice mismatch between the core and the shell. In this way, large strain can be induced in the whole nanowire core [133]. This way is suitable in devices but the strain can not be altered after the structure is made. External strain is induced by applying an external force to the sample, often mechanically. In this way the strain can be continously altered back and forth. Figure 4.3 shows two common ways of introducing external strain in nanowires. In Figure 4.3 (a), a flexible steel substrate is bent to extend the gap between two metal clamps that hold the nanowire. In this way, high levels of uni-

axial tensile and compressive elastic strain can be applied to the nanowire [20][134]. Another common way is to mount the nanowire on a microelectromechanical system (MEMS) chip, see Figure 4.3 (b). This is usually the way to introduce strain in nanowires during in situ TEM measurements [135, 136]. In paper II, we use this method combined with scanning TEM-nanobeam electron diffraction to map the local strain distribution of GaAs nanowires. A third way of introducing external strain in nanowires is to use an AFM-tip, STM-probe or a nanomanipulator to push, bend or stretch the nanowire [137, 138]. In paper III, we use an in situ STM-FIBSEM setup to apply uniaxial tensile strain to individual vertical GaAs nanowires directly on the growth substrate.

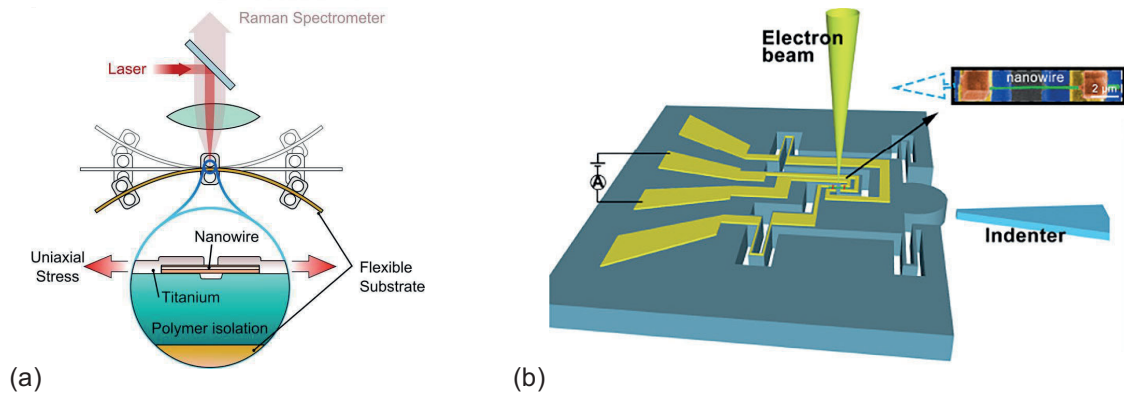

Figure 4.3: **(a)** Straining setup based on bending of a flexible substrate. Reprinted with permission from Nano Lett. 2013, 13, 3, 917–924. Copyright 2013 American Chemical Society. **(b)** MEMS-based straining of nanowire. Reprinted from Nano Lett. 2018, 18, 8, 4949–4956.

Extensive research has been carried out to investigate the impact of strain on III-V nanowires. For example, uniaxial strain has been shown to alter the electron transport properties and the energy of surface states in InAs nanowires, resulting in resistivity changes of several orders of magnitude [134, 136]. Moreover, strain induced by bending have been shown to affect the effective mass of valence electrons in GaAs nanowires [138]. There are many reports on strain-induced band gap modifications in GaAs nanowires. For example, mechanically induced uniaxial tensile strain in ZB GaAs nanowires has been shown to reduce the band gap energy with up to 296 meV [20]. Furthermore, strain induced by highly lattice mismatched core-shell structures in GaAs nanowires could reduce the band gap by 40% [133].

Many of these effects could potentially be utilized in nanowire solar cells. For example, the ability to tune the band gap energy can be very advantageous since it dictates which photons that can get absorbed and how much of their energies that gets used. Despite this, reports of strain engineering applied to nanowire solar cells are scarce. Compressive strain has been shown to increase the photovoltaic efficiency of single Cu_2S/CdS nanowires by the piezo-phototronic effect [139]. Likewise, the same effect has been utilized in ZnO nanowire arrays to enhance the performance of Si-based solar cells [140]. Furthermore, a theoretical study has shown that com-

pressive strain may increase the efficiency of GaAs nanowires containing both ZB and WZ segments [141]. In paper III, we study the effect of mechanical strain on the electrical and photovoltaic properties of single GaAs nanowire solar cells.

4.3 ESE of 2D TMDCs

The 2D geometry and in-plane covalent bonds of mono- to few layer TMDCs make them able to withstand high levels of elastic strain, thus making them suitable for ESE. According to theoretical predictions and experimental studies, atomically thin TMDCs are able to withstand elastic strain levels >10%, giving plenty of room for tuning of their physical properties [21, 142, 143]. For example, biaxial strain in monolayer MoS_2 is expected to continuously shift the band gap from 1.72 eV at no strain to 0 eV at 10% strain, giving rise to a semiconductor-to-metal transition [144]. Realization and investigation of these high elastic strains and their impact on properties demands reliable and versatile experimental straining and characterization techniques. Figure 4.4 shows some of the most common ways to strain 2D materials. AFM-indentation has been widely used to induce high, inhomogenous strain in various TMDCs [145–147]. For example, a maximum strain of around 19% was induced in WS_2 and WSe_2 monolayers using this technique [143]. Inhomogenous local strain may also be realized in so called bulge- or blister tests, where

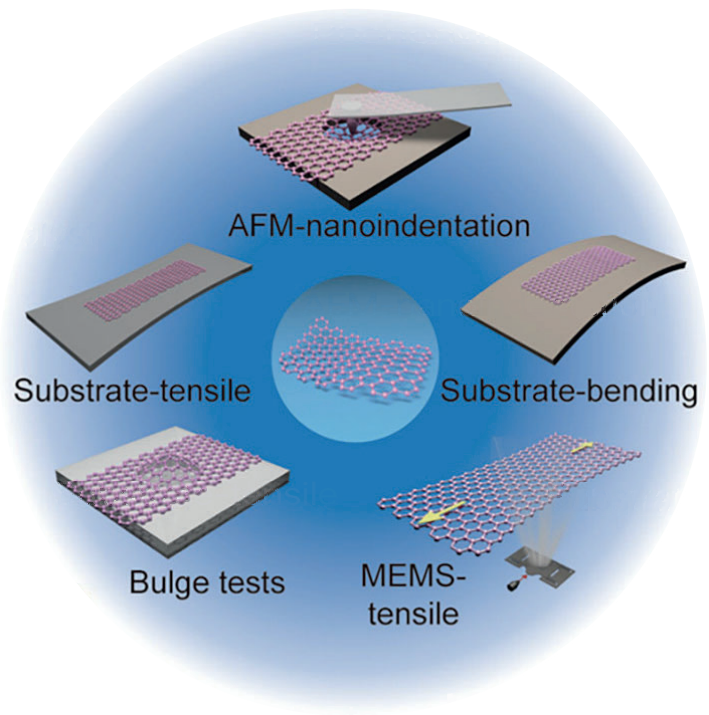

Figure 4.4: Illustration of common ways to introduce strain in 2D-materials. Adapted with permission from ACS Appl. Mater. Interfaces 2022, 14, 7, 8655–8663. Copyright 2022 American Chemical Society

pressure-induced bubbles are formed in the 2D material [148]. Controlled wrinkling is another way to induce inhomogenous strain in 2D TMDCs [149]. For large area, homogenous strains, flexible substrates offer a simple approach where bending or tension/compression of the substrate will induce strain in any 2D-material placed on the substrate surface. This technique is usually limited to strain levels $< 2\%$ though, due to the weak load transfer compared to the in-plane 2D-flake stiffness [150]. MEMS-devices have been shown to be able to introduce large area, homogenous strains of $> 5\%$ in Graphene and h-BN, and is a promising technique for ESE of TMDCs [151]. The main challenges with this technique is the transfer of 2D-flakes to the active area of the device, concentration of stress at the clamping of the flakes and edge defects caused by FIB-milling when shaping the suspended region, which may cause premature failure during straining [150].

Vast efforts have been made to experimentally study the effect of strain on the properties of TMDCs [151–153]. Only a few examples are mentioned here. A strain-induced band gap shift of 70 meV/% for uniaxial tensile strain in MoS_2 has been observed [154]. Biaxial strain of $\sim$5% has been shown to shift the band gap of MoS_2 by 500 meV [155]. A direct-to-indirect band gap transition due to strain has been observed in WS_2, MoS_2 and WSe_2 [156]. Furthermore, a reduction in the resistivity of MoS_2 due to strain has been observed [146]. Despite the efforts and progress made in this field, the great potential of ESE to bring novel electronic and optoelectronic properties in 2D TMDCs is still largely unexplored. Many theoretical predictions have not been experimentally verified, and a comprehensive understanding of the effect of strain in 2D materials is still lacking [150].

5. Metal-semiconductor contact

High quality metal-semiconductor contacts are essential for semiconductor technology. All semiconductor devices generally need to be connected to a metal-based electrical circuit, either for power supply, signal processing or energy harvesting. However, at a metal-semiconductor interface, a Schottky barrier is often formed due to the band gap of the semiconductor. This potential barrier affects the flow of charge carriers between the metal and the semiconductor, and may be detrimental for the device performance. Figure 5.1 describes the formation of a Schottky barrier between a metal and an n-doped semiconductor. When the metal and the semiconductor are isolated from each other (5.1 a), their Fermi levels are not aligned if the work function of the metal (ϕ_m) is different from the work function of the semiconductor (ϕ_s). As the metal and the semiconductor are brought into contact, electrons will flow from the semiconductor to the metal until the Fermi levels are aligned. This will form a depletion region in the semiconductor where uncompensated donor ions give rise to a positive charge, which is balanced by an excess of conduction electrons in the metal. This will induce a built-in electric field, and a bending of the bands in the semiconductor, as shown in Figure (b). The Schottky barrier height in this ideal case is then given by

$$\phi_b = \phi_m - \chi_s, \tag{5.1}$$

where χ_s is the electron affinity of the semiconductor [42].

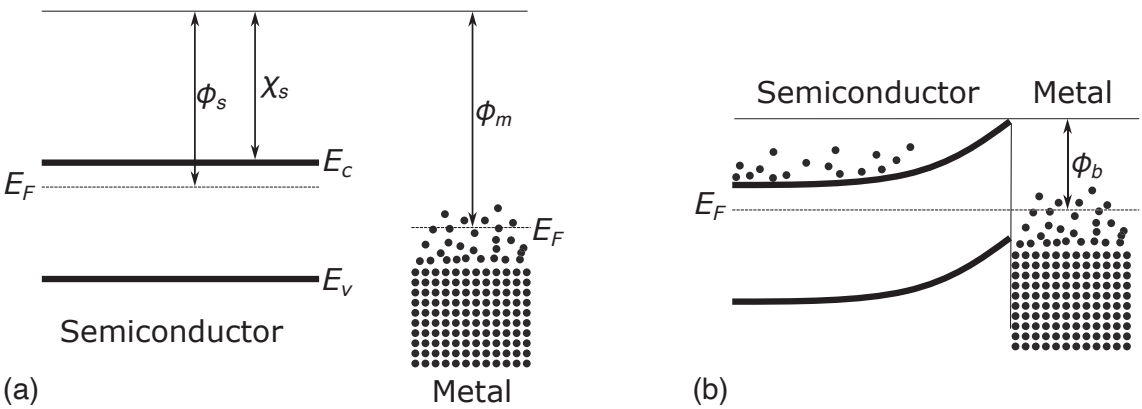

Figure 5.1: **(a)** Band diagram of a semiconductor and a metal separated from each other. **(b)** Band diagram as the semiconductor and the metal are brought into contact.

5.1 Ohmic contact

Ohmic contacts have linear I-V characteristics and are desirable for many applications, since they do not affect the overall I-V characteristics of the device. In principle, an Ohmic metal-semiconductor contact may be achieved by choosing a metal so that ($\phi_m < \phi_s$) for an n-doped semiconductor. However, for covalently bonded semiconductors that have dangling bonds at the surface (including most III-V semiconductors), the Fermi level of the metal tends to align to a characteristic energy position, ϕ_0, within the band gap of the semiconductor [157]. This so called Fermi level pinning makes the Schottky barrier height largely independent of ϕ_m, and instead of equation 5.1, the barrier height is given by $\phi_b \approx E_g - \phi_0$ [158]. Due to this Fermi level pinning, the most common way to achieve Ohmic metal-semiconductor contacts is to create a high doping concentration in the semiconductor locally at the contact. This is typically done by deposition of several layers of suitable metals and dopants (Pd/Ge/Au for n-doped GaAs), followed by an annealing process where the dopant diffuses into the semiconductor [159][93]. In this way, the barrier becomes so narrow that electrons may easily tunnel through, and high currents may flow in both directions.

5.2 Schottky contact

As opposed to an Ohmic contact, a Schottky contact is current rectifying and has non-linear I-V characteristics. A Schottky contact is usually formed if the semiconductor has low doping and the Fermi level of the metal is within the band gap of the

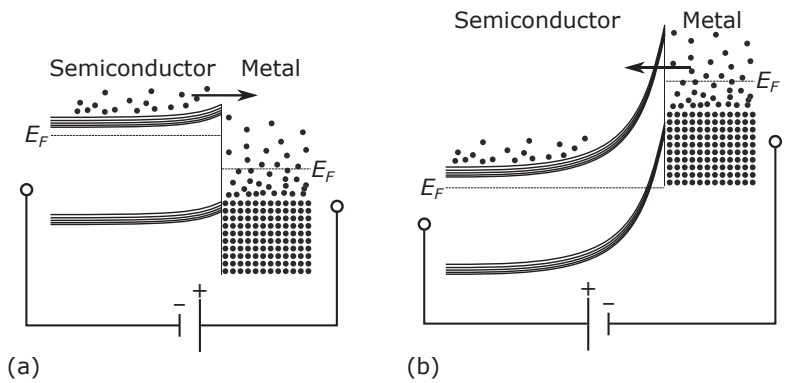

Figure 5.2: Band diagram of a Schottky contact during forward and reverse bias. **(a)** Forward bias state. The energy barrier is lowered by the applied bias, and thermally excited electrons from the semiconductor can go over the barrier. This process is called thermionic emission. **(b)** Reversed bias state. The energy barrier is increased by the applied voltage and the thermally excited electrons can no longer go over the barrier, but could tunnel through the barrier. This is the so called thermionic field emission process.

semiconductor, see Figure 5.1. Under forward bias conditions, i.e when an external bias is applied with the positive pole connected to the metal, the barrier is lowered and thermally excited electrons in the semiconductor can go over the barrier into the metal, as in Figure 5.2 (a). This is called thermionic emission (TE) [160] and is described by

$$I = SA^*T^2\exp\Big(-\frac{\phi_b}{k_BT}\Big)\exp\Big(\frac{qV}{nk_BT}\Big) \times \Big\{1 - \exp\Big(-\frac{qV}{k_BT}\Big)\Big\}, \tag{5.2}$$

where I is the current, S the area of the contact, A^* is the Richardson constant, T the temperature, ϕ_b is the barrier height, k_B is Boltzmann's constant, q is the elementary charge, n the ideality factor and V is the applied bias. Under reverse bias conditions, however, the barrier height will increase and the electrons cannot go over the barrier, see Figure 5.2 (a). This results in a current rectifying behaviour of the contact if only thermionic emission is considered, see Figure 5.3.

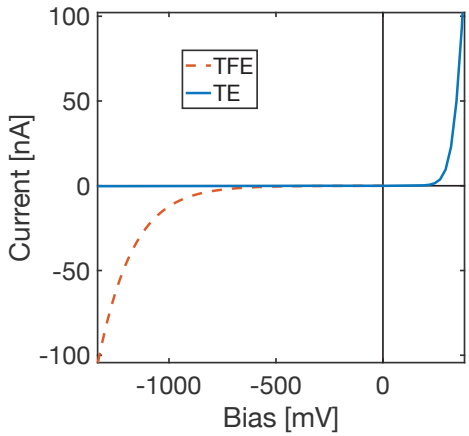

Figure 5.3: Modeled I-V characteristics of a Schottky diode using TE and TFE, respectively.

However, in many cases there is a significant current flowing even in the reverse bias state, especially in nanoscale applications [161]. The reason for this is that there is a possibility for the thermally excited electrons to tunnel through the barrier, see Figure 5.2 (b). This phenomena is described by thermionic field emission (TFE) theory [162], which states that the current through a Schottky barrier is given by

$$I = I_{sb}(V, \phi_b) \times \exp\Big\{V\Big(\frac{q}{k_BT} - \frac{1}{E_0}\Big)\Big\} \tag{5.3}$$

where the saturation current I_{sb} can be expressed as

$$I_{sb} = \frac{SA^*T(\pi qE_{00})^{1/2}}{k_B}\exp\Big(-\frac{\phi_b}{qE_0}\Big) \times \Big\{q(V-\xi) + \frac{\phi_B}{\cosh^2(qE_{00}/k_BT)}\Big\}^{1/2}. \tag{5.4}$$

Here ξ is difference in energy between the Fermi level and the bottom of the conduction band. E_0 can be expressed as

$$E_0 = E_{00}\coth\left(\frac{qE_{00}}{k_B T}\right) \tag{5.5}$$

and

$$E_{00} = \frac{\hbar}{2}\left(\frac{N_d}{m_n^* \epsilon}\right)^{1/2} \tag{5.6}$$

whith N_d being the doping concentration, m_n^* the effective electron mass and ϵ is the permittivity. In Figure 5.3 it is evident that the TFE model gives a significantly larger current during reverse bias than the TE model.

5.2.1 Surface defects and insulating layer

In practice, a thin insulating layer is often present between the metal and the semiconductor. For example, if III-V semiconductors are exposed to air, they usually get covered with a thin native oxide layer. If this oxide layer is not removed before contacting, it increases the distance between the semiconductor and the metal, which reduces the probability of tunneling, see Figure 5.4 (a). The effect of an insulating layer with a thickness δ and a mean barrier height χ may be taken into account in the model by incorporation of an effective Richardson's constant A^{**}defined as [161],

$$A^{**} = A^* \exp(-\chi^{1/2})\delta. \tag{5.7}$$

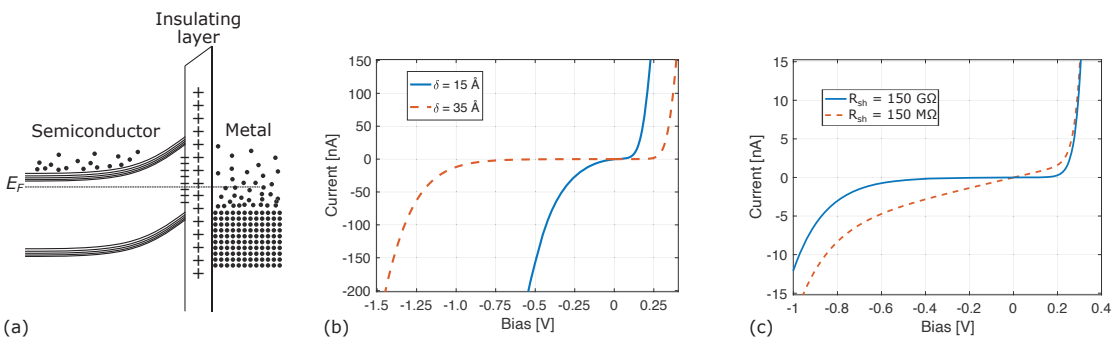

Figure 5.4: **(a)** Band diagram of a Schottky contact with a thin insulating layer present between the semiconductor and the metal. **(b)** I-V characteristics of a Schottky contact with a thin insulating layer of thickness 15 Å and 35 Å, respectively. **(c)** I-V characteristics of a Schottky contact with an R_{sh} of 150 GΩ and 150 MΩ, respectively.

In Figure 5.4 (b) it can be seen that the thickness of the insulating layer affects the current significantly. There may also be localized electronic states at the semiconductor surface, and trapped charges in the insulating layer, see Figure 5.4 (a). This may introduce an alternative current path, which can be considered as a shunt resistance, R_{sh}, in parallel with the Schottky barrier. A high number of charges at the interface results in a low value of R_{sh}, and leads to linear I-V characteristics at small biases [163], see Figure 5.4 (c).

5.2.2 Combination of a p-n junction and Schottky barrier

High quality, Ohmic contacts are crucial for efficient solar cells. If a rectifying Schottky barrier is formed at the contact, this may have detrimental effects on the photovoltaic performance [164]. Figure 5.5 shows an example of simulated dark and illuminated I-V characteristics of a p-n junction with Ohmic contact and a p-n junction with a Schottky contact. The dark current is significantly reduced by the Schottky barrier. The illuminated I-V curve is affected even more. Instead of being a superposition of the dark I-V curve, it has an S-shape around zero bias, reducing the maximum power output of the solar cell. This rather peculiar feature is qualitatively explained by the band diagrams shown in Figure 5.5 (b) and (c). If the p-n junction is combined with a Schottky contact on the n-side, there will be two slopes in the bands with opposite direction. When the p-n junction is reversely biased [Figure 5.5 (b)], the Schottky barrier is forwardly biased and the barrier height at the contact is lowered, letting through the photogenerated charge carriers. However, when the p-n junction is forwardly biased [Figure 5.5 (c)], the height of the Schottky barrier increases as it is reversely biased. The photogenerated charge carriers are blocked by the barrier, and the photocurrent is significantly reduced.

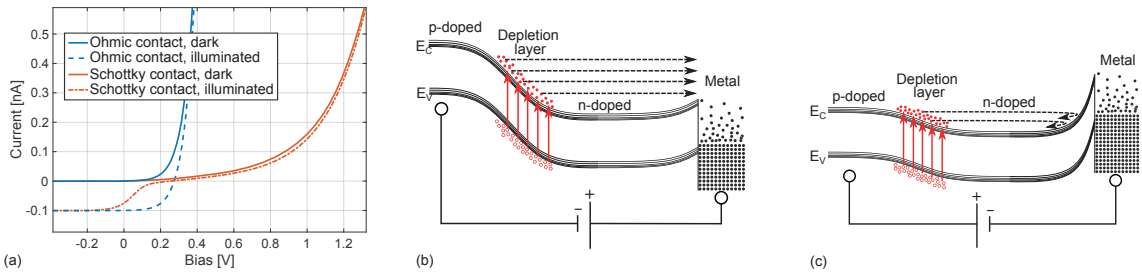

Figure 5.5: **(a)** Modeled I-V characteristics of a P-N junction with Ohmic contact and a Schottky contact, in dark and illuminated condition, respectively. The rectifying behavior of the Schottky barrier reduces the forward current and introduces a kink in the illuminated I-V curve. **(b)** Band diagram of a reversely biased, illuminated p-n junction in series with a Schottky barrier. The Schottky barrier height is reduced by the applied bias and the photogenerated charge carriers can pass over the barrier into the metal. **(c)** Forwardly biased, illuminated p-n junction in series with a Schottky barrier. The Schottky barrier height is increased by the applied bias and the photogenerated charge carriers are blocked by the Schottky barrier.

6. Experimental techniques, methods and materials

This chapter provides a general introduction to the experimental techniques and methods that were used in this thesis work. It also provides detailed information about the specific materials and specimens that were investigated.

6.1 Scanning electron microscopy (SEM)

In scanning electron microscopy (SEM), a focused electron beam is scanned across a specimen to produce an image of the specimen surface. The general design of a scanning electron microscope (SEM) is shown schematically in Figure 6.1. An electron gun is located at the top of the instrument where electrons are emitted and accelerated downwards by an electric potential in the order of 1-30 keV. An electrostatic gun lens gathers the electrons into a crossover-point, and this crossover is subsequently de-magnified by a set of electromagnetic lenses located further down a cylindrical space commonly known as the "column" of the microscope. Unlike glass lenses, the focal length of an electromagnetic lens can easily be altered by changing the current running through its coil. In this way, the de-magnification of the crossover and the lateral point where the beam is in focus can be changed simply by turning a knob changing the coil current. As the electrons travel down the column they also pass through a number of apertures with variable sizes that limits the convergence angle and the electrical current of the beam. The column also contains a pair of so called scanning coils. Their task is to deflect the beam so that it is scanned over a certain area of the specimen. The objective lens, located at the bottom of the column, is used to focus the beam on the surface of the specimen, which generally is located around 2-50 mm below the polepiece of the objective lens. Once the electron beam hits the sample, various signals are generated due to interactions between the beam electrons and the sample. These signals carry different information and can be used to form an image of the specimen, but also for spectroscopy determining elemental composition, diffraction for crystallographic characterization etc. [165].

6.1.1 Imaging

In the image formation process, the beam is scanned over an area of the specimen in an x-y pattern. The beam stops for a certain amount of time, typically in the µs range, at a discrete set of points on the specimen. Simultaneously, an image is built up on a computer display where the pixels have a one-to-one correspondence to the beam locations on the specimen. The brightness of each pixel is determined by the strength of the signal that is chosen to be collected. Most SEM images generated in this way tend to be surprisingly intuitive to interpret. However, a basic knowledge of the signal generation and detection, image formation and contrast mechanisms helps to correctly interpret the fine details.

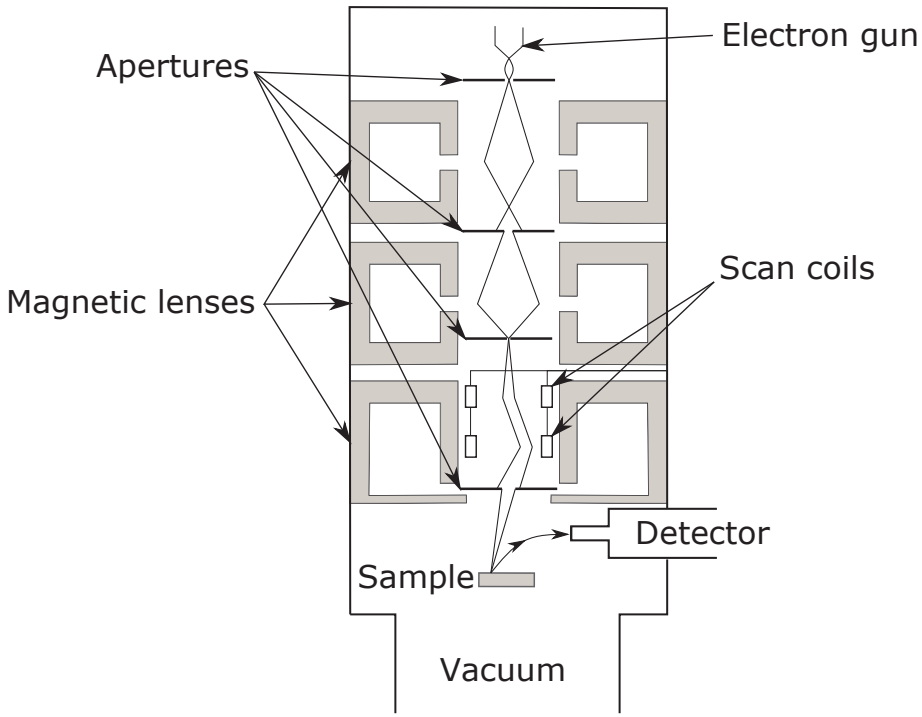

Figure 6.1: Schematic structure of an SEM. An electron gun produces an electron beam that is accelerated down through the column by an electric field. An electrostatic gun lens forms the first cross-over. A set of apertures and electromagnetic lenses are used to further de-magnify the beam diameter, and a set of scan coils are used to scan the beam across the sample. Various signals are generated from the beam-sample interaction and detected to form an image or provide other information of the sample.

The two main signals used for image formation are so-called backscattered electrons (BSEs) and secondary electrons (SEs). BSEs are primary electrons (electrons from the beam) that, after interaction with the sample, are scattered back more or less in the opposite direction of the beam. It is due to both elastic and inelastic collisions with the atomic nuclei in the sample that the electrons changes their traveling direction. When these BSEs leave the sample their kinetic energies range from

almost zero up to the energy of the incoming electrons (1-30 keV). A consequence of the collisions is that the beam broadens on its way through the specimen. The corresponding volume is called the beam interaction volume, see Figure 6.2 (a). The size of the interaction volume depends on the acceleration voltage, with high voltage leading to a large volume and vice versa. The imaging resolution of the BSE signal is limited by the size of the interaction volume. The probability for the primary electrons to collide depends on the atomic number, Z, of the elements in the sample. Heavy elements generate a stronger BSE signal than lighter elements, and this phenomenon is the basis for a contrast mechanism called elemental contrast or Z-contrast. Furthermore, the BSE signal has a significant directionality, and tends to be strong along the direction of the specimen normal. This may give rise to topographic contrast [166].

SEs are electrons that are knocked out from the sample atoms due to inelastic collisions of the primary electrons. The SEs are generated throughout the whole interaction volume. However, SEs have small kinetic energies, $E_k < 50$ eV, and therefore short mean free paths in the sample. Thus it is only those that are generated close to the surface that can escape the sample and give rise to a detectable signal [165]. The imaging resolution of the SE signal can therefore be close to the beam diameter, and for high quality SEMs a resolution of less than 1 nm can be reached [167]. As the tilt angle of the surface of the sample increases, the effective volume that lies within the escape range for the SE increases. Thus, highly tilted surfaces give rise to a strong SE signal. Edges, corners and small structures such

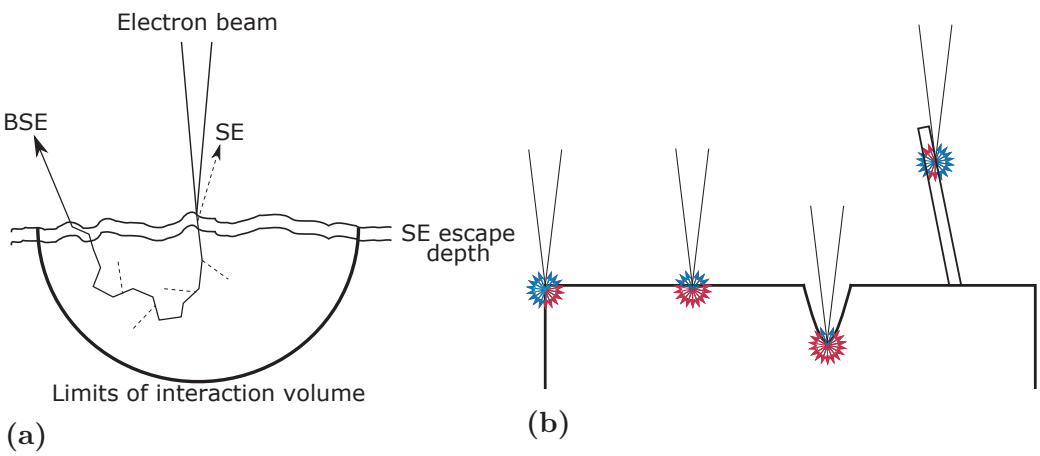

Figure 6.2: **(a)**: Qualitative illustration of the beam interaction volume in an SEM. Once the beam hits the sample it is broadened due to the interaction between the electrons and the atoms in the sample. This reduces the resolution of the BSE signal. SEs are also generated in the whole interaction volume, however, since it is only those SEs that are generated close to the surface that escape and get detected, the SE signal can have almost the same resolution as the beam diameter. **(b)**: Topographic contrast mechanism for SE. The blue arrows represent SE that can escape from the sample, and red arrows represent SE that stays in the sample. As can be seen, highly tilted surfaces, edges and corners result in high SE signal while flat surfaces and valleys result in low SE signal.

as nanoparticles or nanowires also have a large effective volume within the escape range. A strong SE signal can therefore be expected at such positions, see Figure 6.2 (b). On the other hand, flat surfaces and valleys have small effective volumes within the escape range, resulting in a weak SE signal. This phenomenon gives rise to a topographic contrast, and the SE signal is therefore well suited to reveal the topography of the sample, with high spatial resolution.

Once the SEs and BSEs have escaped the sample, they need to be detected in order to make use of the signals. The most common detector is the so-called Everhart-Thornley (ET) detector. It is usually placed above the sample, see Figure 6.3a. Both BSEs and SEs can be detected by the ET detector. If a negative bias >50 V is applied to the detector, all the SEs will be deflected and only the highly energetic BSEs with trajectories pointing towards the detector will contribute to the measured signal. The resulting image will therefore have Z-contrast (heavy elements will appear brighter than light elements), but also some topographic contrast were the surfaces tilted towards the detector will appear brighter than surfaces tilted away from the detector. For normal imaging though, the ET detector is usually positively biased, with a potential of around 250 V. As a result, the low energy SEs are drawn into the detector, regardless of the direction of their original trajectories, see Figure 6.3a. The BSEs will still be detected, and the measured signal will be a mixture of both BSEs and SEs. Because of this additional SE signal, the image will gain extra topographic contrast. Any tilted surface, edge, corner, peak or nanoparticle will appear bright, whether its facing the detector or not. In order to understand or imagine how the final image will look like, there is an analogy that can be made between the situation in the microscope and an everyday life situation, see Figure 6.3b. The image will appear as though the the viewer were looking down on the sample along the direction of the beam, and the sample was both illuminated

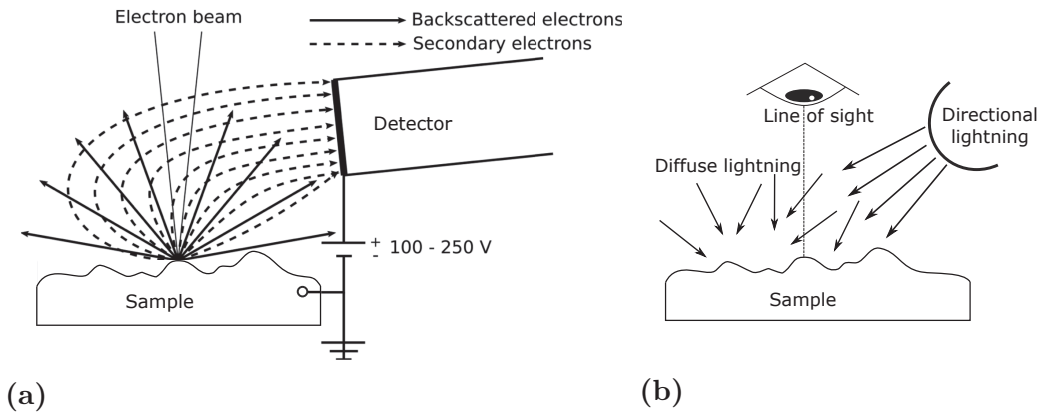

Figure 6.3: **(a)** Detection of BSE and SE with an ET detector. By applying a positive bias to the detector, the low-energetic SE will be drawn into the detector while the high-energetic BSE will be unaffected.**(b)** Real-life analogy of SEM images generated with a positively biased ET-detector. The images will appear as if the viewer is located at the beam source and the sample is illuminated with a directional light source (BSE signal) located at the position of the detector, and an additional diffuse lighting source (SE signal).

by diffuse light and a highly directional light source located at the detector. The directional light source represents the BSE signal and the diffuse lighting represents the SE signal. This is what we are used to since the sun is a directional light source and the scattered light from clouds and objects provides diffuse illumination of our environment, which is why SEM images generated in this way are so easy to interpret [165]. However, there are other ways of forming images, using other types of detectors and signals, which may be more difficult to interpret. In this thesis though, all the SEM images were generated in the way described above, with a mixture of SE and BSE signals.

6.1.2 Electron beam induced current (EBIC)

Electron beam induced current (EBIC) is a technique that is used to map the electronic activity of a sample [168]. When the electron beam is scanned across a semiconductor sample, electron - hole pairs will be created, just as when the sample is illuminated by photons. One important difference though is that the electron beam is localized to a spot size of a few nanometers. If, for example, a p-n junction is present, the electron-hole pairs will be separated and generate a current. Since the beam-electrons in an SEM generally have energies in the range $0.1 - 30$ keV, and typical semiconductor band gap energies are ~ 1 eV, each beam-electron can potentially generate thousands of electron-hole pairs. The measured current will therefore depend on the beam-current, but with a large amplification. By plotting the measured current over the analyzed area pixel by pixel, an EBIC map will be created. If the amount of generated electron-hole pairs is the same in each pixel, the EBIC signal will represent the fraction that are separated and contribute to the current before recombining. Parameters that may influence this are the quality of the p-n junction, the electron and hole diffusion length and distance to reach the junction, and the crystalline quality of the sample (defects act as recombination centers).

The amount of generated electron-hole pairs is largely dependent on the interaction volume of the beam electrons, and the topography of the sample. If the beam is placed close to the edge of the sample, so that part of the interaction volume is outside the sample, it means that some of the beam-electrons will escape before transferring all their energy to the sample. Fewer electron-hole pairs will therefore be created. Figure 6.4 shows Monte Carlo simulations of the interaction volume in a GaAs nanowire at a few different beam acceleration voltages. At 1 keV (6.4a), the electron beam only penetrates ∼30-40 nm into the sample. Thus electron-hole pairs are only generated close to the surface. At 10 keV, (6.4b), the beam spreads throughout the whole nanowire cross-section. At 30 keV, the beam is more narrow than at 10 keV because most of the electrons escape through the lower surface of the sample without much interaction. If the sample had been thick (> 5 µm), the 30 keV beam would have broadened much more than the 10 keV beam [165].

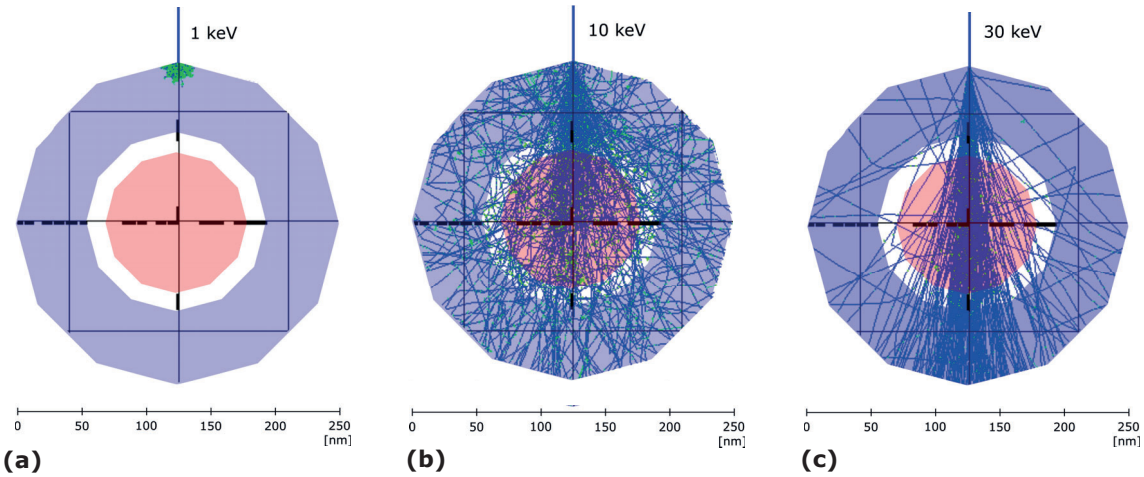

Figure 6.4: Beam interaction volume simulated using Monte Carlo model at beam acceleration voltage **(a)** 1 keV **(b)** 10 keV and **(c)** 30 keV

6.2 Transmission electron microscopy (TEM)

In a transmission electron microscope (TEM), an electron beam is transmitted through, and detected below, the specimen. The sample needs to be thin, usually around 100 nm, in order for the electrons to be transmitted without too much interaction with the specimen. The resolution of a TEM is ∼1-10 Å, which means that the atomic structure of the sample can be investigated. The basic principle of a TEM is depicted in Figure 6.5 (a). An electron gun generates a current of electrons that are accelerated by an electric field of 50-300 keV. The electron beam then passes through the illumination system, which consists of an electrostatic gun lens and a number of condenser lenses and apertures. As in an SEM, the electromagnetic lenses create a strong, adjustable magnetic field that affects the trajectories of the electrons. The apertures are discs with holes where the central part of the beam can pass through but the rest of the beam is blocked. The condenser lenses form either a parallel or convergent beam that illuminates the sample. For traditional TEM imaging and diffraction, a parallel beam is used. After the beam has passed through the specimen it enters the imaging system, also consisting of lenses and apertures. Their role is to magnify and project either an image or a diffraction pattern of the specimen onto a florescent screen or a charge-coupled device (CCD) camera [169]. Please note that Figure 6.5 (a) is a simplified version of an actual TEM, which generally has more lenses, apertures and components.

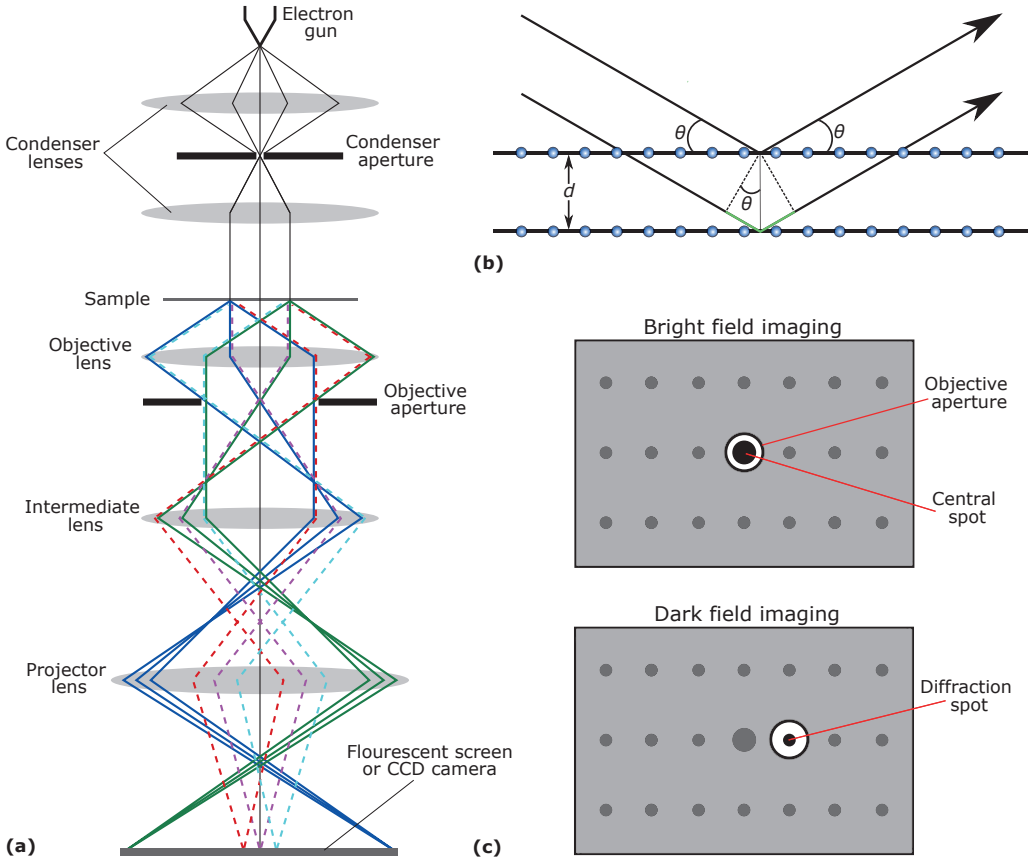

Figure 6.5: **(a)** Simplified schematic of a TEM. An electron gun emits electrons that are accelerated by an electric field. Condenser lenses and apertures are used to form a parallel beam that illuminates the sample. The electrons are scattered into different angles by the interaction with the sample. In imaging mode, electrons that emerge from one point on the sample (solid lines of same color) are gathered into one point on the screen or CCD camera by a set of lenses. In diffraction mode, it is instead electrons that are diffracted into the same angle (dashed lines of same color) that are gathered into one point. To toggle between the two modes, it is sufficient to change the strength of the intermediate lens. **(b)** Graphical description of Bragg's law. The incoming electron rays are reflected at the atomic planes. If θ is such that the extra distance the lower ray need to travel (green segment) equals an integer number of wavelengths, constructive interference occur and diffraction is obtained at that angle. **(c)** Principal behind BF and DF imaging. For BF the objective aperture is placed so that the central spot can pass through, while for DF one or more diffracted spots are chosen to pass through.

6.2.1 Diffraction

When the electrons are transmitted through a sample, they are scattered because of interaction with the atoms in the specimen. If the sample is crystalline, the atoms are ordered in a lattice with a certain periodicity. This results in certain preferred scattering angles of the electrons, a phenomenon called diffraction. The simplest way

to describe diffraction is through Bragg's law. In this picture, the atomic planes are regarded as mirror planes where the incoming electrons get reflected, see Figure 6.5 (b). In order for constructive interference to occur, the difference in traveled distance for electrons reflected at different atomic planes has to be an integer multiple, n, of the wavelength of the electrons. The angles θ that fulfill this requirement can be found using the Bragg equation:

$$2d \sin \theta_B = n\lambda. \tag{6.1}$$

Here θ_B is the Bragg angle, d is the distance between two adjacent atomic planes and λ is the wavelength of the incoming electrons. In a TEM, the kinetic energy of the electrons is known and controlled by the acceleration voltage, thus λ can be calculated, and θ can be measured. Diffraction can therefore be used to investigate the spacing between atomic planes of crystalline samples. In fact, it is possible to find the complete crystal structure of the specimen by analysing so called diffraction patterns. The dashed lines in Figure 6.5 (a) shows how such a diffraction pattern is collected in a TEM. Basically, all the electrons that are diffracted along a certain angle are focused into a spot in the back focal plane of the objective lens. This plane is then chosen as the object plane of the projection lens, by adjusting the strength of the intermediate lens, and projected onto the viewing screen or the CCD camera. Each spot corresponds to one set of parallel atomic planes in the sample, except for the central spot which corresponds to electrons that have transmitted through the sample without being scattered. The distance between a diffraction spot and the central spot is reversely proportional to the distance between the atomic planes corresponding to that diffraction spot. The symmetry of the diffraction pattern is related to the symmetry of the crystal structure of the specimen. In fact, the diffraction pattern represents a section through the reciprocal lattice of the specimen [169].

6.2.2 Imaging

In a TEM, an image is produced by focusing all the electrons scattered from one point in the sample to one point at the viewing screen or CCD camera. This is done by adjusting the strength of the intermediate lens so that the image plane of the objective lens becomes the object of the projector lens, see the solid lines in Figure 6.5 (a). There are two different modes of imaging typically used in a TEM, bright field (BF) and dark field (DF). It is the position of the objective aperture relative to the diffraction pattern that determines whether the resulting image is a BF or DF image, see Figure 6.5 (c). The objective aperture is located at the back focal plane of the objective lens, which is a conjugate plane of the diffraction pattern. This means that by varying the size and position of the objective aperture, one can choose which diffraction spots will be blocked and which ones that will pass through the aperture and contribute to the final image. If the central spot, corresponding to unscattered electrons, is chosen to pass through the aperture, the resulting image will be BF. Thin, low-mass areas of the specimen that do not scatter the electrons

so much will appear bright, while thicker, high-mass areas will appear dark in a BF image. If instead the central spot is blocked and only one or more of the diffracted beams are chosen to pass through the aperture, a DF image will be produced. Then areas that diffract electrons into the chosen spots will appear bright while other areas will appear dark. This is especially useful when the specimen contains regions with different crystal structure or orientation, such as polycrystalline or polytypic samples.

6.3 Focused ion beam - scanning electron microscope (FIB-SEM)

A focused ion beam (FIB)-SEM is a dual beam instrument with both an electron beam column and an ion beam column. The two columns are tilted with regards to each other, normally at an angle of $\sim 50°$, see Figure 6.6. The advantage of such an instrument is that the high-resolution imaging capability of the SEM is combined with the milling capability of the FIB. When the ions hit the sample, atoms located close to the sample surface will be sputtered away. In this way, the FIB can be used to remove unwanted material and mill structures in the sample with high precision, while the process is being monitored using the SEM image. Most FIBSEM:s also contain a gas injection system (GIS). A precursor gas is injected close to the sample surface, where the gas molecules are adsorbed. However, the molecules only decomposes where the electron or ion beam hits the sample. This

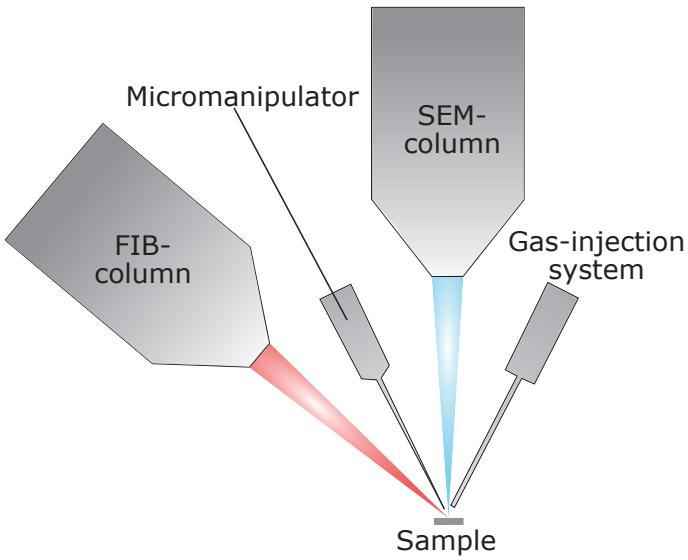

Figure 6.6: Schematic illustration of a FIBSEM. The instrument contains both an SEM-column and a FIB-column, tilted approximately 50° with respect to each other. The ion beam may be used to sputter material from the sample while the electron beam is used for imaging. A gas-injection system is included for deposition of material and the micromanipulator enables in situ lift-out of prepared specimens.

enables local material deposition, spatially controlled by either the electron or the ion beam. Both conductive and insulating materials can be deposited this way [170].

TEM-lamellae with thicknesses < 100 nm can be routinely prepared using FIBSEM. The area of interest is first covered by metal-deposition (usually Pt) using the GIS. Trenches are then milled on both sides of the area of interest, leaving a slice of ∼1-5 µm in the middle. The slice is then transferred to a TEM-grid by in situ lift-out, enabled by a micromanipulator inside the FIBSEM. The slice is attached to the micromanipulator, and subsequently to the grid, by metal-deposition. The ion beam is used to cut the slice loose from the sample and then from the micromanipulator. Once the slice sits securely on the grid, it is thinned down to the wanted thickness by the ion beam. An issue with this technique is that ions from the beam can get implanted in the sample and crystalline samples may undergo a transition to an amorphous phase close to the milled surface. These features can, to a certain degree, be limited by adjusting the acceleration voltage and current of the ion beam.

6.4 Raman spectroscopy

Raman spectroscopy is a versatile, non-destructive characterization technique that provides chemical and structural information about materials. The technique is based on the Raman effect, which is the phenomenon where light is inelastically scattered by interaction with molecular vibrations and phonons in matter. The scattering leads to a frequency shift, $\Delta\nu$, of the light, defined as $\Delta\nu = \nu_r - \nu_0$, where ν_r and ν_0 is the frequency of the scattered and the incident light, respectively. The set of frequency shifts that is obtained when a specimen is illuminated with a monochromatic light source constitutes the Raman spectrum of that specimen [171]. The Raman spectrum is usually expressed in wavenumbers, with units of inverse length (cm^{-1}) instead of frequency. In confocal Raman microscopy, an optical microscope is used both to image the sample and focus a laser spot on the surface of the sample. The scattered laser light is focused through an aperture into a detector to retrieve the Raman spectrum. The laser spot may also be scanned over an area in so called Raman mapping.

Raman spectroscopy can be used to determine both layer thickness and strain distribution in 2D TMDCs. In bulk MoS_2, the in-plane E^1_{2g} and the out-of-plane A_{1g} phonon modes are Raman-active, and give rise to Raman peaks at ∼383 rel. cm^{-1} and ∼408 rel. cm^{-1}, respectively. As the number of layer decreases, the peak positions shift, and for monolayer MoS_2, the E^1_{2g} peak is at 384 rel. cm^{-1} and the A_{1g} peak is at 402 rel. cm^{-1} [172]. This may be used to determine the layer thickness for samples that are 1-4 layers thick. Furthermore, if uniaxial tensile strain is applied to a 2D MoS_2 sample, this will cause a red-shift of the E^1_{2g} peak. It has been shown that the shift is approximately 1.7 cm^{-1} per % strain for few-layer MoS_2 [173], however this may vary depending on the direction of the strain in relation to the crystallographic orientation of the sample [174].

6.5 In situ scanning tunneling microscope (STM) setup

In a scanning tunneling microscope (STM), a sharp, conducting nanoprobe is scanned closely above the surface of a sample while the measured tunneling current is used to produce an image of the surface. For in situ STM-SEM however, the imaging is provided by the SEM, while the STM is used for electrical measurements of nanoscale objects. For the in situ measurements of this work, an STM merged together with a SEM sample holder was used, see Figure 6.7. The SEM-holder makes it possible to place the STM and the sample inside the vacuum chamber of an SEM or a FIBSEM. A light emitting diode (LED) is mounted on the holder to provide light illumination of the sample.

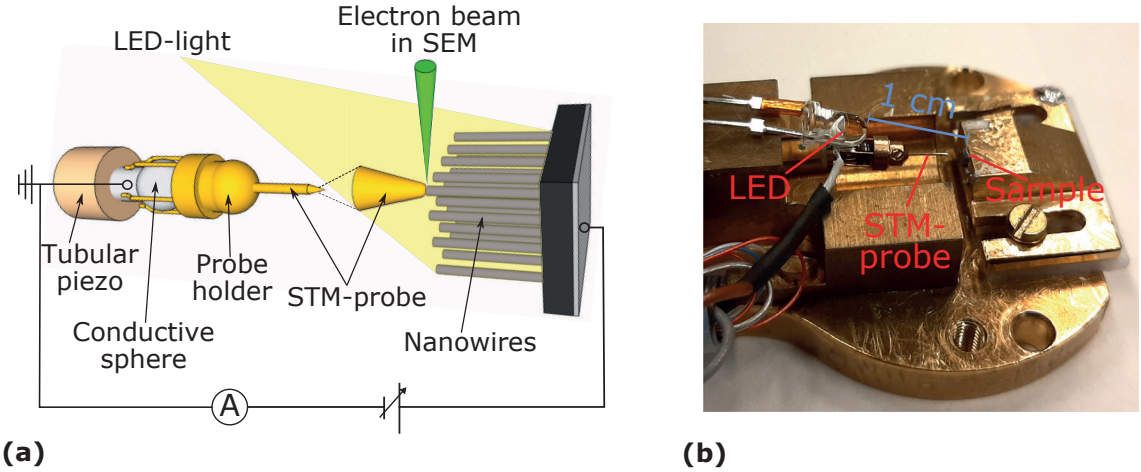

Figure 6.7: **(a)** Schematic illustration of the STM-SEM holder. **(b)** Photograph of the STM-SEM sample holder used for the experimental work. The LED is mounted above and behind the STM-probe, approximately 1 cm away from the sample.

The STM is composed of a tubular piezo that controls the 3-dimensional movement of a conductive sphere. A six-legged metal probe-holder is clamped to this metal sphere. The probe is attached to the probe-holder, and the sample is placed within reach of the tip of the probe. The sample and the probe are connected to an external electrical circuit containing a picoammeter and a power supply. By moving the probe into contact with a specific part of the sample, for example a nanowire, a closed electrical circuit can be formed and measurements may be performed. The movement of the STM probe has two different modes, coarse movement and fine movement. In the fine movement mode, the spatial resolution is $\sim$ 1 nm, but the range is limited to around 1 µm for backward/forward movement and around 10 µm for upward/downward and side movement. The coarse movement mode provides a range of several millimetres in all directions, but with a lower spatial resolution. The sharp tip of the STM-probe can be produced by cutting a 0.25 mm gold wire with a clean pair of scissors, simultaneously as the gold wire and scissors are being

pulled apart. This produces an uneven cut area which usually contains features sharp enough for contacting nano-scale samples.

6.6 Piezo-based straining device

A device based on a piezo-actuator was developed for straining of 2D-flakes. The design of the device is shown in Figure 6.8. Two metal supports are glued onto opposite sides of the piezo-actuator, Figure 6.8 (a). When a bias is applied to the piezo-actuator, it will expand or contract laterally, increasing or decreasing the distance between the two metal supports. A Si wafer with a SiO_2-layer and patterned metal electrodes on the top surface is glued on top of the supports. Before the gluing, a pre-crack is made on the bottom side of the Si wafer. After the glue has hardened, the Si wafer is cracked in two by pushing gently on the pre-crack with a diamond cutter tool. This results in a small gap in the middle of the Si wafer, where the width can be controlled by the bias applied to the piezo-actuator. Subsequently, a 2D-flake is transferred to the device using viscoelastic stamping [110], see section 3.1. The flake is placed over the gap so that one segment of the flake is freely suspended, see Figure 6.8 (b). It may also be placed on top of the electrodes for electrical measurements. The design of the piezo device was inspired by Ref. [175].

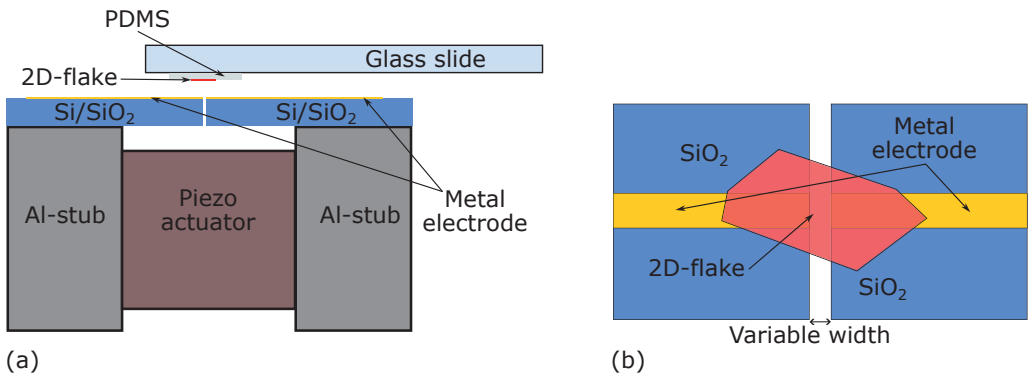

Figure 6.8: Principle and schematic design of the piezo-straining device. **(a)** Side-view of the device and transfer of 2D-flake. **(b)** Top-view of 2D-flake suspended over the gap of the device.

Figure 6.9 illustrates the functionality of the piezo-straining setup. One large and one small flake are suspended over the gap, marked by the red and the yellow arrows. When there is no bias applied to the piezo (Figure 6.9 a), the flakes are bent in the suspended region, indicated by the dark and bright stripes parallel to the gap. Directly after the stamping though, the flakes lay flat over the gap. The bending of the flakes is therefore most likely caused by small mechanical vibrations created when mounting the device under the optical microscope. There is also a ripple in the big flake, extending downwards from the gap. This ripple was present directly after the stamping. By applying some bias to the piezo, the width of the

gap increases and the suspended parts of the flakes are straightened (Figure 6.9 b). The homogeneous contrast in the suspended region of the big flake indicates that the flake is flat there. In the small flake, a weak ripple pattern can be discerned. As the gap is opened further, two different scenarios can occur, illustrated by the big and the small flake in Figure 6.9 (c) and (d). Either the suspended flake is strained until it fractures (big flake), or the flake glides on top of the substrate (small flake). Whether the flake glides or not depends on the size of the contact area to the substrate, the adhesion force between the flake and the substrate and the thickness of the flake. Gliding can be inhibited by anchoring the flake to the substrate, either by Pt-deposition or epoxy glue.

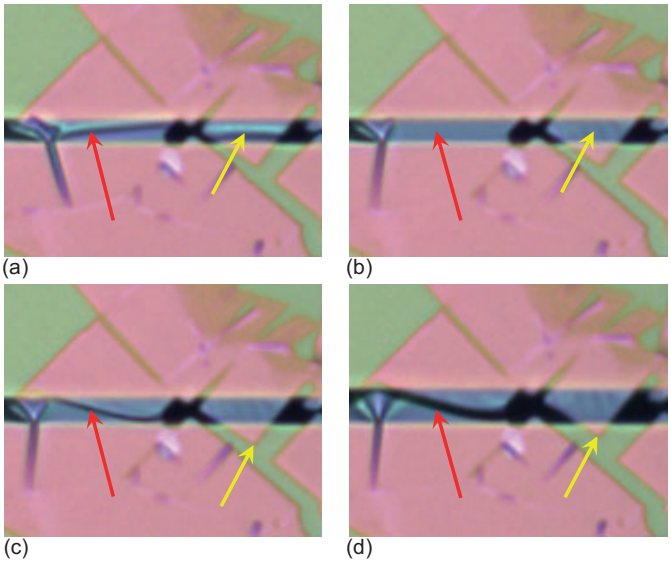

Figure 6.9: Optical microscope images showing straining of MoS_2-flakes using the custom-made piezo-device. **(a)** No bias applied to the piezo-actuator. One big flake (red arrow) and one small flake (yellow arrow) are suspended over the gap. The flakes are bent in the suspended region. **(b)** The gap is extended by applying a bias to the piezo-actuator. The suspended parts of the flakes are straightened. **(c)** The gap is further extended. The big flake fractures in the suspended region. The small flake glides on top of the substrate. **(d)** As the gap is further extended, the small flakes continues to glide.

6.7 GaAs nanowires

Two types of nanowires were investigated in this work, p-doped GaAs nanowires and radially doped p-i-n GaAs solar cell nanowires. They were fabricated through SC-MBE by P. Krogstrup et al. [13]. A p-doped (111) Si substrate was heated to 630 °C and a flux of Ga and As_4 was introduced into the chamber. The p-doping was achieved by introducing an additional flux of beryllium during the axial growth of the nanowires [176]. For the solar cell nanowires, the axial growth was followed by a change in growth parameters to promote radial growth. During the radial growth of

the wires, a thin intrinsic layer was formed, whereafter an n-doped shell was grown by adding a flux of Si [39]. The total diameter of the nanowires was typically in the range 200-350 nm, and the length in the range 15-25 µm. The thicknesses of the p- i- and n-layers were approximately 100-120 nm, 15 nm and 60-80 nm, respectively. The doping concentration was 3.5×10^{19} cm^{-3} for p-doping and 5×10^{18} cm^{-3} for n-doping, as estimated from planar growth.

6.8 2D MoS_2

The MoS_2 samples that were investigated in this work originated from synthetic, bulk MoS_2 (2H phase) crystals purchased from HQ Graphene [177]. The crystals were n-doped with a carrier density of $\sim 10^{15}$ cm^{-3}. 2D MoS_2 samples were produced by mechanical exfoliation using the Scotch tape method [106], see section 3.1.

7. Results and discussion

This chapter summarizes and discusses the work carried out during my PhD-studies. Most of the work is published in the appended papers, but there is also additional work described in this chapter that has not been published yet. The chapter is divided in two main parts. The first part presents the results on GaAs nanowires, which constitutes the main part of my PhD-work. The second part of the chapter presents the work on 2D MoS_2. The first part starts by describing how the in situ STM-(FIB)SEM technique was used to characterize individual nanowires, which is further elaborated in Paper I and Paper III. Then the electrical contact on single nanowires and its optimization are addressed. This is the topic of Paper IV. After that, the photovoltaic properties of the radially doped p-i-n GaAs nanowires are investigated, which is part of Paper I. Subsequently, the effect of elastic strain on the electrical and photovoltaic nanowire properties is presented and discussed, which is the focus of Paper II (for p-doped GaAs nanowires) and Paper III (for p-i-n doped GaAs nanowires). The second part begins by showing how the in situ STM-FIBSEM setup or just FIBSEM were used to obtain freestanding 2D MoS_2 flakes for TEM studies and straining experiments. Then in situ studies of strain-effects on 2D MoS_2 using either the STM-FIBSEM setup or the piezo-based straining device are presented.

7.1 GaAs nanowires

Individual as-grown nanowires were characterized in SEM and FIB-SEM using the in situ STM-setup described in section 6.5. An SEM image of a nanowire contacted by the STM-probe is shown in Figure 7.1 (a). After the STM-probe was brought into contact with the tip of a single nanowire, Pt-deposition enabled by the GIS of the FIB-SEM was used to weld the STM-probe to the nanowire. This stabilized the contact, increased the contact area and enabled strain to be applied to the nanowire by moving the STM-probe. A schematic illustration of the in situ experimental setup is shown in Figure 7.1 (b). Both homogeneously p-doped GaAs nanowires and radially p-i-n doped GaAs nanowires were characterized using this setup. In the case of radially p-i-n doped nanowires, the p-doped core is connected through the p-doped Si substrate, and the n-doped shell is connected by the STM-probe and Pt-deposition. The external circuit enables current-voltage (I-V) measurements.

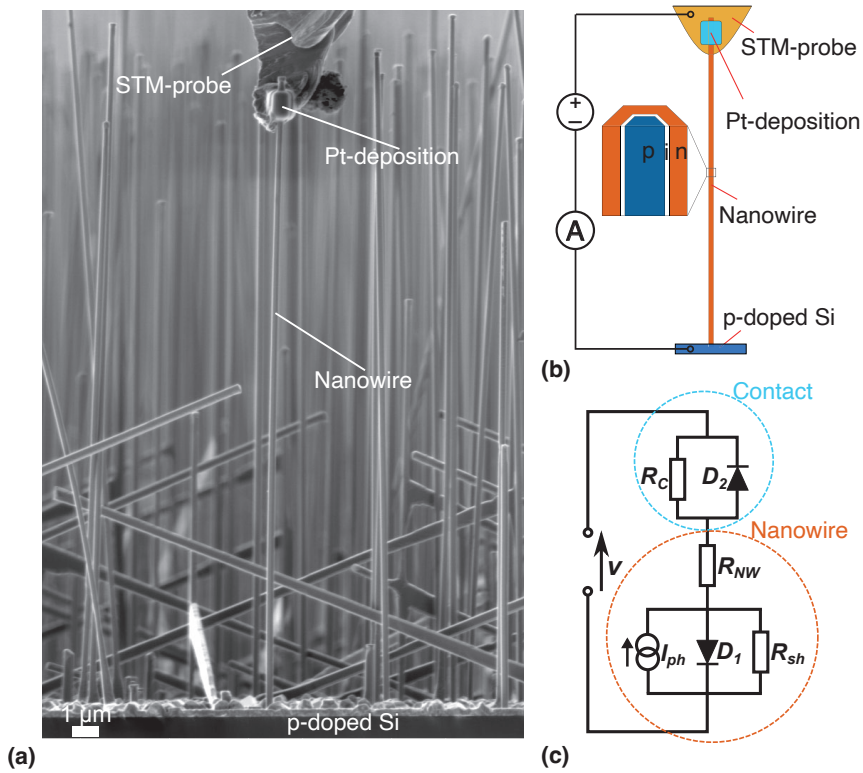

Figure 7.1: **(a)** Secondary electron SEM image of an individually contacted GaAs nanowire. **(b)** Schematics of the experimental system. The STM-probe and the nanowire are attached through Pt-deposition. The external circuit contains a pico-ammeter and a power supply, enabling I-V measurements. **(c)** Equivalent electrical circuit of the experimental system. The contact is represented by a Schottky diode and a resistance in parallel. The nanowire is represented by a p-n diode, a current generator, a series resistance and a shunt resistance.

In order to analyze the single nanowire I-V characteristics quantitatively, the equivalent electrical circuit shown in 7.1 (c) was used to model the system. The nanowire is represented by a p-n diode (D_1), a current generator (I_{ph}) , a shunt resistance R_{sh} and a series resistance R_{NW}, just as in the single diode model for solar cells, and therefore equation 2.3 governs the current through the nanowire. The contact between the STM-probe/Pt-deposition and the nanowire is represented by a Schottky diode (D_2), since it is a metal-semiconductor contact, and a shunt resistance, R_C. The current through D_2 is governed by equation 5.2 or 5.3, depending on the voltage drop at the contact V_{D_2}. Applying Kirchoff's voltage law to the circuit, we get

$$V = V_{D1} + V_{D2} + V_{NW}, \tag{7.1}$$

where V is the supplied voltage and V_{D1} and V_{NW} are the voltage drops at the p-i-n junction and the undepleted part of the nanowire, respectively. By solving the system of equations 2.3, 5.2 or 5.3 and 7.1 numerically, we may find the total current

through the circuit as a function of applied bias. This model is further discussed and applied in paper II-IV.

7.1.1 Microstructure

The microstructure of the nanowires was investigated using TEM imaging and diffraction. As-grown nanowires were mechanically fractured from the growth substrate and transferred to a TEM-grid. The structure of a representative nanowire is shown in Figure 7.2. The high resolution TEM (HRTEM) micrograph and the corresponding electron diffraction pattern in Figure 7.2 (a) and (b) reveal that the crystal structure of the nanowire is ZB. They also show that the nanowire contains twin planes, oriented perpendicular to the long axis of the nanowire, and that a

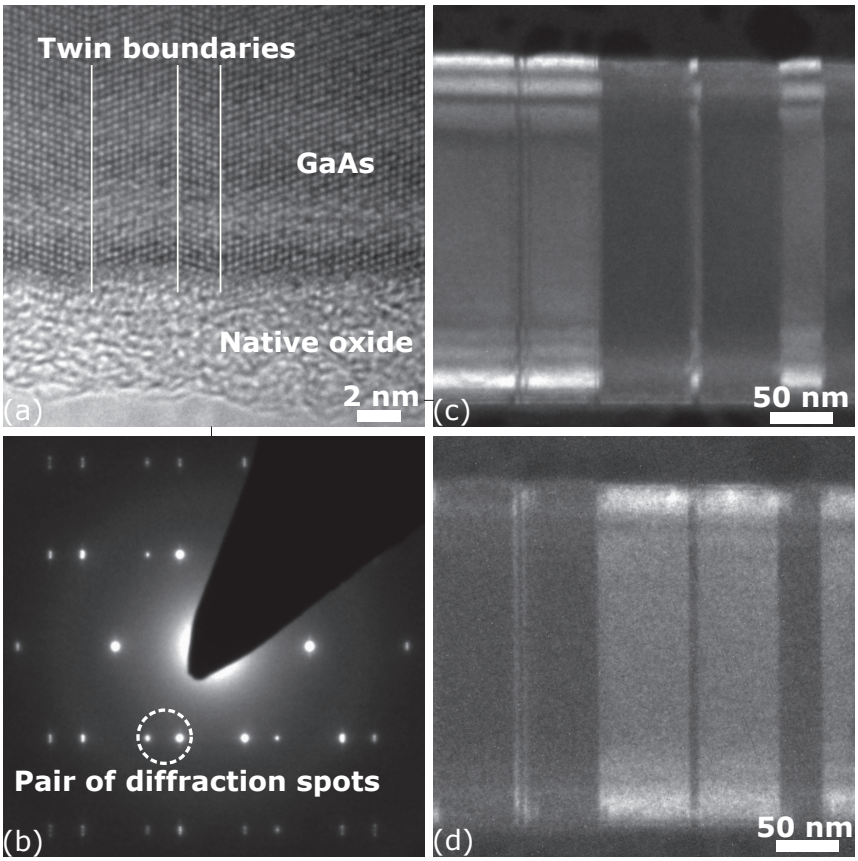

Figure 7.2: **(a)** and **(b)**: High resolution TEM image of a GaAs nanowire and a corresponding diffraction pattern. Twin planes, where the crystal orientation changes, are visible in the image and show up as pairs of spots in the diffraction pattern. **(c)** and **(d)**: Dark field images recorded at lower magnification showing the spatial distribution of twin domains. Dark areas in the upper image are bright in the lower and vice versa, because the two images were generated by choosing one or the other diffraction spot in a pair. The horizontal stripes are a result of sample thickness variation across the nanowire.

native oxide layer with thickness ∼5 nm is present at the nanowire surface. In the diffraction pattern, many diffraction spots appear in pairs. This is a result of the twins and the two spots in a pair correspond to the two sets of twins in the nanowire. The dark field TEM image in Figure 7.2 (c) was obtained by choosing only one of the spots in a pair and in (d) the other spot was chosen to form the image. In this way, the distribution of twins and TPs are revealed at a larger scale. It is evident that even though a few TPs are located in close vicinity, most of them are separated by more than 50 nm, and should therefore not have a significant effect on the charge transport in the nanowires, see section 3.2.

7.1.2 Electrical contact

The quality of the electrical contact between the probe and the nanowires is crucial for the electrical measurements. An example of an I-V measurement on a radially

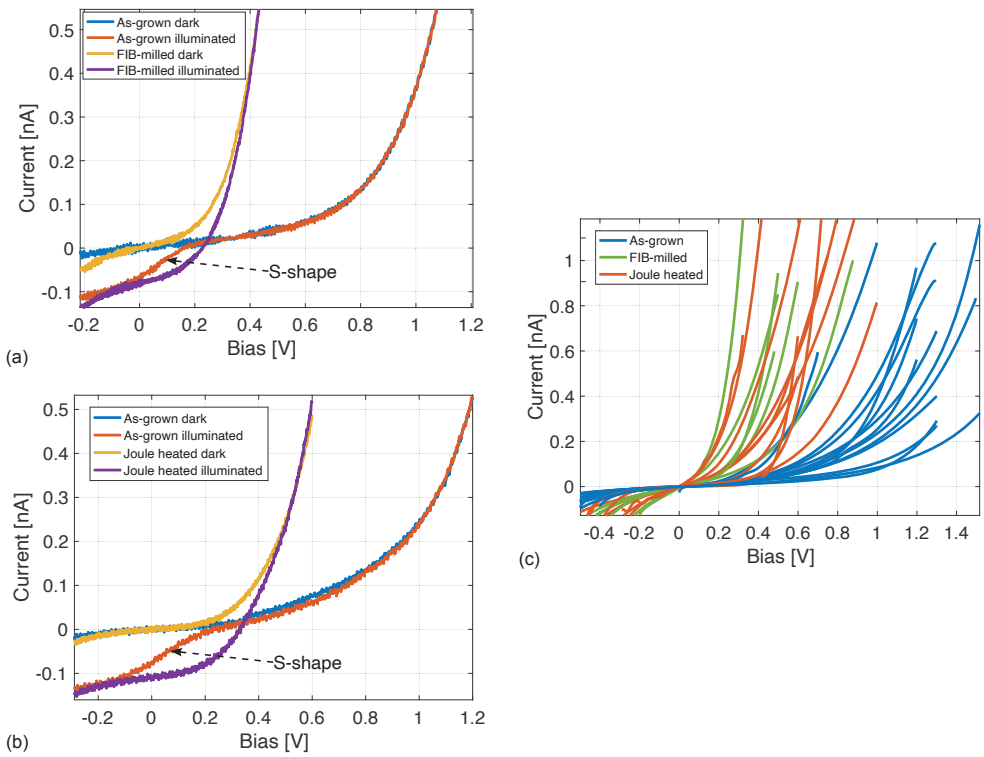

Figure 7.3: **(a)** Dark and illuminated I-V characteristics of a nanowire contacted as-grown and another nanowire that was FIB-milled at the contact area. The as-grown nanowire has an S-shape in the illuminated I-V curve and lower forward current than the FIB-milled one. **(b)** Dark and illuminated I-V characteristics of a single nanowire before (as-grown) and after contact optimization by Joule heating. The effect of Joule heating is similar to that of FIB-milling. **(c)** Dark I-V characteristics of a large selection of nanowires that was either contacted as-grown, FIB-milled or Joule heated.

p-i-n doped GaAs nanowire contacted as-grown using the in situ setup is shown in Figure 7.3 (a). The illuminated I-V curve does not follow the superposition principle which is applicable for a high quality solar cell. Instead it is S-shaped around zero bias, reducing both the I_{SC}, V_{OC} and FF of the solar cell. This S-shape is due to the formation of a current-rectifying Schottky barrier at the semiconductor-metal contact, as discussed in section 5.2.2. In order for the I-V characteristics to represent the intrinsic properties of the nanowires, the contact must first be optimized. Two different strategies for contact-optimization were developed. The first one was to ion mill the surface of the nanowire at the contact area, before connecting the probe and the nanowire. This was done using a focused Ga ion beam with an acceleration voltage of 2 kV and a beam current of 27 pA in a FIBSEM. Figure 7.3 (a) shows the I-V characteristics of a milled nanowire, and there is no S-shape of the illuminated I-V curve. The dark forward current is also significantly higher in the FIB-milled nanowire than the nanowire contacted as-grown. Hence, the contact is improved by the ion milling.

The other strategy to improve the electrical contact was to apply Joule heating to heat up the contact area until the contact resistance is reduced. In practice this was done by contacting a nanowire with the STM-probe and Pt-deposition and apply a large bias so that a current of around 1-2 µA passed through the contact. Since the contact is the most resistive part, most heat is generated there. However, at some point the contact resistance will quickly drop and the current will increase significantly. If the current reaches values >5 µA, there is a risk that the nanowire is damaged. A series resistance of 5 MΩ was therefore added to the circuit during Joule heating, and the bias was kept below 20 V. Figure 7.3 (b) shows the dark and illuminated I-V characteristics of a single nanowire before and after Joule heating. It is clear that this treatment improves the quality of the contact, since the S-shape disappears and the dark current increases afterwards. Figure 7.3 (c) shows the I-V characteristics under dark conditions for a large selection of nanowires. Each curve corresponds to a unique wire, either contacted as-grown, FIB-milled or Joule heated. The trend is clear; both FIB-milled and Joule heated contacts generally result in a higher current at a certain applied bias than as-grown contacts. The FIB-milling is the most reliable and reproducible one of the two procedures, since it is controlled by the settings of the FIB-instrument. Joule heating is less controllable and may harm the nanowires even though precautions are made. However, Joule heating is a good option when the experiment is performed in a regular SEM, without access to an ion beam.

To gain insight of the reason behind the contact-improvement, TEM characterization of an as-grown nanowire and a FIB-milled nanowire was carried out, see Figure 7.4. Cross-sectional TEM lamellae of the two different nanowires were prepared by FIBSEM lift-out. In 7.4 (a), an overview image of the as-grown nanowire is shown. The nanowire cross section has a regular hexagonal shape, with the facets aligned to the {1 -1 0} crystallographic planes. There is a layer of bright contrast surrounding the nanowire. A zoom-in on one of the nanowire facets (7.4d) shows that there is an approximately 4-5 nm thick amorphous layer separating the GaAs from the EBID-Pt. This amorphous layer is a native oxide layer consisting of ∼ 70 % O and ∼

30 % Ga, according to energy dispersive x-ray spectroscopy (EDS) (see Paper IV). As discussed in section 5.2.1, an insulating layer between the semiconductor and the metal reduces the tunnelling probability through the Schottky barrier and can significantly reduce the electrical current. Figure 7.4 (b) shows a TEM micrograph of a cross section of a nanowire of which the surface has been ion milled. The oxide layer is removed at two facets of the nanowire. By comparing the shape of the cross section to a regular hexagon, it can be estimated that a surface layer of approximately 15 nm has been milled away from the nanowire. The outermost part of the nanowire that has been exposed to the ion beam has a darker contrast, (7.4e), indicating that this region is structurally different from the rest of the nanowire. A dark field TEM micrograph of the FIB-milled nanowire cross section is shown in 7.4 (e). The DF image was obtained by placing the objective aperture around one of the (2 2 0) diffraction spots in the diffraction pattern shown in 7.4 (f). Within the area of bright contrast, the nanowire is still crystalline. By comparing this area to the nanowire contour (dashed blue line), we can conclude that the outermost 10-20 nm of the exposed nanowire facets are amorphous. In total, the outermost 25-35 nm of

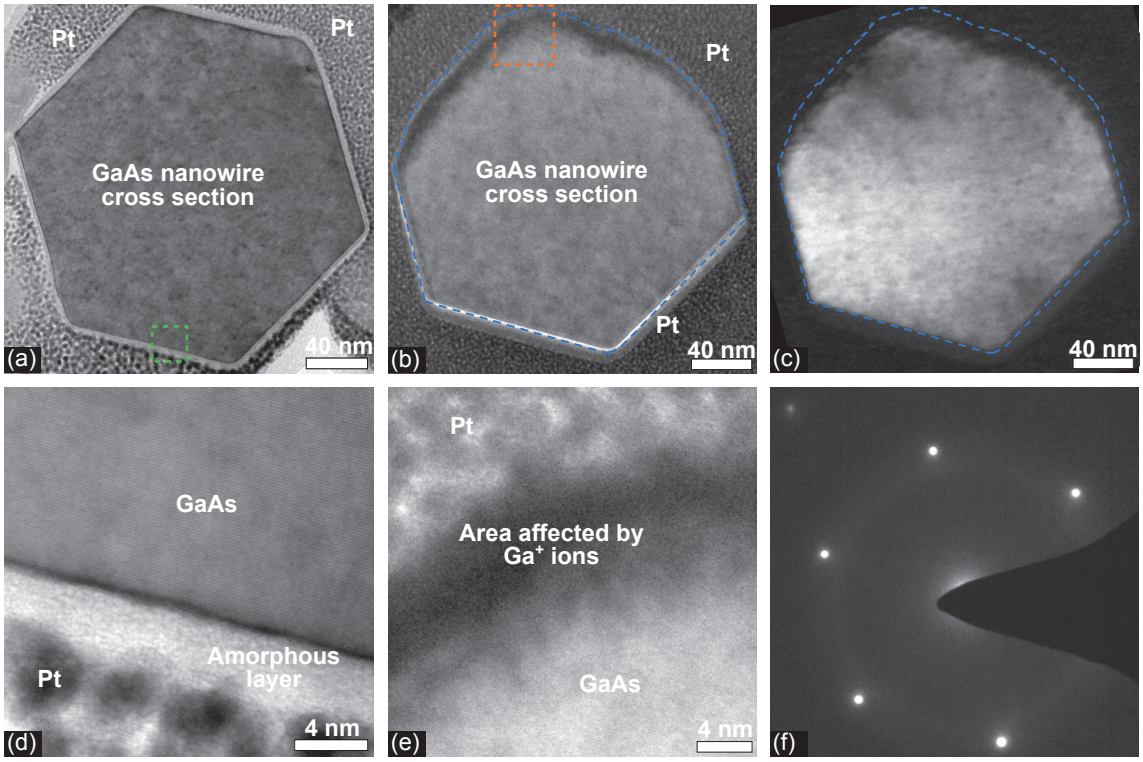

Figure 7.4: **(a)** TEM micrograph of a cross-sectional sample of an as-grown nanowire. **(b)** TEM micrograph of cross sectional sample of a FIB-milled nanowire. Part of the nanowire itself has been milled away. **(c)** Dark-field TEM micrograph of the FIB-milled nanowire. The blue dashed line represents the contour of the nanowire cross section in the micrograph shown in (b). **(d)** Zoom-in of the area marked with a green square in (a). The Pt and the GaAs are separated by an amorphous layer. **(e)** Zoom-in of the area marked with an orange square in (b). **(f)** Diffraction pattern of the FIB-milled nanowire cross section.

the nanowire has been milled away or structurally damaged by the FIB-treatment. The thickness of the n-doped shell of the nanowire is approximately 60-80 nm, so the ion beam damage should not have reached the junction.

For further understanding of the mechanism of the contact-improvement, the model circuit in Figure 7.1 (c) were used to fit the experimental I-V characteristics of a nanowire with as-grown contact and one with FIB-treated contact, see Figure 7.5. The simulated I-V characteristics of a p-n junction with Ohmic contact is included as reference. In the low bias regime (7.5a), the I-V curve of the FIB-milled nanowire is similar to the one with Ohmic contact. For the nanowire contacted as-grown (i.e. no ion milling or Joule heating), the I-V curve differs significantly from the Ohmic, both with respect to the S-shape and the magnitude of the forward current. At high bias (7.5b), both the FIB-milled and the as-grown nanowires have lower forward current than the Ohmic case. The FIB-milled nanowire still has higher forward current than the as-grown nanowire though. The parameters that were used for the numerical data-fitting are presented in Table 7.1.

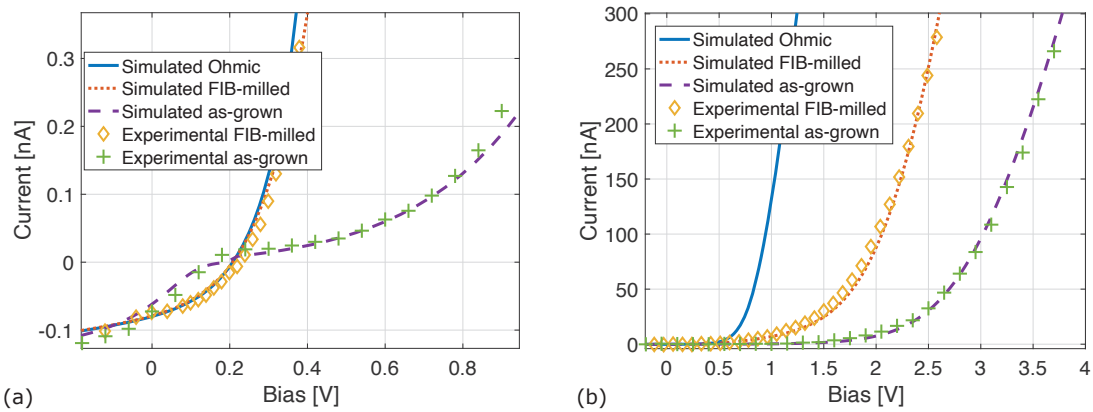

Figure 7.5: Fits to the experimental illuminated I-V characteristics of a nanowire contacted as-grown and one FIB-milled. The I-V characteristics in the case of perfect Ohmic contact is included as reference. **(a)** Low bias regime. **(b)** High bias regime.

According to the data-fitting, the improvement of the FIB-milled contact compared to the as-grown contact is mainly due to a reduction in R_C (the shunt resistance of the contact) and δ (the thickness of the insulating layer). The shunt resistance of a Schottky barrier influences the I-V characteristics at low bias (see section 5.2.1), so the reduction of R_C is the main reason for the disappearance of the S-shape. The reduction of δ is the main reason for the increased current at high bias. From the TEM characterization, we know that the native oxide layer is milled away by the FIB-treatment, making the Pt in more direct contact with the nanowire, explaining the reduction in δ. The TEM characterization and EDS analysis also revealed amorphization and Ga-implantation at the metal/nanowire interface due to the FIB-treatment. This may give rise to trapped charges and electronic states within the band gap [178], which may form an alternative current path through the junction, and explain the reduction in R_C.

Table 7.1: Parameters for numerical fitting of I-V curves in Figure 7.5. n_1 and n_2 are the ideality factors for the p-n diode and the Schottky diode, respectively. The rest of the parameters are introduced in the main text.

	As-grown	FIB-milled	Ohmic
R_{Sh} [GΩ]	12	12	12
R_C [GΩ]	100	0.08	–
R_{NW} [MΩ]	2.0	2.0	1.0
I_S [pA]	10	7.0	7.0
I_{Ph} [pA]	100	80	80
ϕ_b [eV]	0.365	0.5	–
ξ [eV]	0.02	0.02	–
δ [Å]	40	15	–
N_d [m^{-3}]	5.7	6.3	–
n_1	3.5	3.5	3.5
n_2	1	1	–
χ [eV]	0.1	0.1	–
S [µm^2]	6	6	–

7.1.3 Photovoltaic properties

Using either the FIB-milling or Joule heating process to establish high quality contacts, the intrinsic photovoltaic properties of individual GaAs nanowires with radial p-i-n junctions were investigated. The I-V characteristics of two different nanowires during white LED illumination are shown in Figure 7.6 (a). Table 7.2 shows the corresponding photovoltaic parameters. It should be noted that the PCE-values received for single nanowires using our setup cannot be directly compared to PCE-values received from standardized tests on full scale solar cells. One reason is that the waveguiding effect of the nanowires makes the area to be used in the calculation of the total incoming light intensity ambiguous. Another reason is that the the wavelength spectrum of the white LED is not equal to the solar spectrum, see Figure 7.6 (b). Furthermore, the LED-light is incident at an angle of 10-40° relative to the sample normal, as opposed to standardized conditions where the incoming light is parallell to the sample normal. Additionally, part of the incoming light may be blocked by the STM-probe and other nanowires. Therefore, the use of the PCE values should be limited to the internal comparison of the performance between individual nanowires.

We see in Table 7.2 that Nanowire 2 has high V_{OC} and FF, resulting in a high PCE despite a low I_{SC}. Nanowire 1 has lower V_{OC} and FF, but significantly higher I_{SC}, resulting in the highest PCE. By using the model circuit in Figure 7.1 to perform numerical data-fitting of the I-V curves in Figure 7.6, the parameters describing the p-i-n junctions of the wires were extracted, see the three rightmost columns of Table 7.2. The most distinguishing feature is I_S, which is significantly lower for Nanowire 2. One probable reason for this is that Nanowire 1 was ∼25 µm long while Nanowire

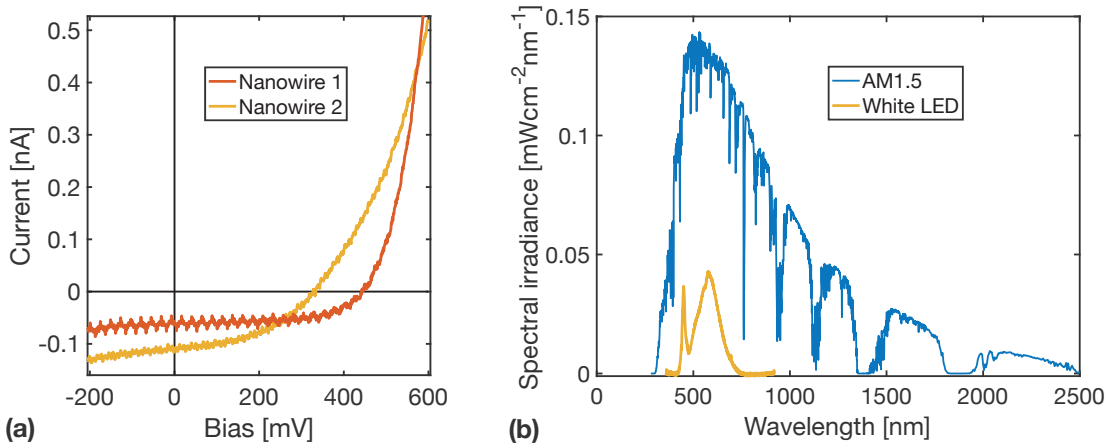

Figure 7.6: **(a)** I-V characteristics of two different nanowires during white LED illumination. The periodic noise present for Nanowire 1 stems from the surrounding electrical grid, because the setup was not optimally shielded at the time. **(b)** Comparison between the solar spectrum AM1.5 and the white LED spectrum.

2 was ∼10 µm long. The area of the p-i-n junction scales with the nanowire length due to its radial geometry, which in turn affects I_S, as discussed in Section 2.3.4. The shorter nanowire may therefore have a lower I_S and as a result a higher V_{OC}, according to equation 2.4. The shorter nanowire also has a smaller smaller area exposed to the illumination, which may explain the low I_{SC} for Nanowire 2.

Table 7.2: Photovoltaic and electrical parameter values of individual nanowires

Nanowire	I_{SC} $[pA]$	V_{OC} $[mV]$	FF	PCE	R_{sh} $[G\Omega]$	I_S $[pA]$	n
1	110	330	0.44	10.8%	40	2.5	4
2	61	442	0.59	9.7%	40	0.01	2.3

The interpretation of the illuminated I-V measurements above assumes that it is only the nanowire in contact with the STM-probe that contributes to the photocurrent. In principle though, it is not possible to rule out any contribution to the photocurrent from the substrate or from any of the other nanowires considering the I-V measurements alone, since the LED illuminates the whole sample. Furthermore, the I-V measurements can not provide any information about possible local variations of the photoresponse within individual nanowires. In contrast, EBIC mapping provides information about the charge carrier separation and collection efficiency locally with high spatial resolution.

Figure 7.7 shows the result of an EBIC measurement performed on a single nanowire contacted as-grown. A beam current of ∼100 pA and an acceleration voltage of 30 kV of the electron beam were used. The contact was placed ∼5 µm below the tip of the nanowire, see the SEM image in Figure 7.7 (b). In the EBIC map (Figure 7.7a), there is a strong signal throughout the whole nanowire, except where the Pt deposition of the contact blocks the electron beam. There is no contribution from the surrounding nanowires or the substrate. This confirms the existence of the

radial p-i-n junction and that it is indeed only the contacted nanowire that gives rise to the photocurrent in the I-V measurements. In the SEM image (Figure 7.7b), a feature is visible at the tip of the nanowire. A close comparison between the EBIC map and the SEM image shows that there is no EBIC signal within this feature. This suggests that there is no active p-i-n junction there. A possible explanation is that the catalytic Ga-droplet was not completely consumed during the growth of the nanowire, and remained as a solidified, inactive Ga particle at the nanowire tip. At the very bottom of the nanowire, the signal increases significantly and it has been deliberately cut-off at 2.7 nA for a better display of the EBIC map. The true maximum of the signal here is 6.6 nA. This is most likely due to the fact that the thickness of the nanowire increases here. At 30 kV acceleration voltage, most of the beam is transmitted through the thin nanowire, see Figure 6.4. Increasing the thickness will increase the number of absorbed electrons, and therefore also the number of generated electron-hole pairs. For the same reason, the EBIC signal varies along a line perpendicular to the long axis of the nanowire, with the highest value in the centre, which is the thickest part of the nanowire.

The EBIC signal in the centre of the wire is plotted as a function of position along the long-axis in Figure 7.7 (c). The profile reveals a slight dip in the EBIC signal at

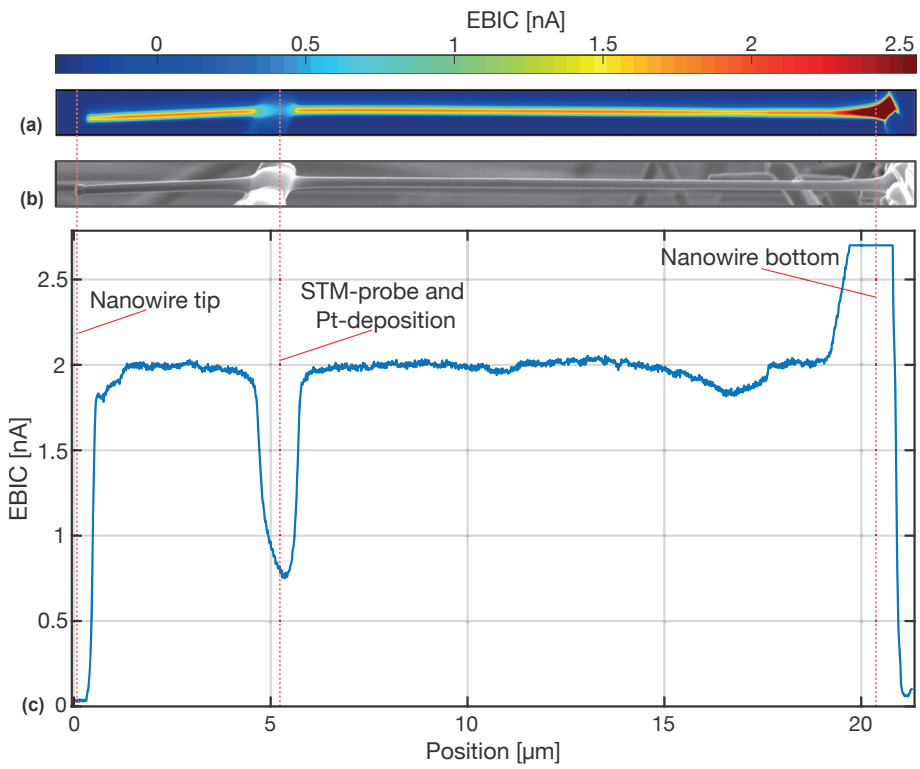

Figure 7.7: **(a)** EBIC map of an individual nanowire contacted as-grown. The whole nanowire is active except for the first ∼200 nm at the tip. The electron beam is partially blocked by the Pt-deposition at the contact, and the EBIC signal is reduced here. At the bottom of the the nanowire, the EBIC signal increases significantly due to increased thickness of the wire. **(b)** Corresponding secondary electron SEM image of the contacted nanowire. **(c)** EBIC signal along the nanowire.

around 17 µm from the tip. There is no obvious feature in the SEM image that could be related to this dip, and therefore it could be related to internal structure defects. Otherwise, the signal is quite stable at around 2 nA, except for at the tip, contact and bottom as discussed before. The high degree of homogeneity of the EBIC signal in the wire indicates high quality of the nanowire fabrication. It is worth pointing out that the EBIC signal is similar both above and below the contact, suggesting that the photovoltaic performance is independent of the placement of the contact. This feature is attributed to the radial geometry of the p-i-n junction.

7.1.4 Effects of elastic strain

The strain-induced effects on the electrical and photovoltaic properties of individual nanowires were investigated using the in situ STM-SEM setup. The nanowires were exposed to uniaxial tensile or compressive strain by moving the STM-probe either away from or towards the substrate. In many cases, more than 3% tensile strain could be applied before the fracture of the wires. Figure 7.8 shows the result of one such measurement on a p-i-n doped nanowire. This nanowire was FIB-milled to optimize the contact. The average strain was calculated by dividing the elongation of the wire by its original length. The elongation and the length were measured from the SEM images shown in 7.8 (a). At each strain level, the dark I-V characteristics were measured, see 7.8 (b). The strain had significant effects on the I-V characteristics. In order to investigate the reversibility of these effects, the nanowire was relaxed and strained once more. The I-V characteristics during the first and the second straining cycle agreed well, showing that the strain-induced effects were indeed reversible. Again, the model circuit in Figure 7.1 was used for numerical data-fitting of the I-V curves, in order to quantitatively determine the effect of strain upon the nanowire electrical properties. Figure 7.8 (c) shows that the I_S of the p-i-n junction increases as a function of strain. With I_S being known, equation 2.2 was used to calculate E_g as a function of strain. The result is shown in Figure 7.8 (d). According to this, E_g decreases monotonously with increasing strain, from 1.42 eV at zero strain to around 1.2 eV at 3 % strain.

The nanowire resistance, R_{NW}, was also affected by the strain. Figure 7.9 shows R_{NW} as a function of strain for 5 different nanowires, two with p-i-n doping and three with only p-doping. The trend for all of the wires is the same: the resistance increases at moderate strain levels, up to around 1-2%, but as the strain increases further, R_{NW} starts to decrease instead. This effect is attributed to the strain-induced energy splitting of the degenerate heavy and light hole bands in GaAs. This splitting causes the average effective hole mass to increase, which in turn increases the resistivity. However, at high strain levels the splitting of the bands is large enough to suppress interband phonon scattering, which in turn decreases the resistivity. At high strain levels, the suppression of phonon scattering is the dominating factor and therefore the total nanowire resistance decreases.

Furthermore, the parameters ϕ_B, R_{sh} and R_C, all decreased with increasing strain.

ϕ_B and R_C are parameters of the contact, so they may be affected by structural changes to the Pt-GaAs interface induced by the movement of the STM-probe, in addition to the elastic strain in the nanowire. The reduction of R_C might be due to a more direct contact between the Pt and GaAs as force is applied to the contact. ϕ_B is closely related to the band gap of the semiconductor, so the reduction of ϕ_B is likely due to the reduction of E_g induced by the strain. In the simple picture where the Fermi level of the Pt is pinned mid-gap, one could expect ϕ_B to decrease half as much as E_g. However, ϕ_B decreases only by ~0.04 eV, which is only about one fifth of the reduction in E_g. This is probably because the strain induced at the contacted area is less than in the rest of the nanowire. The reduction of R_{sh} is potentially detrimental for the photovoltaic performance of the nanowire. The origin of the shunt resistance could be that the n-doped shell is in direct contact with the Si substrate at the bottom of the nanowire, forming a leakage current path

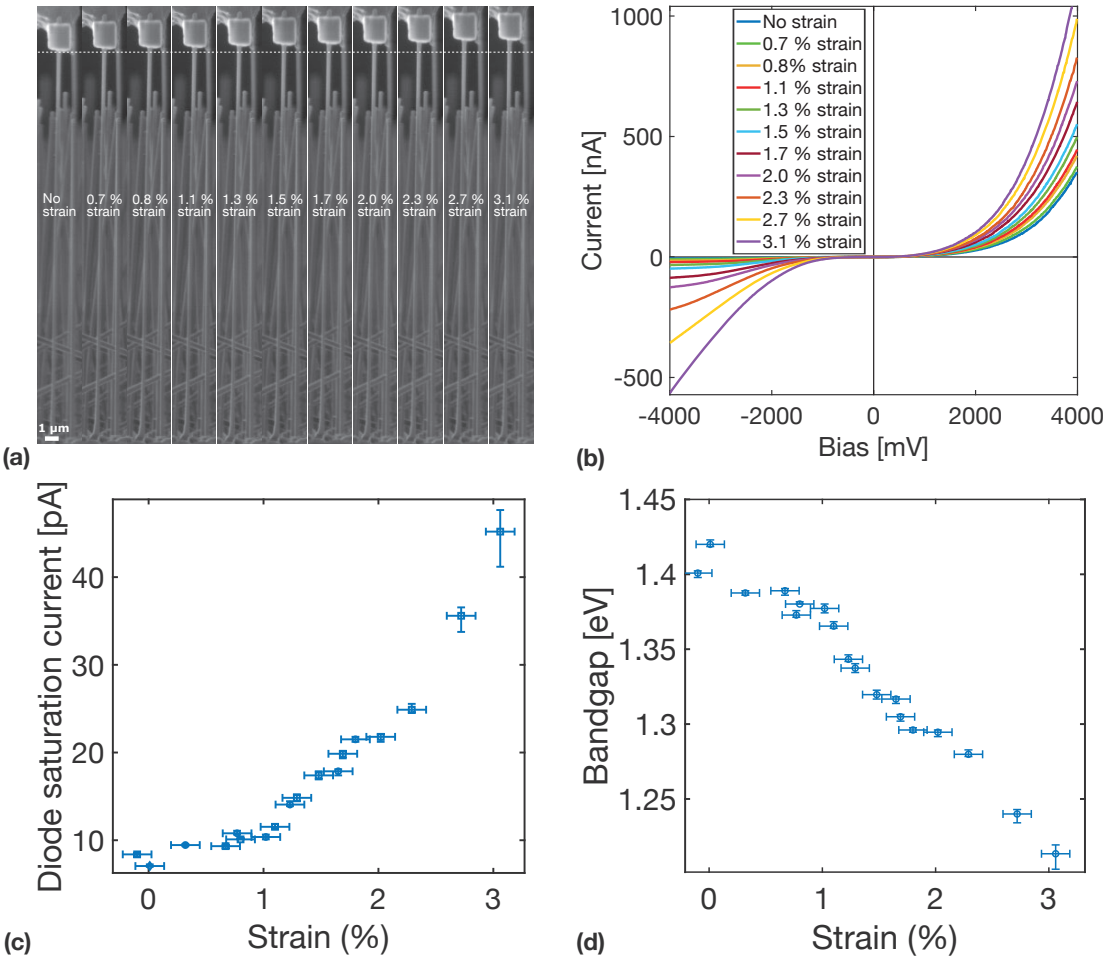

Figure 7.8: **(a)** Secondary electron SEM images showing one straining cycle of a single GaAs nanowire with radial p-i-n junction. **(b)** I-V characteristics corresponding to the different straining levels. **(c)** Diode saturation current of the p-i-n junction as a function of strain. **(d)** Band gap energy of the nanowire as a function of strain.

past the p-i-n junction. Since the substrate is p-doped, a hetero-junction should exist at the interface between the nanowire shell and the substrate. As the band gap of the nanowire is reduced, the potential barrier of this junction could also be reduced, and this could be an explanation of the reduction in R_{sh}.

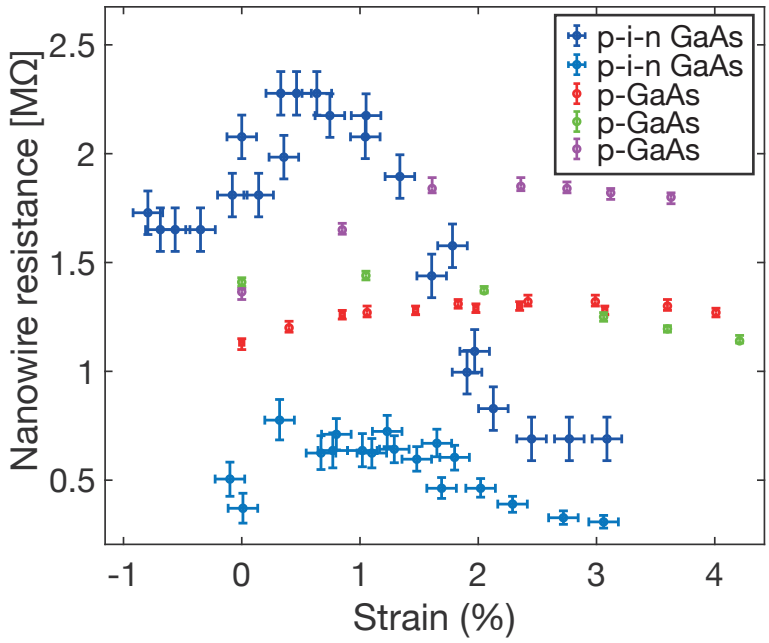

Figure 7.9: Nanowire resistance as a function of strain for five different nanowires, two with radial p-i-n junctions and three p-doped.

So far, only the effect of strain on the dark I-V characteristics has been considered. Now we move on to the case where the nanowires are illuminated, to study the strain-induced effects of the photovoltaic properties. Two nanowires were illuminated with near-infrared (NIR) LED and one with a green LED, see Figure 7.10 (a) for the different LED wavelength spectra. The corresponding I-V characteristics are shown in Figure 7.10 (b-d). In the case of NIR LED illumination (Figure 7.10b and c), at least three different effects of strain can be discerned directly from the illuminated I-V characteristics. First, the I-V curves are shifted downwards on the negative bias side, which means the photocurrent increases with increasing strain. Second, the shape of the I-V curves at positive bias changes so that a higher forward current is reached at a specific applied voltage as the strain increases. This is similar to the dark I-V characteristics and it is a consequence of the reduced I_S. Lastly, the slope of the I-V curves around zero bias increases with increasing strain, indicating a reduced R_{sh}. In the case of green LED illumination (Figure 7.10d), no increase in photocurrent occurs. The effect of strain on the shape of the I-V curves and the slope around zero bias, is similar for green LED illumination as for NIR LED illumination.

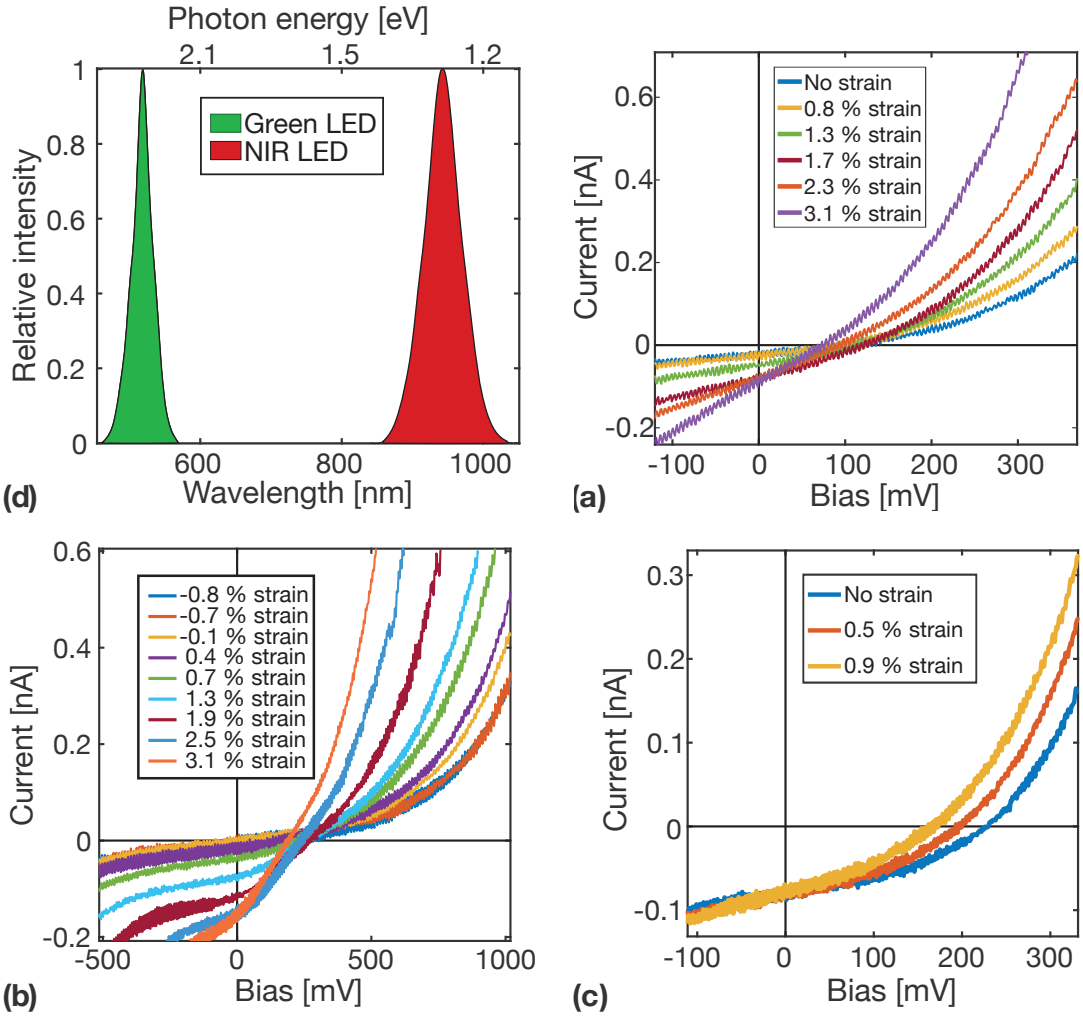

Figure 7.10: **(a)** Normalized light intensity as a function of wavelength for the green LED and the NIR LED that were used to illuminate the nanowires during straining. **(b)** I-V characteristics of a single nanowire during NIR LED illumination at different strain levels. **(c)** I-V characteristics of another single nanowire during NIR LED illumination at different strain levels. **(d)** I-V characteristics of a third single nanowire during green LED illumination at different strain levels.

The parameters I_{SC}, V_{OC}, FF and PCE, describing the photovoltaic performance of the three nanowires, are plotted as a function of strain in Figure 7.11 (a-d), respectively. In the case of NIR LED illumination, I_{SC} is small at zero strain and increases with increasing strain until it reaches a plateau, see Figure 7.11 (a). For green LED illumination though, it starts at a high value and is not significantly influenced by the strain. This can be explained by examining the wavelength spectra for the two different LED:s. For the green LED, all the photons have energies well above 1.42 eV which is the band gap energy of GaAs. These photons will therefore be absorbed regardless of the strain applied. For the NIR LED though, most photons have energies below 1.42 eV and will not get absorbed in an unstrained nanowire. When the nanowire is strained though, the band gap decreases and the NIR photons

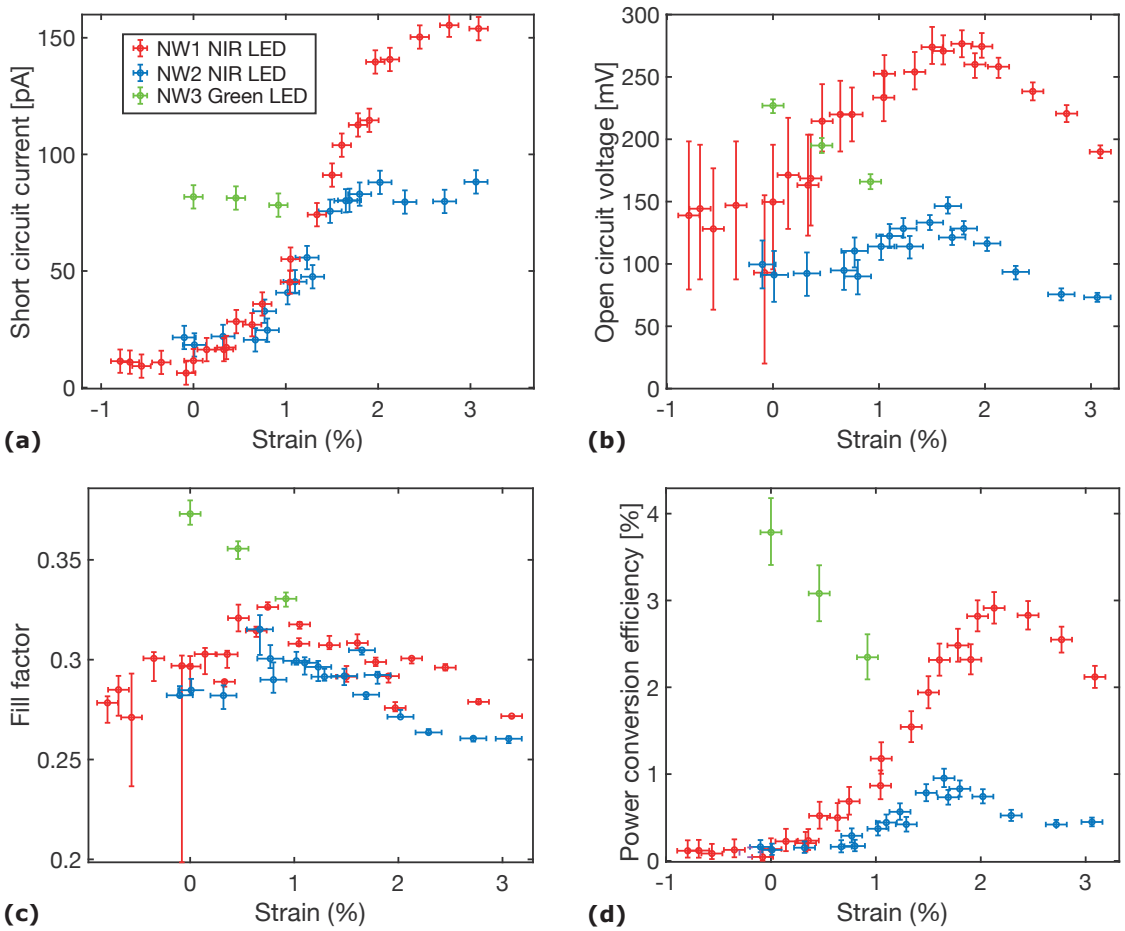

Figure 7.11: The photovoltaic parameters I_{SC} **(a)**, V_{OC} **(b)**, FF **(c)** and PCE **(d)** as a function of strain for three different nanowires. Nanowire 1 and 2 were illuminated with a NIR LED and nanowire 3 were illuminated with a green LED.

can get absorbed. The increase in I_{SC} is thus consistent with the calculated shift in E_g due to strain shown in Figure 7.8 (c). The plateau is reached when E_g has shifted outside of the NIR LED spectrum. Had this spectrum been wider, I_{SC} would probably have continued to increase all the way up to 3 % strain. Moving on to Figure 7.11 (b), we see that during NIR illumination, V_{OC} increases up to 1.5-2 % strain, but decreases at higher strain levels. This effect can be explained by considering equation 2.4, which states that V_{OC} is directly proportional to I_{SC}, and inversely proportional to I_S. Since I_{SC} increases significantly between 0 and 2 % strain, V_{OC} also increases. Above 2 % strain though, I_{SC} reaches a plateau, and the reduction in V_{OC} is caused by an increase in I_s. In the case of green LED illumination though, I_{SC} remains almost constant while I_s increases during the straining, causing a monotonous reduction in V_{OC}. FF follows the same trend as V_{OC} for the three respective nanowires. Finally, considering the PCE as a function of strain shown in Figure 7.11 (d), we see that during NIR illumination it increases up to a certain point beyond which it starts to decrease again. Observe that the decline in PCE at high strain is mainly associated with the narrow spectrum of the NIR LED. When the strain no longer leads to more absorbed photons, it only reduces the PCE due to

the reduction in V_{OC}. During green LED illumination, the PCE instead decreases steadily with increasing strain. This is because there is no positive effect of increased absorption, only the negative effect of decreased V_{OC}. These results are in line with the detailed balanced theory discussed in section 2.3.3, which boils down to the fact that for a single band gap solar cell, the optimal band gap energy is a compromise between absorbing as many photons as possible, and utilising as much energy of each absorbed photon as possible.

In order to investigate the effect of tensile strain on the charge-separation ability locally within the nanowires, EBIC mapping was performed. The result of one such measurement is shown in Figure 7.12. The tip of the nanowire was FIB-milled for optimizing the electrical contact. An SEM image of the nanowire in the relaxed state and the corresponding EBIC map are shown in Figure 7.12 (a) and (b), respectively. Figure 7.12 (c) shows the EBIC line profile both in the relaxed and in the strained states. First of all, we notice that the EBIC signal increases towards the bottom of the nanowire, except at the contact were the beam is partly blocked by the deposited Pt. This feature could be due to redistribution of the charge carriers into the junction during their transport to the contacts, leading to recombination.

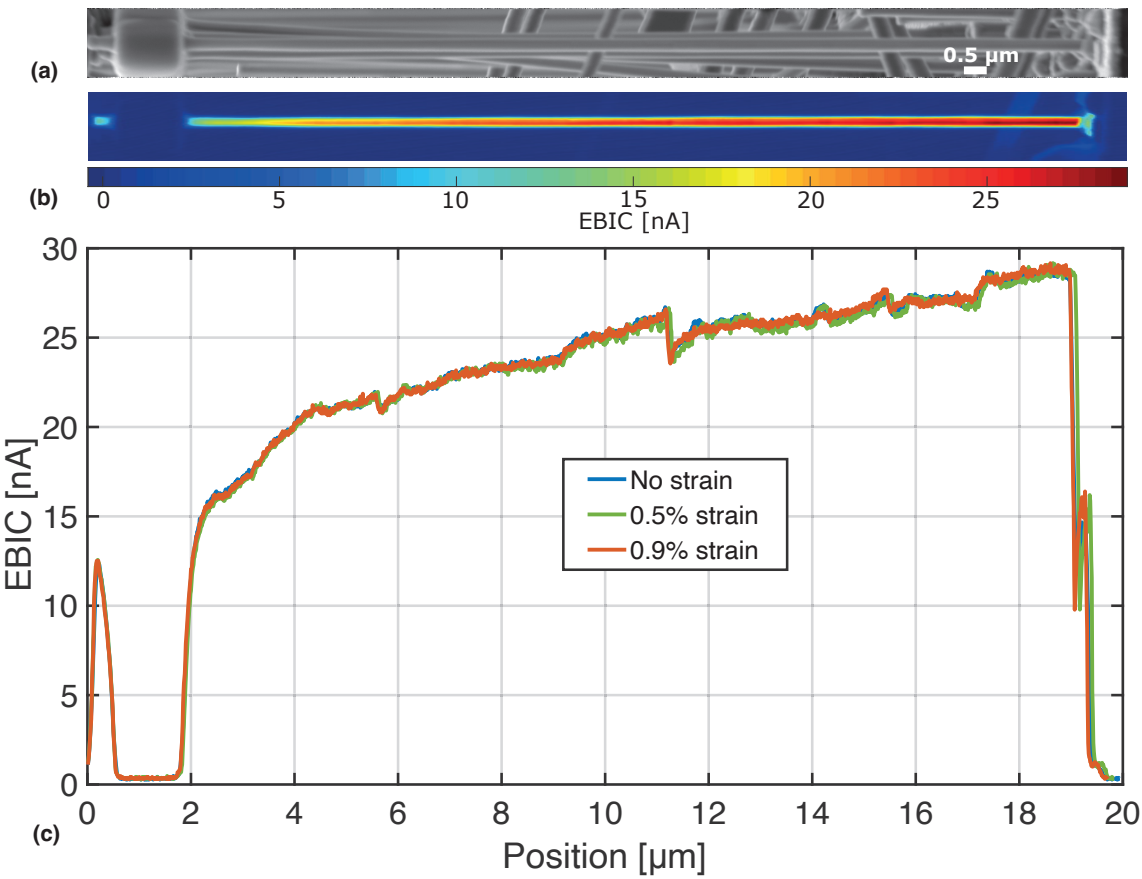

Figure 7.12: EBIC mapping of a FIB-milled nanowire at different strain levels. **(a)** Secondary electron SEM image of the nanowire in the relaxed state. **(b)** Corresponding EBIC map. **(c)** EBIC line profiles at different strain levels. The EBIC signal is not affected by the strain when the contact has been optimized.

The higher the resistance of the transport path is, the more redistribution and recombination occurs [179]. The holes and the electrons have different transport paths. The holes go through the p-doped core of the wire and are collected through the substrate, while the electrons go through the n-doped shell and are collected through the STM-probe. Since the hole mobility is lower than the electron mobility for GaAs, we expect less recombination (and higher EBIC signal) when the hole transport path is shorter, i.e when the electron beam is closer to the bottom of the nanowire. Second, we see that the EBIC profile does not change as tensile strain up to 0.9 % is applied to the nanowire. This shows that the strain does not affect the charge separation ability of the nanowire, and validates that the enhanced photocurrent observed for NIR LED illumination is due to enhanced absorption.

Another way to induce strain in the nanowires is to push the STM-probe towards the substrate. However, this does not result in pure compressive strain since the nanowires tend to bend due to their high aspect ratio. The bending will induce both compressive and tensile strain, since one side of the nanowire will be elongated and the other will be compressed. Furthermore, bending can cause the illuminated area to change and the interaction volume of the electron beam to vary throughout the nanowire, complicating the interpretation of photocurrent and EBIC measurements.

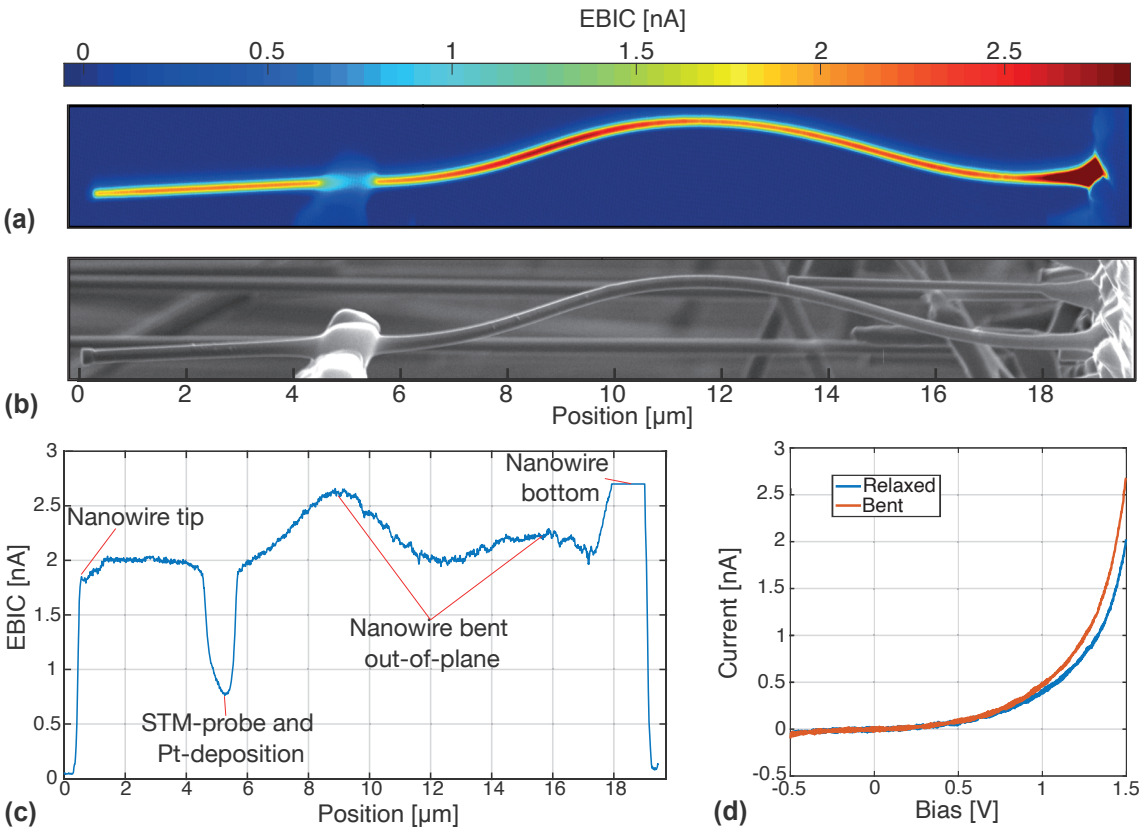

Figure 7.13: Effect of bending on the nanowires. **(a)** EBIC map of a bent nanowire. **(b)** Corresponding secondary electron SEM image of the bent nanowire. **(c)** Corresponding EBIC line profile. The bumps are likely artefacts caused by out-of-plane bending. **(d)** Dark I-V characteristics of the nanowire in relaxed and the bent states.

Nevertheless, a few measurements were performed where the nanowire was bent by pushing the STM-probe towards the substrate. An example is shown in Figure 7.13. This is the same nanowire as is shown in Figure 7.7. The STM-probe was pushed approximately 2 µm towards the substrate, which caused the part of the nanowire below the contact to bend, see Figure 7.13 (b). In the EBIC map (Figure 7.13a), we see that the signal increases at some parts in the bent region. This is more clear in the EBIC line profile shown in Figure 7.13 (c). Two bumps appear at approximately 9 µm and 15 µm below the tip of the nanowire. These are most likely artefacts arising due to the fact that the nanowire did not bend perfectly in-plane. The nanowire surface is therefore tilted with respect to the incoming beam there, and the electron beam travels a longer path through the nanowire. This causes the interaction volume to increase at the positions of out-of-plane bending. More charge carriers are thus generated there and a stronger EBIC signal is measured. Between the two bumps and above the contact though, the EBIC signal remained around 2 nA, which is the same as in the relaxed state (see Figure 7.7). This indicates that the bending does not affect the charge-separation ability of the nanowire. The bending affects the dark I-V characteristics in a similar manner as tensile strain, see Figure 7.13 (d).

7.2 2D MoS_2

2D MoS_2-flakes were investigated using in situ electron microscopy and Raman spectroscopy. The possibility to use the in situ STM-FIBSEM setup and the Omniprobe micromanipulator in a FIBSEM to obtain freestanding 2D-flakes was investigated. Furthermore, two different ways of applying strain to 2D-flakes were explored, one using the in situ STM-FIBSEM setup and one using the custom-made straining device based on a piezo-actuator.

7.2.1 In situ exfoliation, lift-off and transfer

The STM-FIBSEM setup was used to prepare freestanding MoS_2-flakes by in situ exfoliation, an example of this is shown in Figure 7.14. Multilayer flakes were first exfoliated and transferred to either Au, Si or SiO_2 substrates by the Scotch-tape method. Individual flakes were approached by the STM-probe inside the FIBSEM. The fine motion of the STM-probe made it possible to gently touch the flakes without causing damage, something that was not possible with the built-in Omniprobe of the FIBSEM. With the probe touching the edge of one flake, EBID-Pt was used to attach the probe to the flake (Figure 7.14 a). To initiate the exfoliation, the probe was lifted upwards. It was found that this procedure has three possible outcomes. The first is that the Pt-deposition breaks or the flake breaks in the vicinity of the Pt-deposition. The second is that the flake detaches from the substrate and the third is that the topmost layer/layers of the flake start to exfoliate. The outcome

of each specific case depends on a number of factors. The size, thickness and shape of the flake play an important role. Thinner flakes seem to increase the chance for detachment, and thicker flakes increase the chance for exfoliation. Attaching the probe to a corner or an edge of the flake increases the chance of both detachment and exfoliation. The adhesion between the substrate and the flake, and the quality and size of the Pt-deposition also affect the outcome.

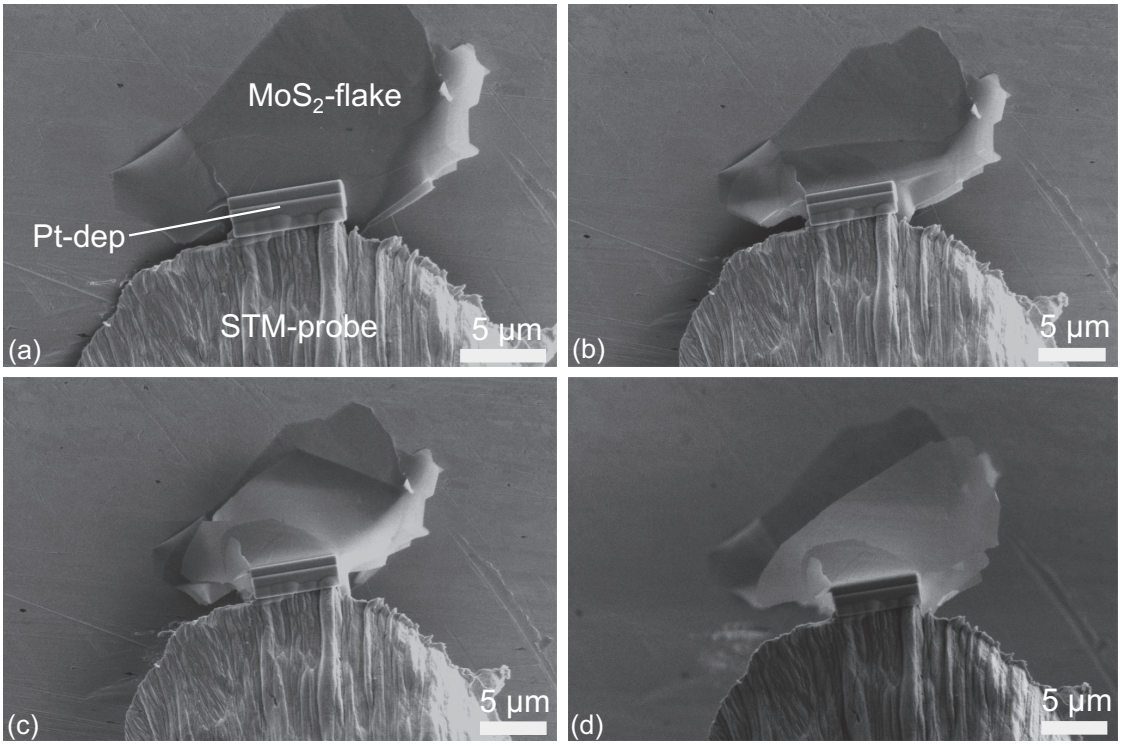

Figure 7.14: Secondary electron SEM images illustrating in situ exfoliation of a multilayer 2D MoS_2-flake using the in situ STM-FIBSEM setup: **(a)** The STM-probe (lower part of the image) is attached by EBID-Pt to the top surface of a MoS_2 flake lying on a Au-substrate **(b)** By slowly lifting the STM-probe upwards, the flake starts to detach from the substrate. **(c)** At some point, the topmost layers of the flake start to detach from the flake and are gradually exfoliated as the probe is lifted further upwards. **(d)** In the end, a freely suspended thin flake is attached to the STM-probe. The mother-flake is still attached to the substrate.

The example shown in Figure 7.14 is a mix between detaching and exfoliation. In the beginning, the flake starts to detach from the substrate (Figure 7.14 b), but as the probe is lifted further the topmost layers starts to exfoliate (Figure 7.14 c) and the mother-flake falls back onto the substrate. Eventually, the topmost layers are completely exfoliated and constitute a thinner, freestanding flake attached to the probe (Figure 7.14 d). Evidently, this method could be used to prepare freestanding multilayer 2D-flakes. However, so far the success rate is rather low and the control of the size and thickness of the prepared flake is limited. Another issue with this method is that the thin, freestanding flakes are sensitive to the electron

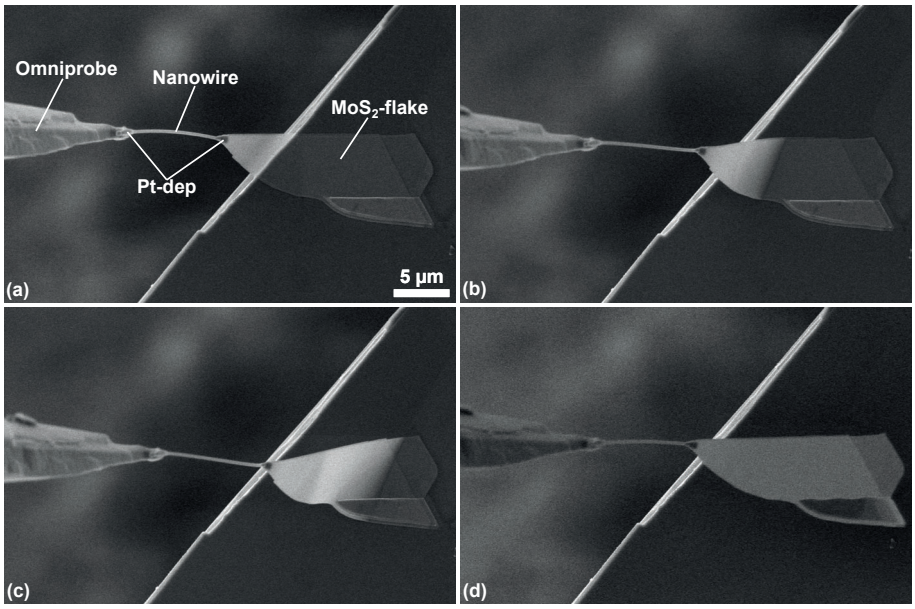

Figure 7.15: Secondary electron SEM images illustrating in situ lift-out of a multilayer 2D MoS_2-flake using an Omniprobe with a nanowire attached at the tip. **(a)** The free end of the nanowire is attached to the suspended corner of the flake by EBID-Pt. **(b)** By moving the Omniprobe upwards and to the right, the flake starts to detach from the substrate. **(c)** A well-defined wavefront moves from left-to-right as the flake is detached further. There is a clear difference in contrast between the detached part of the flake and the part that remains adhered to the substrate. **(d)** The flake is fully detached. No part of the flake remains on the substrate.

beam. Continuous scanning could make the flakes curl up and eventually fold onto themselves. This issue could be mitigated by increasing the acceleration voltage to 15-30 keV and reducing the beam current, unfortunately at the cost of reduced image contrast and signal-to-noise ratio.

The Omniprobe micromanipulator in a FIBSEM can also be used to lift out 2D-flakes. To increase the success rate for preparing freestanding flakes using the FIB-SEM Omniprobe, a slightly different approach was implemented, see Figure 7.15. Firstly, by extending the probe by attaching a GaAs nanowire at the tip of the probe, the risk of damaging the flake decreases since the elastic nanowire acts as a buffer between the flake and the rigid probe (Figure 7.15 a). With this trick, it is possible to use the less precise Omniprobe inside the FIBSEM to pick up flakes. Furthermore, starting with a flake that already has one freestanding corner facilitates the lift-off process in two ways; it makes the height of the probe not so critical, and it creates a natural starting point for the detachment of the flake from the substrate (Figure 7.15 b), greatly reducing the risk of breaking the flake. The free end of the nanowire was attached to the freestanding corner of the flake by EBID-Pt. As the probe is lifted upwards and moved slightly to the right, a wavefront moves from left to right through the flake (Figure 7.15 b and c), defining the border between the detached part of the flake and the part still adhered to the substrate. The contrast difference between these two regions arises due to an increased SE signal in the detached part,

partly because the surface is tilted there, and partly because the flake is thin so the SE can escape both from the lower surface and the upper surface of the detached part. In the end, the flake is completely detached from the substrate and may be transferred to another site (Figure 7.15 d). This procedure is more straight-forward and has a higher success rate than in situ lift-off or exfoliation of flakes that are completely attached to a substrate. However, it relies on the preparation of flakes that already has a small freestanding part. This is more difficult to prepare than flakes lying flat on a substrate, but can be done using PDMS-stamping.

After the flake has been lifted off the substrate it could be transferred to another substrate or support. An example of this is shown in Figure 7.16, where a flake was lifted off by the Omniprobe + nanowire (Figure 7.16 a) and was transferred to a TEM Cu-grid (Figure 7.16 b). The flake was attached to the grid by EBID-Pt and the Omniprobe was detached using the FIB to cut through the nanowire. The nanowire creates a distance between the Omniprobe and the flake, making it possible to cut the probe loose without exposing the flake to the ion beam. The Cu-grid can

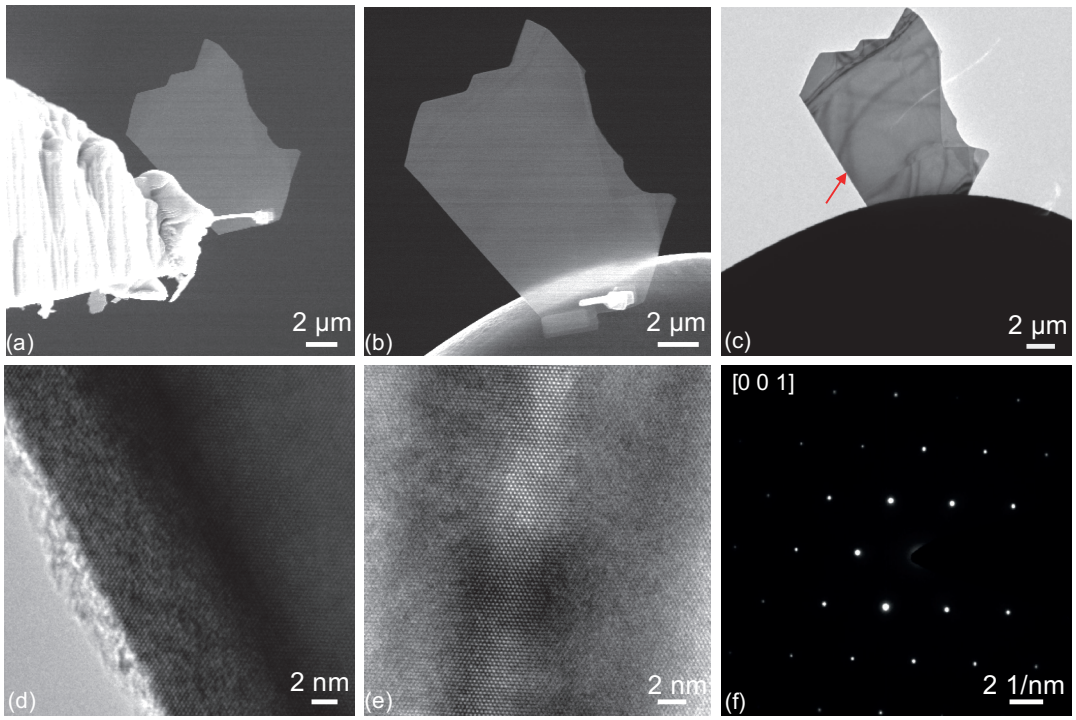

Figure 7.16: Transfer to TEM-grid and TEM characterization of multilayer 2D MoS_2-flakes. **(a)** Secondary electron SEM image showing a flake that has been lifted off the substrate using Omniprobe + nanowire and EBID-Pt. **(b)** Secondary electron SEM image of the flake after it has been transferred and attached to a Cu-grid by EBID-Pt. The Omniprobe was detached by cutting the nanowire using FIB-milling. **(c)** Low magnification BF TEM micrograph of the transferred flake. **(d)** High-resolution TEM micrograph of the edge marked by the red arrow in (c). **(e)** High-resolution TEM micrograph of another MoS_2-flake prepared by FIBSEM lift-out. **(f)** Example of diffraction pattern from an MoS_2-flake prepared by FIBSEM lift-out.

then be transferred to a TEM for characterization of the flake, see Figure 7.16 (c). In Figure 7.16 (d) a high resolution TEM micrograph of the area indicated by the red arrow in Figure 7.16 (c) is shown. At the very edge of the flake, there is a thin stripe with random contrast distribution. This could be due to that the flake has folded onto itself and is therefore no longer at the zone axis [180]. This is followed by a region with both periodic contrast representing the atomic crystalline structure of MoS_2 and an overlaid random contrast distribution. This could be due to a thinner part of the flake that has folded over a thicker part that is on the zone axis. Further inside the flake there is a dark region that indicates a thickness variation, and this is followed by a thicker, pure crystalline region. In Figure 7.16 (e), a high resolution TEM micrograph of another MoS_2-flake prepared by FIBSEM lift-out is shown. The lattice crystal structure is clearly visible. The contrast variation is most likely due to bending of the flake, making the crystal slightly misaligned to the beam in some areas. The single crystallinity of the flakes were confirmed by electron diffraction, an example of this is shown in Figure 7.16 (f).

7.2.2 Effects of elastic strain

Several different approaches were used to apply and study the effect of elastic strain in 2D MoS_2. In the first example, the in situ exfoliation technique shown in Figure 7.14 was used to get a freestanding flake attached to the STM-probe. By connecting the free end of the flake to a rigid W-tip, strain was applied to the flake and I-V measurements were performed, see Figure 7.17. Here, a rather small (approx. 3x4 μm^2) MoS_2-flake is suspended between and connected to the STM-probe and the W-

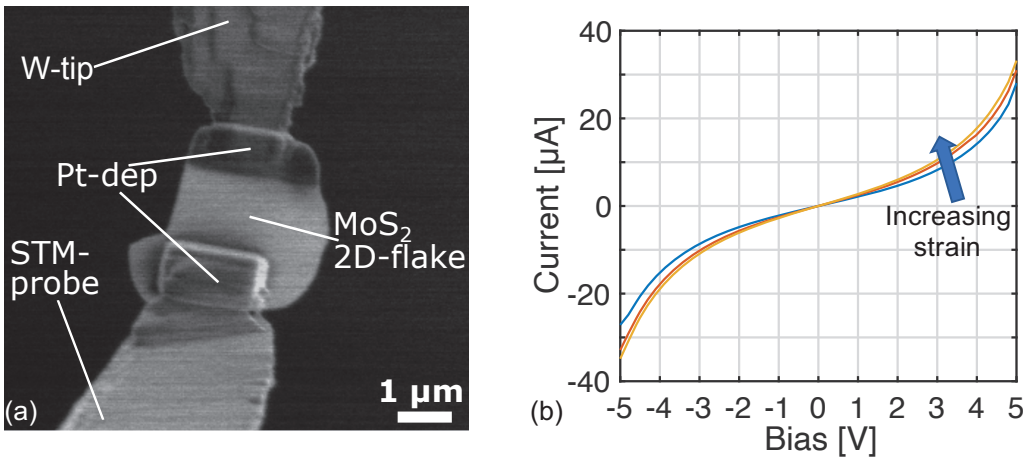

Figure 7.17: Straining and I-V characterization of a multilayer MoS_2-flake. **(a)** Secondary electron SEM image of an MoS_2-flake suspended between a Au STM-probe and a W-tip. The flake is attached and electrically connected to the STM-probe and W-tip by EBID-Pt inside a FIBSEM. By retracting the STM-probe, tensile strain was applied to the flake. **(b)** I-V characteristics at different strain levels.

tip by EBID-Pt. The W-tip was electrically connected to the measurement circuit by conductive epoxy. Strain was applied to the flake by retracting the STM-probe, and I-V characteristics were measured at different strain levels (Figure 7.17b). The I-V characteristics are non-linear and symmetrical, indicating that there are two equal Schottky barriers at the contacts. As the strain increases, the current at a given applied bias increases, which indicates that the resistivity of the flake decreases with strain. However, since the I-V characteristics are largely influenced by the contacts, it cannot be ruled out that the influence of strain on the I-V characteristics is a contact effect.

Another example where the in situ STM-setup was used to study the effect of elastic strain on the electrical properties of 2D MoS_2 is shown in Figure 7.18. Here, the STM-probe was attached by EBID-Pt to the free end of the flake that was transferred to a Cu-grid (Figure 7.18 a). By retracting the STM-probe, tensile strain was applied to the flake. The STM-probe was retracted in steps of approximately 40 nm, until the flake fractured (Figure 7.18 b). The estimated maximum tensile strain is around 1.4%. However, the strain is likely not homogeneous due to the irregular shape of

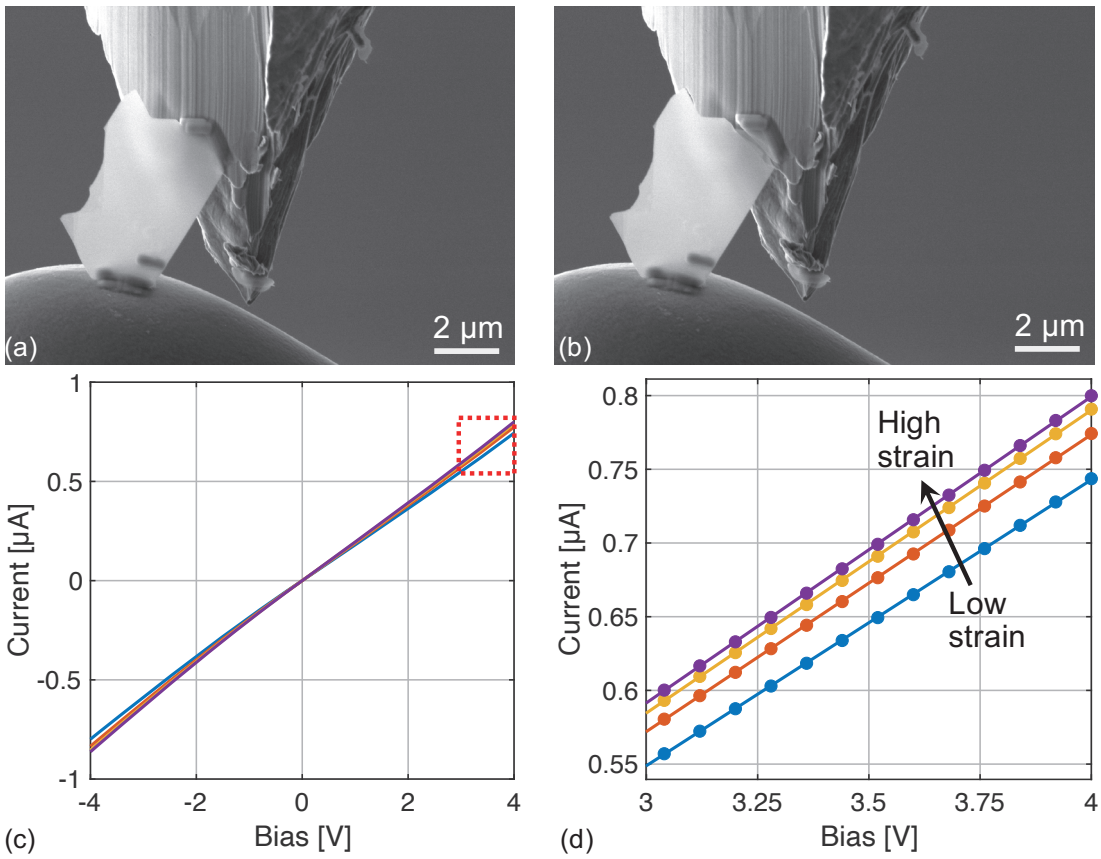

Figure 7.18: Straining and I-V characterization of multilayer MoS_2-flake. **(a)** Secondary electron SEM image showing the flake in the relaxed state, suspended between a Cu-grid and the STM-probe **(b)** SEM image of the flake after fracture. **(c)** I-V characteristics of the flake at different strain levels. **(d)** Highlight of the I-V curves in the area marked by the red square in (c).

the flake and Pt-contact. The I-V characteristics at the different strain levels are shown in Figure 7.18 (c). They are linear, indicating Ohmic contact. As the strain increases, the resistance of the flake decreases.

The piezo-straining device described in section 6.6 was used to perform in situ straining and Raman spectroscopy of individual MoS_2-flakes. An example is shown in Figure 7.19. Optical images of the relaxed state and the maximum strained state of a flake are shown in Figure 7.19 (a) and (b), respectively. The red circle indicates the position of the Raman laser beam. In Figure 7.19 (c), the Raman spectra of the relaxed and strained state is shown. The inset shows the E^1_{2g} peak with Gaussian fit. The straining results in a 4.5 cm^{-1} shift of the E^1_{2g} peak. This corresponds to a tensile strain of approximately 2.6 % [173].

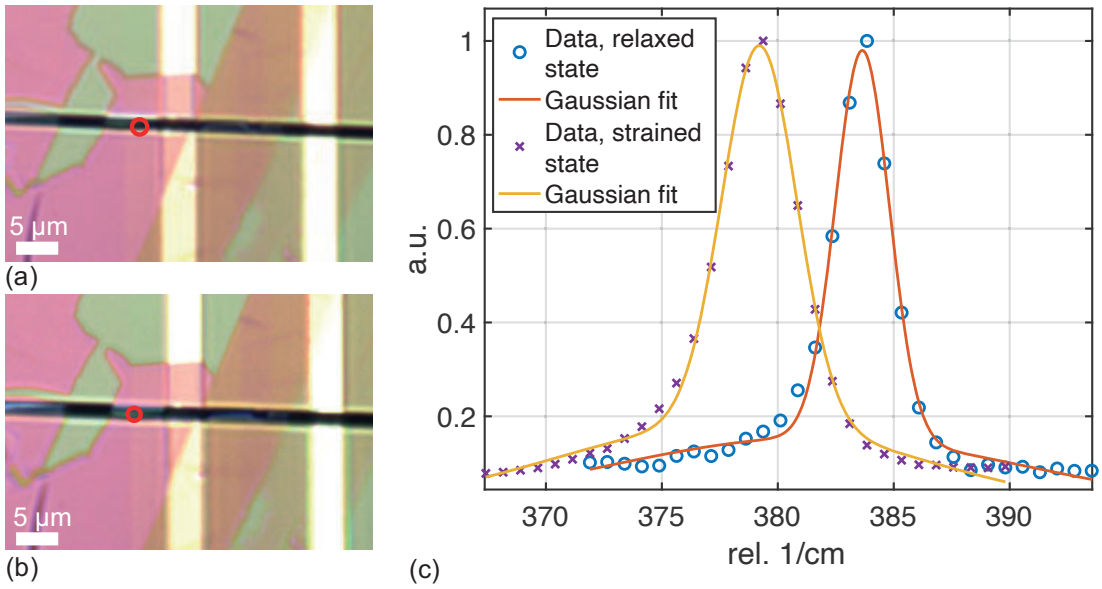

Figure 7.19: **(a)** Optical micrograph of an MoS_2-flake suspended over the gap of the piezo-device in the relaxed state. No bias is applied to the piezo-actuator. **(b)** Optical micrograph of the strained state of the MoS_2-flake. The gap is widened by applying a bias to the piezo-actuator. The red circle indicates the position of the Raman laser beam. **(c)** Normalized Raman spectra and Gaussian fits to the E^1_{2g} peak of the MoS_2-flake in the relaxed and strained state.

Another example of in situ straining using the piezo-device is shown in Figure 7.20. An MoS_2-flake was transferred onto the device using PDMS-stamping. Directly after the transfer, the flake was flat, see inset of Figure 7.20 (a). However, after mounting the device in the Raman microscope, the flake was bent in the suspended part, see Figure 7.20 (a) and the left column in Figure 7.20 (c). There is also a ripple across the gap. This is most likely due to mechanical instabilities of the device as mentioned before. As the gap is extended, the flake starts to straighten, see Figure 7.20 (b) and the right column in Figure 7.20 (c). Raman mapping was performed in the area marked by the green and red rectangles in 7.20 (a) and (b). Figure 7.20

(d) shows a map of the E^1_{2g} peak shift. We can see that, in the suspended part and in the ripple area, there is a significant red-shift of the peak compared to the flat regions away from the gap. As the gap is extended (right column in Figure 7.20 d), the red-shift decreases in the suspended part of the flake. Converting the red-shift to strain by assuming that a shift of 1.7 cm^{-1} corresponds to 1 % strain [173], we get the strain-maps shown in Figure 7.20 (e). Here we see that the bending in the suspended part and the ripple give rise to strain in the flake. As the gap is extended and the flake is straightened, the strain decreases within the gap, except at the lower edge of the flake, where the strain increases. Unfortunately, the flake was destroyed due to a failed I-V measurement before the gap could be extended any further.

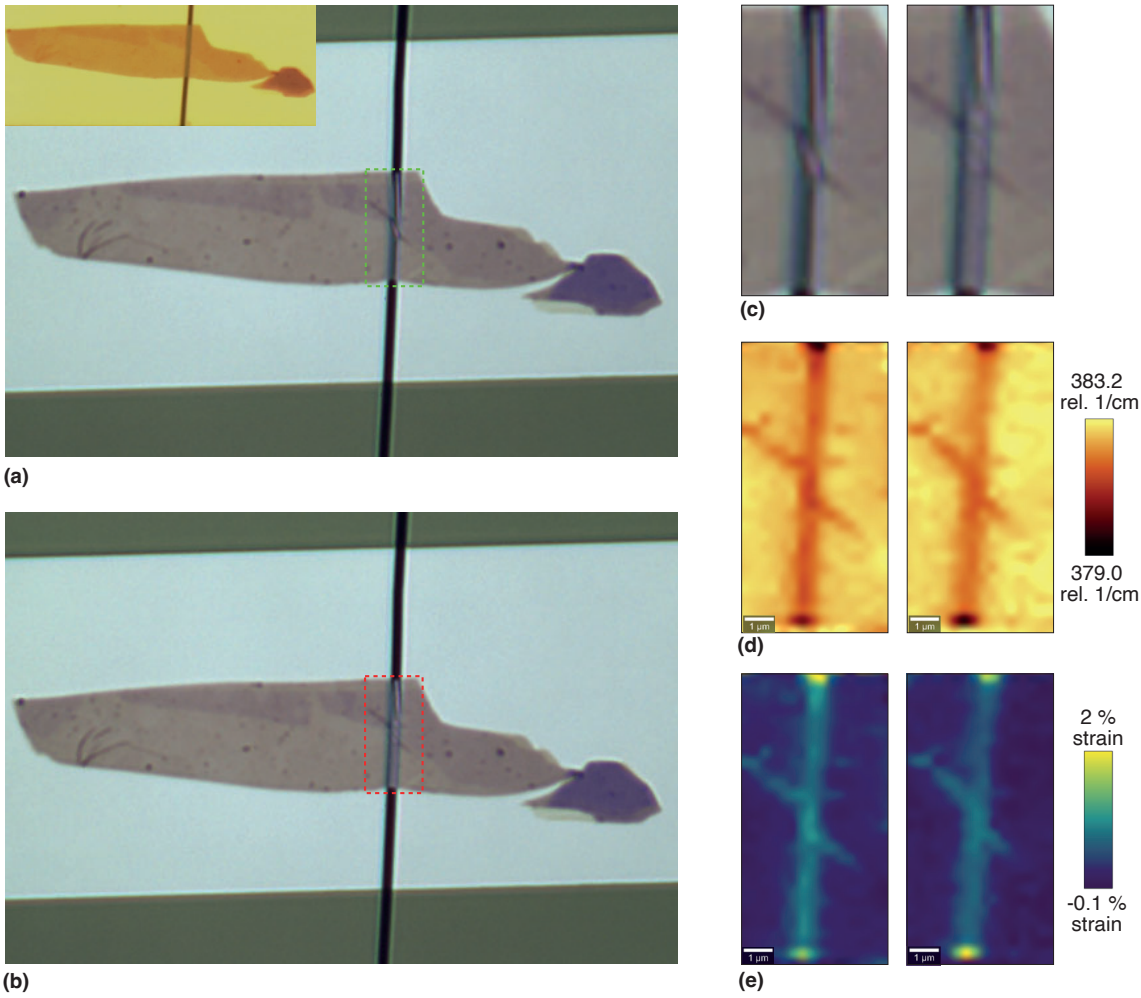

Figure 7.20: Optical images of suspended MoS_2-flake without **(a)** and with **(b)** bias applied to the piezo-actuator. **(c)** Zoom-in of the area marked with green rectangle (left column) and red rectangle (right column). **(d)** Raman maps of the E^1_{2g} peak shift. **(e)** Strain maps.

8. Conclusions and outlook

In this work, an in situ STM-FIBSEM technique for elastic strain engineering and charcterization of electrical and photovoltaic properties of nanomaterials was developed. Individual GaAs nanowires were investigated using the technique. It was found that the electrical contact between the STM-probe and the nanowires had a strong impact on the I-V characteristics. Two different procedures, FIB-milling and Joule heating, were successfully used to improve the quality of the contact. Removal of the nanowire native oxide layer and a decrease in the shunt resistance of the contact was found to be the main reasons for the contact improvement. With the electrical contact being optimized, the photovoltaic properties of the nanowires were investigated.

Elastic strain was shown to have a significant impact on the I-V characteristics of the nanowires. Analysis of the I-V curves showed that the resistance of both p-doped and radially p-i-n doped nanowires increased with uniaxial tensile strain at low to moderate strain levels and decreased with strain at high strain levels. Furthermore, the nanowire band gap decreased with increasing uniaxial tensile strain, with a maximum shift of 0.2 eV at 3% strain. This resulted in a red-shift in the nanowire absorption range, and the photocurrent during NIR LED illumination of the radially p-i-n doped nanowires was significantly enhanced by the applied strain.

These results show that it is possible to use elastic strain engineering to tune the properties of semiconductor nanowires. More specifically, ESE may be employed to improve the performance of nanowire solar cells. This is enabled by the high elasticity of the nanowires due to their nanoscale dimensions, and is not possible in conventional solar cells. As a next step, it would be interesting to find a way to introduce a strain gradient in the nanowires, creating a continuous decrease in the band gap going from top to bottom. In this way, the incoming sunlight could be used more efficiently, just as in a multijunction solar cell, but without the need to form material heterostructures. This could potentially increase the efficiency of nanowire solar cells.

Atomically thin 2D MoS_2-flakes were also investigated using the in situ STM-FIBSEM setup. The technique could be used for exfoliation, lift-out and transfer of 2D MoS_2-flakes and to apply strain to freestanding 2D-flakes while performing I-V measurements. The success rate of this technique is still rather low and does not come with any obvious advantages compared to existing techniques for ESE of 2D-materials. However, the in situ STM-FIBSEM technique could potentially be used for transfer of 2D-flakes in situations where conventional transfer methods may be difficult to use, for example onto supports that are not flat.

A piezo-based straining device was developed for ESE of 2D-materials. This device is highly versatile and precise thanks to the piezoelectric effect. Since the device is compatible with both electron and Raman microscopy, it could enable correlative EBIC mapping, Raman mapping and I-V measurements of strained 2D-materials. Once the mechanical stability of the device is further improved, large uniaxial strain can be applied to various 2D semiconductors, to study the effect of elastic strain on their electrical and optoelectronic properties. The in situ electron microscopy and Raman microscopy could enable further understanding of a range of intriguing strain-induced phenomena in 2D TMDCs, such as phase transitions and flexophotovoltaic effects.

Strain engineering is an effective method with huge potential to accelerate technological development, and it has already been implemented in commercially important materials systems and device applications. By tuning the electronic band structure and chemical bonding through modification of atomic structure, elastic strain engineering can be applied in many functional materials to tailor their physical, chemical and biological properties. The techniques developed in this thesis could be especially beneficial for studying strain engineering of nanoscale materials and devices, which are of critical importance in a range of scientific disciplines.

Bibliography

1. Atalla, M. M., Tannenbaum, E. & Scheibner, E. J. Stabilization of silicon surfaces by thermally grown oxides. *The Bell System Technical Journal* **38,** 749–783 (1959).
2. Bardeen, J. & Brattain, W. The transistor, a semi-conductor triode. *Phys. Rev.* **74,** 231–231 (1948).
3. Joachim Möller, H. Semiconductors for solar cell applications. *Progress in Materials Science* **35,** 205–418 (1991).
4. Rosencher, E. & Vinter, B. *Optoelectronics* (ed Piva, P. G.) (Cambridge University Press, 2002).
5. Geim, A. K. & Novoselov, K. S. The rise of graphene PROGRESS. *Nature Materials* **6,** 183–191 (2007).
6. Xia, B. Y. *et al.* One-Dimensional Nanostructures : Synthesis , Characterization, and Applications. *Advanced Materials* **15,** 353–389 (2003).
7. Greer, J. R. & Nix, W. D. Nanoscale gold pillars strengthened through dislocation starvation. *Physical Review B - Condensed Matter and Materials Physics* **73,** 1–6 (2006).
8. Zhu, T. & Li, J. Ultra-strength materials. *Progress in Materials Science* **55,** 710–757 (2010).
9. Goldberger, J., Hochbaum, A. I., Fan, R. & Yang, P. Silicon vertically integrated nanowire field effect transistors. *Nano Letters* **6,** 973–977 (2006).
10. Law, M. *et al.* Nanoribbon waveguides for subwavelength photonics integration. *Science* **305,** 1269–1273 (2004).
11. Huang, M. H. *et al.* Room-temperature ultraviolet nanowire nanolasers. *Science* **292,** 1897–1899 (2001).
12. Hahn, C. *et al.* Epitaxial growth of InGaN nanowire arrays for light emitting diodes. *ACS Nano* **5,** 3970–3976 (2011).
13. Krogstrup, P. *et al.* Single-nanowire solar cells beyond the Shockley–Queisser limit. *Nature Photonics* **7,** 1–5 (2013).
14. Biermanns, A. *et al.* Strain accommodation in Ga-assisted GaAs nanowires grown on silicon (111). *Nanotechnology* **23** (2012).
15. Otnes, G. & Borgström, M. T. Towards high efficiency nanowire solar cells. *Nano Today,* 1–15 (2016).

16. Wang, Q. H., Kalantar-Zadeh, K., Kis, A., Coleman, J. N. & Strano, M. S. Electronics and optoelectronics of two-dimensional transition metal dichalcogenides. *Nature Nanotechnology* **7,** 699–712 (2012).

17. Song, S., Rahaman, M. & Jariwala, D. Can 2D Semiconductors Be Game-Changers for Nanoelectronics and Photonics? *ACS Nano* **18,** 10955–10978 (2024).

18. Wang, L. *et al.* 2D Photovoltaic Devices: Progress and Prospects. *Small Methods* **2,** 1–20 (2018).

19. Zhang, H. *et al.* Approaching the ideal elastic strain limit in silicon nanowires. *Science Advances* **2,** 2–10 (2016).

20. Signorello, G., Karg, S., Björk, M. T., Gotsmann, B. & Riel, H. Tuning the light emission from GaAs nanowires over 290 meV with uniaxial strain. *Nano Letters* **13,** 917–924 (2013).

21. Cooper, R. C. *et al.* Nonlinear elastic behavior of two-dimensional molybdenum disulfide. *Phys. Rev. B* **87,** 035423 (3 Jan. 2013).

22. Li, J., Shan, Z. & Ma, E. Elastic strain engineering for unprecedented materials properties. *MRS Bulletin* **39,** 108–114 (2014).

23. Vurgaftman, I., Meyer, J. R. & Ram-Mohan, L. R. Band parameters for III-V compound semiconductors and their alloys. *Journal of Applied Physics* **89,** 5815–5875 (2001).

24. Wagner, R. S. & Ellis, W. C. Vapor-liquid-solid mechanism of single crystal growth. *Applied Physics Letters* **4,** 89–90 (1964).

25. Hamano, T., Hirayama, H. & Aoyagi, Y. New technique for fabrication of two-dimensional photonic bandgap crystals by selective epitaxy. *Japanese Journal of Applied Physics, Part 2: Letters* **36** (1997).

26. Dhindsa, N. *et al.* Highly ordered vertical GaAs nanowire arrays with dry etching and their optical properties. *Nanotechnology* **25,** 305303(11pp) (2014).

27. Dhindsa, N. & Saini, S. S. Top-down fabricated tapered GaAs nanowires with sacrificial etching of the mask. *Nanotechnology* **28** (2017).

28. Barrigón, E., Heurlin, M., Bi, Z., Monemar, B. & Samuelson, L. Synthesis and Applications of III-V Nanowires. *Chemical Reviews* **119,** 9170–9220 (2019).

29. Harmand, J. C. *et al.* Atomic Step Flow on a Nanofacet. *Physical Review Letters* **121,** 166101 (2018).

30. Perea, D. E. *et al.* Three-dimensional nanoscale composition mapping of semiconductor nanowires. *Nano Letters* **6,** 181–185 (2006).

31. Allen, J. E. *et al.* High-resolution detection of Au catalyst atoms in Si nanowires. *Nature Nanotechnology* **3,** 168–173 (2008).

32. Boulanger, J. P. *et al.* Characterization of a Ga-Assisted GaAs Nanowire Array Solar Cell on Si Substrate. *IEEE Journal of Photovoltaics* **6,** 661–667 (2016).

33. Ikejiri, K., Noborisaka, J., Hara, S., Motohisa, J. & Fukui, T. Mechanism of catalyst-free growth of GaAs nanowires by selective area MOVPE. *Journal of Crystal Growth* **298,** 616–619 (2007).

34. Franchi, S. *Molecular beam epitaxy: fundamentals, historical background and future prospects* 1–46 (Elsevier, 2013).

35. Krogstrup, P. *et al.* Structural phase control in self-catalyzed growth of GaAs nanowires on silicon (111). *Nano Letters* **10,** 4475–4482 (2010).

36. Uccelli, E. *et al.* Three-dimensional multiple-order twinning of self-catalyzed GaAs nanowires on Si substrates. *Nano Letters* **11,** 3827–3832 (2011).

37. Plissard, S., Larrieu, G., Wallart, X. & Caroff, P. High yield of self-catalyzed GaAs nanowire arrays grown on silicon via gallium droplet positioning. *Nanotechnology* **22** (2011).

38. Vukajlovic-Plestina, J. *et al.* Fundamental aspects to localize self-catalyzed III-V nanowires on silicon. *Nature Communications* **10** (2019).

39. Colombo, C., Heiß, M., Grätzel, M. & Fontcuberta I Morral, A. Gallium arsenide p-i-n radial structures for photovoltaic applications. *Applied Physics Letters* **94** (2009).

40. Li, Z., Tan, H. H., Jagadish, C. & Fu, L. III–V Semiconductor Single Nanowire Solar Cells: A Review. *Advanced Materials Technologies* **3,** 1–12 (2018).

41. Torkhov, N. A. Formation of a Native-Oxide Structure on the Surface of n-GaAs under Natural Oxidation in Air. *Semiconductors* **37,** 1177–1184 (2003).

42. Rhoderick, E. H. & Williams, R. H. *Metal–Semiconductor Contacts (2nd Edition)* (Springer Science + Business Media, 1988).

43. Ito, T. Simple criterion for wurtzite-zinc-blende polytypism in semiconductors. *Japanese Journal of Applied Physics, Part 2: Letters* **37,** 9–13 (1998).

44. Caroff, P., Bolinsson, J. & Johansson, J. Crystal phases in III-V nanowires: From random toward engineered polytypism. *IEEE Journal on Selected Topics in Quantum Electronics* **17,** 829–846 (2011).

45. Jacobsson, D. *et al.* Interface dynamics and crystal phase switching in GaAs nanowires. *Nature* **531,** 317–322 (2016).

46. Akopian, N., Patriarche, G., Liu, L., Harmand, J. C. & Zwiller, V. Crystal phase quantum dots. *Nano Letters* **10,** 1198–1201 (2010).

47. Qian, X., Kawai, M., Goto, H. & Li, J. Effect of twin boundaries and structural polytypes on electron transport in GaAs. *Computational Materials Science* **108,** 258–263 (2015).

48. Shimamura, K., Yuan, Z., Shimojo, F. & Nakano, A. Effects of twins on the electronic properties of GaAs. *Applied Physics Letters* **103,** 1–5 (2013).

49. Dimitrijev, S. *Principles of Semiconductor Devices (2nd Edition)* (Oxford University Press, 2012).

50. Würfel, P. & Würfel, U. *Physics of Solar Cells: From Basic Principles to Advanced Concepts, Second, Updated and Expanded Edition* (Wiley-VCH, 2009).

51. Keppens, A., Ryckaert, W. R., Deconinck, G. & Hanselaer, P. High power light-emitting diode junction temperature determination from current-voltage characteristics. *Journal of Applied Physics* **104** (2008).

52. Sangster Alan, J. *Electromagnetic Foundations of Solar Radiation Collection: A Technology for Sustainability* (Springer, 2014).

53. Miller, O. D., Yablonovitch, E. & Kurtz, S. R. Strong Internal and External Luminescence as Solar Cells Approach the Shockley–Queisser Limit. *IEEE Journal of Photovoltaics* **2,** 303–311 (2012).

54. Shockley, W. & Read, W. T. Statistics of the recombinations of holes and electrons. *Physical Review* **87,** 835–842 (1952).

55. Shah, J. M., Li, Y. L., Gessmann, T. & Schubert, E. F. Experimental analysis and theoretical model for anomalously high ideality factors (n>2.0) in AlGaN/GaN p-n junction diodes. *Journal of Applied Physics* **94,** 2627–2630 (2003).

56. U.S. Department of Energy (DOE)/NREL/ALLIANCE. *Reference Air Mass 1.5 Spectra* `https://www.nrel.gov/grid/solar-resource/spectra-am1.5.html` (05/01/2022).

57. Rühle, S. Tabulated values of the Shockley-Queisser limit for single junction solar cells. *Solar Energy* **130,** 139–147 (2016).

58. Shockley, W. & Queisser, H. J. Detailed balance limit of efficiency of p-n junction solar cells. *Journal of Applied Physics* **32,** 510–519 (1961).

59. France, R. M. *et al.* Triple-junction solar cells with 39.5% terrestrial and 34.2% space efficiency enabled by thick quantum well superlattices. *Joule* **6,** 1121–1135 (2022).

60. Dimroth, F. *et al.* Four-Junction Wafer-Bonded Concentrator Solar Cells. *IEEE Journal of Photovoltaics* **6,** 343–349 (2016).

61. Green, M. A. *et al.* Solar cell efficiency tables (Version 63). *Progress in Photovoltaics: Research and Applications* **32,** 3–13 (2024).

62. Li, J. *et al.* A Brief Review of High Efficiency III-V Solar Cells for Space Application. *Frontiers in Physics* **8,** 1–15 (2021).

63. National Renewable Energy Laboratory (NREL). *Best Research-Cell Efficiency Chart* `https://www.nrel.gov/pv/cell-efficiency.html` (10/17/2024).

64. Cui, Y. *et al.* Efficiency enhancement of InP nanowire solar cells by surface cleaning. *Nano Letters* **13,** 4113–4117 (2013).

65. Gao, Q. *et al.* Axial p-n junction design and characterization for InP nanowire array solar cells. *Progress in Photovoltaics: Research and Applications* **27,** 237–244 (2019).

66. Aberg, I. *et al.* A GaAs nanowire array solar cell with 15.3% efficiency at 1 sun. *IEEE Journal of Photovoltaics* **6,** 185–190 (2016).

67. Mariani, G., Zhou, Z., Scofield, A. & Huffaker, D. L. Direct-bandgap epitaxial core-multishell nanopillar photovoltaics featuring subwavelength optical concentrators. *Nano Letters* **13,** 1632–1637 (2013).

68. Mariani, G. *et al.* Patterned radial GaAs nanopillar solar cells. *Nano Letters* **11,** 2490–2494 (2011).

69. Hu, Y., Lapierre, R. R., Li, M., Chen, K. & He, J. J. Optical characteristics of GaAs nanowire solar cells. *Journal of Applied Physics* **112** (2012).

70. Lin, C. & Povinelli, M. L. The effect of plasmonic particles on solar absorption in vertically aligned silicon nanowire arrays. *Applied Physics Letters* **97** (2010).

71. Yao, M. *et al.* GaAs nanowire array solar cells with axial p-i-n junctions. *Nano Letters* **14,** 3293–3303 (2014).

72. Hrachowina, L. *et al.* Development and Characterization of a bottom-up InP Nanowire Solar Cell with 16.7% Efficiency. *Conference Record of the IEEE Photovoltaic Specialists Conference* **2020-June,** 1754–1756 (2020).

73. Anttu, N. & Xu, H. Q. Efficient light management in vertical nanowire arrays for photovoltaics. *Optics express* **21 Suppl 3,** A558–75 (2013).

74. Anttu, N. Absorption of light in a single vertical nanowire and a nanowire array. *Nanotechnology* **30** (2019).

75. Wen, L. *et al.* Theoretical analysis and modeling of light trapping in high efficicency GaAs nanowire array solar cells. *Applied Physics Letters* **99** (2011).

76. Muskens, O. L., Rivas, J. G., Algra, R. E., Bakkers, E. P. & Lagendijk, A. Design of light scattering in nanowire materials for photovoltaic applications. *Nano Letters* **8,** 2638–2642 (2008).

77. Diedenhofen, S. L. *et al.* Broad-band and omnidirectional antireflection coatings based on semiconductor nanorods. *Advanced Materials* **21,** 973–978 (2009).

78. Fan, Z. *et al.* Ordered arrays of dual-diameter nanopillars for maximized optical absorption. *Nano Letters* **10,** 3823–3827 (2010).

79. Diedenhofen, S. L., Janssen, O. T., Grzela, G., Bakkers, E. P. & Gómez Rivas, J. Strong geometrical dependence of the absorption of light in arrays of semiconductor nanowires. *ACS Nano* **5,** 2316–2323 (2011).

80. Anttu, N. Shockley-queisser detailed balance efficiency limit for nanowire solar cells. *ACS Photonics* **2,** 446–453 (2015).

81. Korzun, K., Castellanos, G. W., de Boer, D. K., Gómez Rivas, J. & Haverkort, J. E. Nanowire Solar Cell Above the Radiative Limit. *Advanced Optical Materials* **9,** 1–7 (2021).

82. Matthews, J. & Blakeslee, A. Defects in epitaxial multilayers: I. Misfit dislocations. *Journal of Crystal Growth* **27,** 118–125 (1974).

83. Kalogirou, S. A. *McEvoy's Handbook of Photovoltaics - Fundamentals and Applications (3rd Edition)* (Elsevier, 2018).

84. Cirlin, G. E. *et al.* Critical diameters and temperature domains for MBE growth of III-V nanowires on lattice mismatched substrates. *Physica Status Solidi - Rapid Research Letters* **3,** 112–114 (2009).

85. Borgström, M. T. *et al.* Nanowires with promise for photovoltaics. *IEEE Journal on Selected Topics in Quantum Electronics* **17,** 1050–1061 (2011).

86. Holm, J. V. *et al.* Surface-passivated GaAsP single-nanowire solar cells exceeding 10% efficiency grown on silicon. *Nature Communications* **4,** 1–5 (2013).

87. Yao, M. *et al.* Tandem Solar Cells Using GaAs Nanowires on Si: Design, Fabrication, and Observation of Voltage Addition. *Nano Letters* **15,** 7217–7224.

88. Mariani, G., Scofield, A. C., Hung, C.-H. & Huffaker, D. L. GaAs nanopillar-array solar cells employing in situ surface passivation. *Nature communications* **4,** 1497 (2013).

89. Cui, Y. *et al.* Efficiency enhancement of InP nanowire solar cells by surface cleaning. *Nano letters* **13,** 4113–7 (Sept. 2013).

90. Zhong, Z. *et al.* Efficiency enhancement of axial junction InP single nanowire solar cells by dielectric coating. *Nano Energy* **28,** 106–114 (2016).

91. Zhang, Y. & Liu, H. Self-catalyzed GaAs(P) nanowires and their application for solar cells. *Journal of Physics D: Applied Physics* **53** (2020).

92. Green, M. A. *et al.* Solar cell efficiency tables (Version 58). *Progress in Photovoltaics: Research and Applications* **29,** 657–667 (2021).

93. Hüttenhofer, L. *et al.* Optimization of Ohmic Contacts to n-Type GaAs Nanowires. *Physical Review Applied* **10,** 034024 (2018).

94. Rizzo Piton, M. *et al.* Optimization of Ohmic Contacts to p-GaAs Nanowires. *Nanoscale Research Letters* **14** (2019).

95. Colombo, C., Heiß, M., Grätzel, M. & Fontcuberta I Morral, A. Gallium arsenide p-i-n radial structures for photovoltaic applications. *Applied Physics Letters* **94** (2009).

96. Tian, B. *et al.* Coaxial silicon nanowires as solar cells and nanoelectronic power sources. *Nature* **449,** 885–889 (2007).

97. Gutsche, C. *et al.* Direct determination of minority carrier diffusion lengths at axial GaAs nanowire p-n junctions. *Nano Letters* **12,** 1453–1458 (2012).

98. Heiss, M. & Fontcuberta I Morral, A. Fundamental limits in the external quantum efficiency of single nanowire solar cells. *Applied Physics Letters* **99,** 97–100 (2011).

99. Nowzari, A. *et al.* A comparative study of absorption in vertically and laterally oriented InP core-shell nanowire photovoltaic devices. *Nano Letters* **15,** 1809–1814 (2015).

100. Ko, W. S. *et al.* Illumination Angle Insensitive Single Indium Phosphide Tapered Nanopillar Solar Cell. *Nano Letters* **15,** 4961–4967 (2015).

101. Piazza, V. *et al.* Nanoscale investigation of a radial p-n junction in self-catalyzed GaAs nanowires grown on Si (111). *Nanoscale* **10,** 20207–20217 (2018).

102. Otnes, G. *et al.* Understanding InP Nanowire Array Solar Cell Performance by Nanoprobe-Enabled Single Nanowire Measurements. *Nano Letters* **18,** 3038–3046 (2018).

103. Barrigón, E., Hrachowina, L. & Borgström, M. T. Light current-voltage measurements of single, as-grown, nanowire solar cells standing vertically on a substrate. *Nano Energy* **78** (2020).

104. Novoselov, K. S., Geim, A. K., Morozov, S. V. & Jiang, D. Electric Field Effect in Atomically Thin Carbon Films. *Science* **306,** 666–669 (2004).

105. Manzeli, S., Ovchinnikov, D., Pasquier, D., Yazyev, O. V. & Kis, A. 2D transition metal dichalcogenides. *Nature Reviews Materials* **2** (2017).

106. Novoselov, K. S. *et al.* Two-dimensional atomic crystals. *Proceedings of the National Academy of Sciences of the United States of America* **102,** 10451–10453 (2005).

107. Huang, Y. *et al.* Reliable Exfoliation of Large-Area High-Quality Flakes of Graphene and Other Two-Dimensional Materials. *ACS Nano* **9,** 10612–10620 (2015).

108. Magda, G. Z. *et al.* Exfoliation of large-area transition metal chalcogenide single layers. *Scientific Reports* **5,** 3–7 (2015).

109. Heyl, M. & List-Kratochvil, E. J. Only gold can pull this off: mechanical exfoliations of transition metal dichalcogenides beyond scotch tape. *Applied Physics A: Materials Science and Processing* **129,** 1–17 (2023).

110. Castellanos-Gomez, A. *et al.* Deterministic transfer of two-dimensional materials by all-dry viscoelastic stamping. *2D Materials* **1,** 011002 (2014).

111. Nourbakhsh, A., Zubair, A., Dresselhaus, M. S. & Palacios, T. Transport properties of a MoS2/WSe2 heterojunction transistor and its potential for application. *Nano Letters* **16,** 1359–1366 (2016).

112. Gupta, D., Chauhan, V. & Kumar, R. A comprehensive review on synthesis and applications of molybdenum disulfide (MoS2) material: Past and recent developments. *Inorganic Chemistry Communications* **121,** 108200 (2020).

113. Liu, N. *et al.* Large-Area Atomically Thin MoS2 Nanosheets Prepared Using Electrochemical Exfoliation. *ACS Nano* **8.** PMID: 24937086, 6902–6910 (2014).

114. Samy, O., Zeng, S., Birowosuto, M. D. & El Moutaouakil, A. A review on MoS2 properties, synthesis, sensing applications and challenges. *Crystals* **11,** 1–24 (2021).

115. Jang, Y., Yeo, S., Lee, H. B. R., Kim, H. & Kim, S. H. Wafer-scale, conformal and direct growth of MoS 2 thin films by atomic layer deposition. *Applied Surface Science* **365,** 160–165 (2016).

116. Xu, J., Zhang, J., Zhang, W. & Lee, C.-S. Interlayer Nanoarchitectonics of Two-Dimensional Transition-Metal Dichalcogenides Nanosheets for Energy Storage and Conversion Applications. *Advanced Energy Materials* **7,** 1700571 (2017).

117. Ding, Y. *et al.* First principles study of structural, vibrational and electronic properties of graphene-like MX2 (M=Mo, Nb, W, Ta; X=S, Se, Te) monolayers. *Physica B: Condensed Matter* **406,** 2254–2260 (2011).

118. Yoon, Y., Ganapathi, K. & Salahuddin, S. How Good Can Monolayer MoS2 Transistors Be? *Nano Letters* **11,** 3768–3773 (2011).

119. Shanmugam, M., Bansal, T., Durcan, C. A. & Yu, B. Molybdenum disulphide/titanium dioxide nanocomposite-poly 3-hexylthiophene bulk heterojunction solar cell. *Applied Physics Letters* **100,** 153901 (Apr. 2012).

120. Wang, G. *et al.* Colloquium: Excitons in atomically thin transition metal dichalcogenides. *Reviews of Modern Physics* **90,** 21001 (2018).

121. Akinwande, D. *et al.* Graphene and two-dimensional materials for silicon technology. *Nature* **573,** 507–518 (2019).

122. Splendiani, A. *et al.* Emerging photoluminescence in monolayer MoS2. *Nano Letters* **10,** 1271–1275 (2010).

123. Mak, K. F., Lee, C., Hone, J., Shan, J. & Heinz, T. F. Atomically thin MoS2: A new direct-gap semiconductor. *Physical Review Letters* **105,** 2–5 (2010).

124. Li, M.-Y., Chen, C.-H., Shi, Y. & Li, L.-J. Heterostructures based on two-dimensional layered materials and their potential applications. *Materials Today* **19,** 322–335 (2016).

125. He, F. *et al.* Moiré Patterns in 2D Materials: A Review. *ACS Nano* **15,** 5944–5958 (2021).

126. Thompson, S. E., Sun, G., Choi, Y. S. & Nishida, T. Uniaxial-process-induced Strained-Si: Extending the CMOS roadmap. *IEEE Transactions on Electron Devices* **53,** 1010–1020 (2006).

127. Kittel, C. *Introduction to Solid State Physics (8th Edition)* (John Wiley & Sons, Inc., 2005).

128. Sun, Y., Thompson, S. E. & Nishida, T. *Strain Effect in Semiconductors* (Oxford University Press, 2012).

129. Gabrys, P. A. *et al.* Lattice Mismatch in Crystalline Nanoparticle Thin Films. *Nano Letters* **18,** 579–585 (2018).

130. Armstrong, R. W. 60 years of hall-petch: Past to present nano-scale connections. *Materials Transactions* **55,** 2–12 (2014).

131. Yuan, R., Beyerlein, I. J. & Zhou, C. Coupled crystal orientation-size effects on the strength of nano crystals. *Scientific Reports* **6,** 1–9 (2016).

132. Uchic, M. D., Dimiduk, D. M., Florando, J. N. & Nix, W. D. Sample dimensions influence strength and crystal plasticity. *Science* **305,** 986–989 (2004).

133. Balaghi, L. *et al.* Widely tunable GaAs bandgap via strain engineering in core/shell nanowires with large lattice mismatch. *Nature Communications* **10,** 1–10 (2019).

134. Signorello, G. *et al.* Manipulating Surface States of III-V Nanowires with Uniaxial Stress. *Nano Letters* **17,** 2816–2824 (2017).

135. Agrawal, R., Peng, B., Gdoutos, E. E. & Espinosa, H. D. Elasticity size effects in ZnO nanowires-A combined experimental- computational approach. *Nano Letters* **8,** 3668–3674 (2008).

136. Zeng, L. *et al.* Correlation between Electrical Transport and Nanoscale Strain in InAs/In 0.6 Ga 0.4 As Core-Shell Nanowires. *Nano Letters* **18,** 4949–4956 (2018).

137. Wang, Z. L. & Song, J. Piezoelectric Nanogenerators Based on Zinc Oxide Nanowire Arrays. *Science* **312,** 242–246 (2006).

138. Zeng, L. *et al.* The Effect of Bending Deformation on Charge Transport and Electron Effective Mass of p-doped GaAs Nanowires. *Physica Status Solidi - Rapid Research Letters* **13,** 1–8 (2019).

139. Pan, C. *et al.* Enhanced Cu 2S/CdS coaxial nanowire solar cells by piezo-phototronic effect. *Nano Letters* **12,** 3302–3307 (2012).

140. Zhu, L. *et al.* Enhancing the Efficiency of Silicon-Based Solar Cells by the Piezo-Phototronic Effect. *ACS Nano* **11,** 1894–1900 (2017).

141. Alekseev, P. A. *et al.* Effect of the uniaxial compression on the GaAs nanowire solar cell. *Micromachines* **11,** 1–13 (2020).

142. Sun, H., Agrawal, P. & Singh, C. V. A first-principles study of the relationship between modulus and ideal strength of single-layer, transition metal dichalcogenides. *Materials Advances* **2,** 6631–6640 (2021).

143. Falin, A. *et al.* Mechanical Properties of Atomically Thin Tungsten Dichalcogenides: WS2, WSe2, and WTe2. *ACS Nano* **15,** 2600–2610 (2021).

144. Scalise, E., Houssa, M., Pourtois, G., Afanas'ev, V. & Stesmans, A. Strain-induced semiconductor to metal transition in the two-dimensional honeycomb structure of MoS2. *Nano Research* **5,** 43–48 (2012).

145. Castellanos-Gomez, A. *et al.* Elastic properties of freely suspended MoS2 nanosheets. *Advanced Materials* **24,** 772–775 (2012).

146. Manzeli, S., Allain, A., Ghadimi, A. & Kis, A. Piezoresistivity and Strain-induced Band Gap Tuning in Atomically Thin MoS2. *Nano Letters* **15,** 5330–5335 (2015).

147. Song, S. *et al.* Room Temperature Semiconductor–Metal Transition of MoTe2 Thin Films Engineered by Strain. *Nano Letters* **16,** 188–193 (2016).

148. Wang, G. *et al.* Measuring interlayer shear stress in bilayer graphene. *Physical Review Letters* **119,** 1–7 (2017).

149. Castellanos-Gomez, A. *et al.* Local strain engineering in atomically thin MoS2. *Nano Letters* **13,** 5361–5366 (2013).

150. Han, Y. *et al.* Experimental nanomechanics of 2D materials for strain engineering. *Applied Nanoscience (Switzerland)* **11,** 1075–1091 (2021).

151. Han, Y. *et al.* Deep Elastic Strain Engineering of 2D Materials and Their Twisted Bilayers. *ACS Applied Materials and Interfaces* **14,** 8655–8663 (2022).

152. Roldán, R., Castellanos-Gomez, A., Cappelluti, E. & Guinea, F. Strain engineering in semiconducting two-dimensional crystals. *Journal of Physics Condensed Matter* **27** (2015).

153. Peng, Z., Chen, X., Fan, Y., Srolovitz, D. J. & Lei, D. Strain engineering of 2D semiconductors and graphene: from strain fields to band-structure tuning and photonic applications. *Light: Science and Applications* **9** (2020).

154. He, K., Poole, C., Mak, K. F. & Shan, J. Experimental demonstration of continuous electronic structure tuning via strain in atomically thin MoS2. *Nano Letters* **13,** 2931–2936 (2013).

155. Lloyd, D. *et al.* Band Gap Engineering with Ultralarge Biaxial Strains in Suspended Monolayer MoS2. *Nano Letters* **16,** 5836–5841 (2016).

156. Blundo, E. *et al.* Evidence of the direct-to-indirect band gap transition in strained two-dimensional WS2, MoS2, and WSe2. *Physical Review Research* **2,** 1–7 (2020).

157. Hasegawa, H. Fermi level pinning and schottky barrier height control at metal-semiconductor interfaces of InP and related materials. *Japanese Journal of Applied Physics, Part 1: Regular Papers and Short Notes and Review Papers* **38,** 1098–1102 (1999).

158. Sharma, B. L. *Metal-Semiconductor Schottky Barrier Junctions and Their Applications* (Plenum Press, New York, 1984).

159. Piotrowska, A. Ohmic Contacts to GaAs: Fundamentals and Practice. *Acta Physica Polonica A* **84,** 491–504 (1993).

160. Rideout, V. A review of the theory and technology for ohmic contacts to group III–V compound semiconductors. *Solid-State Electronics* **18,** 541–550 (1975).

161. Zhang, Z. *et al.* Quantitative analysis of current-voltage characteristics of semiconducting nanowires: Decoupling of contact effects. *Advanced Functional Materials* **17,** 2478–2489 (2007).

162. Padovani, F. A. & Stratton, R. Field and thermionic-field emission in Schottky barriers. *Solid State Electronics* **9,** 695–707 (1966).

163. Chattopadhyay, P. The effect of shunt resistance on the electrical characteristics of Schottky barrier diodes. *Journal of Physics D: Applied Physics* **29,** 823–829 (1996).

164. Zekry, Z. & Eldallal, G. Effect of MS contact on the electrical behaviour of solar cells. *Solid State Electronics* **31,** 91–97 (1988).

165. Goldstein, J. I. *et al. Scanning Electron Microscopy and X-Ray Microanalysis, Fourth Edition* (Springer Science + Business Media New York, 2018).

166. Reimer, L. *Scanning Electron Microscopy* (Springer-Verlag Berlin Heidelberg, 1998).

167. Kazumori, H., Honda, K., Matsuya, M., Date, M. & Nielsen, C. Field emission SEM with a spherical and chromatic aberration corrector. *Microscopy and Microanalysis* **10,** 1370–1371 (2004).

168. Leamy, H. J. Charge collection scanning electron microscopy. *Journal of Applied Physics* **53** (1982).

169. Williams, D. B. & Carter, C. B. *Transmission Electron Microscopy: A Textbook for Materials Science* (Springer Science + Business Media, 2009).

170. Gianuzzi, L. A. & Stevie, F. A. *Introduction to Focused Ion Beams* (Springer Science + Business Media, Inc., 2005).

171. Szymanski, H. A. *Raman Spectroscopy, Theory and Practice* (Plenum Press, New York, 1967).

172. Toporski, J., Dienig, T. & Hollricher, O. *Confocal Raman Microscopy (2nd Edition)* (Springer International Publishing AG, 2018).

173. Rice, C. *et al.* Raman-scattering measurements and first-principles calculations of strain-induced phonon shifts in monolayer MoS2. *Physical Review B - Condensed Matter and Materials Physics* **87,** 1–5 (2013).

174. Tan, C. K. *et al.* Raman studies of MoS2 under strain at different uniaxial directions. *Vacuum* **153,** 274–276 (2018).

175. Neri, I. & López-Suárez, M. Electronic transport modulation on suspended few-layer MoS2 under strain. *Physical Review B* **97,** 1–5 (2018).

176. Casadei, A. *et al.* Doping incorporation paths in catalyst-free Be-doped GaAs nanowires. *Applied Physics Letters* **102** (2013).

177. HQ Graphene. *MoS_2* `https://www.hqgraphene.com/MoS2.php` (10/16/2024).

178. Brown, S. J., Rose, P. D., Jones, G. A., Linfield, E. H. & Ritchie, D. A. Electrically active defect centers induced by Ga+ focused ion beam irradiation of GaAs(100). *Applied Physics Letters* **74,** 576–578 (1999).

179. Lavenus, P. *et al.* Experimental and theoretical analysis of transport properties of core-shell wire light emitting diodes probed by electron beam induced current microscopy. *Nanotechnology* **25** (2014).

180. Fabbri, F. *et al.* Novel near-infrared emission from crystal defects in MoS 2 multilayer flakes. *Nature Communications* **7,** 1–7 (2016).